EPITAXIAL ENGINEERING OF HIGH QUALITY TOPOLOGICAL INSULATOR FILMS

by

NIKESH KOIRALA

A dissertation submitted to the

Graduate School—New Brunswick

Rutgers, The State University of New Jersey

In partial fulfillment of the requirements

For the degree of

Doctor of Philosophy

Graduate Program in Physics and Astronomy

Written under the direction of

Seongshik Oh

And approved by

_____

_____

_____

_____

_____

New Brunswick, New Jersey

October, 2016

ABSTRACT OF THE DISSERTATION

EPITAXIAL ENGINEERING OF HIGH QUALITY TOPOLOGICAL INSULATOR FILMS

By NIKESH KOIRALA

Dissertation Director:

Seongshik Oh

Topological insulator is an exciting phase of matter because at its boundaries reside table-top version of Dirac fermions, while its bulk is supposed to be insulating. However, in real materials this latter condition is often far from being fulfilled and the bulk of the material is usually highly conducting due to the presence of inevitable defects. The aim of this dissertation is to understand the role of these defects on electrical properties of chalcogenide based topological insulators and utilize this knowledge to fabricate high quality films.

We start out by briefly introducing topological insulators. This is followed by Chapter 2, where we discuss experimental techniques that are pertinent to this work: thin film growth technique and electrical measurement. In Chapter 3, we will first seek theoretical understanding of role of defects in determining electrical properties of topological insulators and follow this by experimental results on Bi_2Se_3 films grown on epitaxially engineered virtual substrate, which show near ideal topological insulator behavior: namely, high mobility conduction through topological surface states and highly insulating bulk. We follow this in Chapter 4 with report of topological surface state originated quantum Hall effect in these films. A summary of results followed by future outlook will conclude the dissertation.

Acknowledgments

First and foremost, I want to thank my advisor Professor Seongshik Oh. Through patient mentorship, stimulating discussions and limitless friendship, he has taught me how to be an experimental physicist and enjoy my Ph.D. experience. His enthusiastic outlook towards research was infectious and motivated me even during tough times in the Ph.D. pursuit. I could not have done it without him.

I also would like to express my sincerest appreciation to my committee members, Professor Sevil Salur, Professor Kristjan Haule, Professor Weida Wu and Professor Daniel Dessau for their advice and guidance.

My labmates have been an integral part of my graduate life and I owe a tremendous amount to all of them. To Namrata Bansal for showing me how to use MBE during early days and being a friend. To my friends Maryam Salehi and Jisoo Moon with whom it has been a joy to work with during last couple of years. I am especially indebted to my friend Matthew Brahlek whose shared work-load and help has been vital in shaping up my research experience.

I would like to thank Prof. N. Peter Armitage and his student Liang Wu, Prof Danniel Dessau and his group, Prof. Weida Wu and his postdoc Jixia Dai, and Professor Hyunyong Choi and his students for fruitful discussions and collaborations.

I would also like to thank my friends and collegues Xueyun Wang, Matthew Bell, Joshua Paramanandam, Brian Dennis, Sebastian Reyes Lillo and Brett Manning for wonderful discussions and joyous times. I am fortunate to have my friends Ghanashyam, Sirjana, Prayas, Sunil, Hari, Dinesh and Kishor, who have made my stay at Rutgers more enjoyable.

Lastly, to my family to whom I am eternally grateful for everything. To my parents, Lila and Shanta, who have dedicated their lives to build a future for their children. To my sisters, Pushpa and Sanju, and brothers, Deepesh and Bharat, for their constant love and

support. To my grandparents for being ‘ba’ and ‘ama’. To my cousins Pramee, Pranaya, Prajjwal, Srijana and Pratistha for all the wonderful times. Love to my beautiful nieces Bivisha and Bibhuti.

Dedication

This work is entirely dedicated to my family without whose love and support this journey would not have been possible.

Table of Contents

List of Figures

Chapter 1

Introduction

Topological insulators are a new phase of matter that have energy gap in their bulk band-structure around the Fermi level and possess gap-less surface band that traverse the bulk band gap (Bernevig et al., 2006; Fu et al., 2007a). In this sense, topological insulators can be thought of as insulators that are *coated* with metallic boundary states. However, unlike, conventional insulators and semiconductors, which can also host accidental metallic surface bands(Goetzberger et al., 1976; Shockley, 1939; Tamm, 1932), in topological insulators the gap-less surface bands are a consequence of non-trivial topology of bulk band and are guaranteed to exist as long as the conditions for topological insulators are met(Hasan and Kane, 2010). These so called topological surface states disperse like Dirac electrons, have spin-momentum locking and are immune to backscattering. Due to their unique electronic band structure, topological insulators have been proposed to display novel physical phenomena including unusual quantum Hall effect (Koirala et al., 2015; Xu et al., 2014; Yoshimi et al., 2015), quantum anomalous Hall effect in magnetically doped topological insulators (Chang et al., 2013), quantized topological magneto-electric effect (Hasan and Kane, 2010) and host Majorana fermions (by inducing superconductivity) (Qi and Zhang, 2011). In addition they could also be very useful in technological applications that range from spintronics (Yokoyama and Murakami, 2014) to quantum computation (Stern and Lindner, 2013). As a result, they are an intensely studied condensed matter system.

In this chapter we will introduce the concept of topological insulators and follow it with a brief review of the initial developments in the field and then outline the scope of the work presented in the thesis.

1.1 A brief introduction to insulators that are 'topological'

Since the name topological insulator consists of two words: topology and insulators, we will begin by briefly introducing each and tie them together to lay the foundation for rest of the discussion.

1.1.1 Topology

The notion of topology developed as a tool to describe geometry of 3D manifolds. While topology encompasses a vast field within mathematics and a detailed treatment of it is beyond the scope of this thesis, here we will present an intuitive picture of topology with reference to classification of 3D objects. In geometry, if a 3D object can be adiabatically deformed into a different 3D object then both of these objects are said to have same topology. Otherwise they are topologically different. In this context, adiabatical deformation means slow and smooth changes such as stretching and bending, while actions such as tearing or gluing a hole are considered as drastic changes.

The central idea of topology relies on defining a single (or a set of) quantity called the topological index, which takes on discreet values. For objects with same topology, the topological index is the same, otherwise its different. The topological index associated with geometric objects is called a genus, which physically corresponds to the number of holes present in the object. Mathematically, the genus corresponds to the integral of Gaussian curvature over a closed 2D surface of a 3D objects as formalized by Gauss-Bonnet theorem. For example, a sphere and cube are topologically equivalent (no hole $\rightarrow$ genus =0), while a sphere and a torus (one hole $\rightarrow$ genus = 1) are topologically different. This is shown in Fig. 1.1. Due to the integered nature of the genus (for a closed surface), it is not possible to smoothly change the topology i.e. no adiabatical transformation can lead to a change in topology of a 3D object.

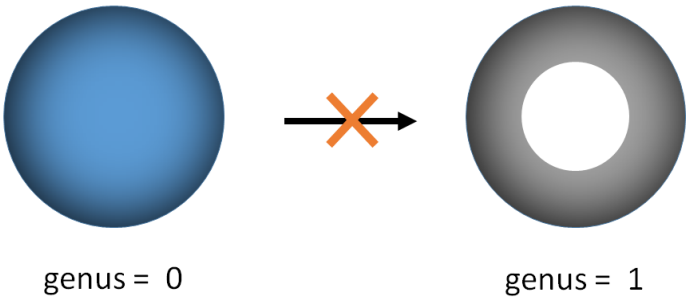

Figure 1.1: **Topology of 3D objects:** No adiabatical transformation can change a sphere (left) into a torus (right) since they have different topology. The topological index , i.e. genus, is 0 and 1 for the two shapes respectively.

1.1.2 Insulators

We will begin with a simple description of insulators[1]. Colloquially, metals and insulators are differentiated in terms of their ability to conduct *electricity*: metals are good conductors, while insulators are poor conductors. The underlying reason for such a physics can be understood in terms of the position of Fermi energy (E_F) in relation to the electronic energy bands. In a metal, E_F lies within a electronic band, while in insulators E_F lies between two energy bands that are separated by an energy gap. Therefore, in a insulator there is a completely filled band below E_F (known as valence band) and a completely empty band above it (known as conduction band) that are separated by the energy gap. This is shown in Fig 1.2.

This gap between the highest occupied electronic state (top of the valence band) and the lowest unoccupied electronic state (bottom of the conduction band), which can be on the order of ∼eV, is the reason why electrons in insulators cannot be *pushed* by an external electric field, which is usually too weak to excite an electron from the valence band to the conduction band resulting in no electrical conduction.On the other hand, due to the quasi-continuous nature of energy states within a band, electrons (or holes) in metals become conducting at arbitrarily small electric fields. Having discussed what insulators are, we next discuss where topology enters into description of insulators and whether all insulators

[1]Throughout this thesis, we will assume insulators to mean band insulators unless otherwise stated.

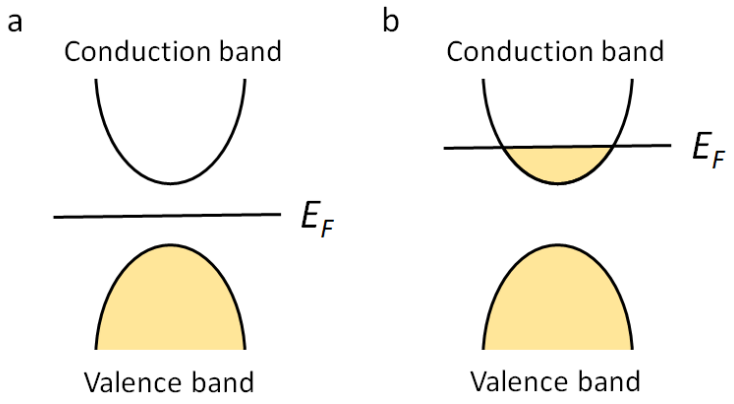

Figure 1.2: **Insulator versus metal:** The Fermi energy (E_F) lies (a) in the band gap for an insulator and (b) within the conduction band for a metal.

belong to the same topological classification.

1.1.3 Topology and insulators

We have seen that shapes, like spheres and toruses, belong to different topological classes that are indexed by different values of correponding topological index. In fact, the notion of topology for such 3D shapes has been generalized not only into higher dimensions but also to more abstract spaces such as the Hilbert space, which is where the quantum states of a system reside. Particularly, in the case of insulators the same ideas of topology of 3D shapes can be straight forwardly generalized to topologically classify the insulators. The notion of Gaussian curvature in geometric shapes is replaced by that of Berry curvature (Berry, 1984) for material systems, where Berry curvature for an energy band is derived from the properties of Bloch waves in that band . Analogous to the genus for geometric shapes, integral of Berry curvature over the Brillouin zone then gives the topological index for the band, which is called the Chern number (Chern, 1946; Thouless et al., 1982). Adding Chern numbers of all the filled bands in an insulator then gives the (total) Chern number of the insulator, which defines the topological class of an insulator. For conventional band insulators such as Al_2O_3, solid Ar or even the vacuum the Chern number turns out to be

zero and therefore these insulators are topologically trivial. But in the early 1980s, a new kind of insulator was discovered, which is now known as the quantum Hall insulator (QHI) (Klitzing et al., 1980; Laughlin, 1981) and this insulating state represents the first kind of topological insulator (Thouless et al., 1982). In the following we discuss the QHI briefly.

Consider a two dimensional electron gas (2DEG) where electrons are mobile in the 2D plane resulting in a metallic state. In the presence of a perpendicular magnetic field, these electrons get deflected due to Lorentz force leading to the cyclotron motion. With increasing magnetic field, these orbit get smaller and the electrons can be thought as becoming bound leading to the insulating phase. While the semiclassical picture presented above gives an intuitive picture of why the system becomes insulating, quantum mechanical treatment is required for the full understanding of this insulating state.

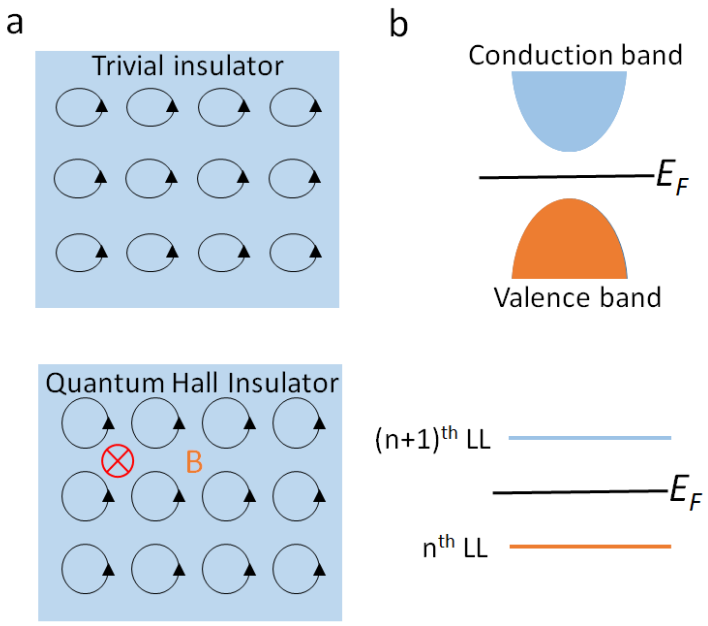

Figure 1.3: **Comparison between a trivial insulator and quantum Hall insulator:** (a) Schematic view of a trivial insulator (upper panel) and a QHI (bottom panel). (b) Corresponding band structure.Figure adapted from (Hasan and Kane, 2010)

In quantum mechanical treatment,when an external magnetic field is applied the continuous energy bands of 2DEG become discretized into discreet energy levels known as Landau Levels (LLs). For conventional 2DEGs, LLs are given by $E_n = \hbar\frac{eB}{m^*}(n+1/2)$, where e,m^*,B

and n are the electronic charge, effective mass of carriers, magnetic field and integer valued LL index respectively (2DEGs of Dirac electrons such as those present in graphene or TIs have a different LL structure, which we will discuss in Chapter 4.). When E_F lies within a LL, the system becomes metallic, while if E_F lies in between adjacent LLs (i.e. $(n)^{th}$ LL completely filled and $(n+1)^{th}$ LL completely empty), the bulk becomes insulating. We mention that some level of impurity or disorder needs to be in the system to observe this bulk insulating phase. Intuitively the reason for requirement of such impurities or disorder is as follows. In an ideally clean system all states within a LL are delocalized (conducting). Now if we imagine changing E_F w.r.t. LLs (for example by changing the magnetic field), then E_F will get pinned within a LL (and the bulk remains meatallic) until all states within that LLs are completely empty at which point E_F jumps to next LL (and the bulk again remains metallic). So a bulk insulating phase is not observed experimentally. On the other hand impurities localize states near the tails of LLs and when E_F lies in these states the system becomes insulating. A detailed formulation of how these localized states come about in the presence of impurities is beyond the scope of this thesis (See, for example, (Stone, 1992) for detail). As shown in Fig.1.3, a QHI looks similar to conventional insulator in a sense that electrons are localized as E_F lies between adjacent energy bands.

However, we can ask whether the QHI is in the same class as the topologically trivial band insulator? It turns out that the Chern number for a filled LL of a QHI is unity (See (Avron et al., 2003) and references therein). Hence a QHI state with n^{th} LL completely filled is a topological insulator indexed by Chern number = n. A natural question to ask is what happens at the boundary between two topologically different insulators? In order to intuitively see what happens at the boundary, we can imagine moving across the boundary between a trivial insulator (such as vacuum) and the QHI sample. Obviously, the topology changes as one moves from vacuum to the QHI sample. But an important aspect of topology is that it cannot be changed continuously. This is perhaps easy to understand in the context of geometric topology, where a sphere cannot be changed into a torus without rupturing it i.e. destroying the surface. Similarly, when moving from trivial insulator (vacuum) to topological insulator (QHI) the insulating state at the boundary must necessarily be destroyed (analogous to rupturing the surface of a sphere) in order for the topology to

change. This results in a metallic state at the boundary, whose existence is guaranteed by the topological arguments presented above. Experiments and theory have shown that there exist n metallic chiral edge states at the boundary, where n is the Chern number of the insulator (Klitzing et al., 1980; Kohmoto, 1985; Thouless et al., 1982). This fact has been explained in terms of bulk boundary correspondence theorem, which states that the number of metallic gapless boundary states corresponds to the difference between the topological index across the boundary(Hasan and Kane, 2010). The chiral nature of edge mode is in the sense that along a given edge, they only propagate along one direction, say left, and therefore cannot backscatter as there are no states available that move along the opposite direction. If the direction of the magnetic field were to be reversed, then accordingly the direction of the chiral edge modes would also be reversed. We briefly mention that this chiral nature of edge states leads to perfectly quantized Hall conductance $\sigma_{xy} = n\frac{e^2}{h}$, where n is the number of chiral edge modes (equivalently the Chern number of QHI). Furthermore, the longitudinal resistance $\rho_{xx} = 0$ and somewhat paradoxically longitudinal conductivity $\sigma_{xx} = 0$ in a QHI state (Klitzing et al., 1980). This latter part is actually consistent, since the usual assumption of $\vec{j}$ // $\vec{E}$ no longer holds due to off diagonal terms in conductivity tensor in the presence of magnetic field.

The QHI is an example of a topological insulator, but the fact that a magnetic field is applied in order to achieve the QHI means that the time reversal symmetry (TRS) is broken in QHI. In fact, a requirement for non-zero Chern number in an insulator is that the TRS be broken (Thouless et al., 1982). But, are there TRS preserving insulators that are topologically non-trivial? The answer turns out to be yes. The earliest work related to such pursuit was by Haldane, where he showed that a 2D honeycomb lattice with staggered magnetic field (such that the net magnetic field was zero) could be topologically non-trivial (Haldane, 1988). Although this system broke the TRS, no external magnetic field was required to achieve the non-trivial Chern insulator. Such a system has been experimentally realized in a honeycomb lattice of ultracold atoms (Jotzu et al., 2014). From middle of last decade pioneering theoretical work led by C.L. Kane (Fu and Kane, 2007; Fu et al., 2007b; Kane and Mele, 2005a,b), S.-C. Zhang (Bernevig et al., 2006; Bernevig and Zhang, 2006; Qi et al., 2008, 2006), J. Moore(Moore and Balents, 2007) and R. Roy (Roy, 2009)

showed that a TRS preserving topologically non-trivial insulator phase is indeed possible in both 2D and 3D. These insulators are now known as Z_2 topological insulators, or simply topological insulators (TIs) and we will discuss them next.

1.2 Topological insulators

1.2.1 Theoritical considerations

In TIs the TRS is preserved so the Chern number is zero and therefore the topological classification used for QHI is not applicable. However, a certain analogy exists between a QHI and (2D) TI and we will use it to paint an intuitive picture of TIs. In 2D TIs, due to TRS, Hall conductivity is zero, which means that there are no QHI like chiral edge modes. They instead have counter-propagating helical edge modes i.e. left moving modes have (say) spin up and right moving modes would then have spin down (See (Qi and Zhang, 2010) and references therein). From our discussion of QHI, it is clear that the 2D TI looks like two copies of spinful QHI as shown in Fig. 1.4. The counter propagating helical edge modes are time-reversed partner of each other so under timer reversal they get switched and the system remains invariant (as required by TRS). There can be no Hall conductivity due to counter-propagating edge modes,however, because down-spins flow in one direction and the up-spins flow in opposite direction, there is spin Hall conductivity. In fact, for this reason the 2D TI is also known as the quantum spin Hall insulator (although the spin Hall conductivity is not necessarily quantized) (Hasan and Kane, 2010). In order to distinguish the 2D TIs from trivial insulator, we can first look at the metallicity of edge states and use bulk boundary correspondence theorem to relate this to the underlying topology of the bulk bands. At the edge of a 2D insulator, edge states can arise in the bulk band gap. If the TRS is preserved, then Kramer's theorem states that each energy level is at least two fold degenerate (for a spin-1/2 system). This can be understood most easily in terms of anti-unitary nature of time reversal operator (T) as follows. By definition of anti-unitary operator,

$$T^2|\Psi>=-|\Psi>$$

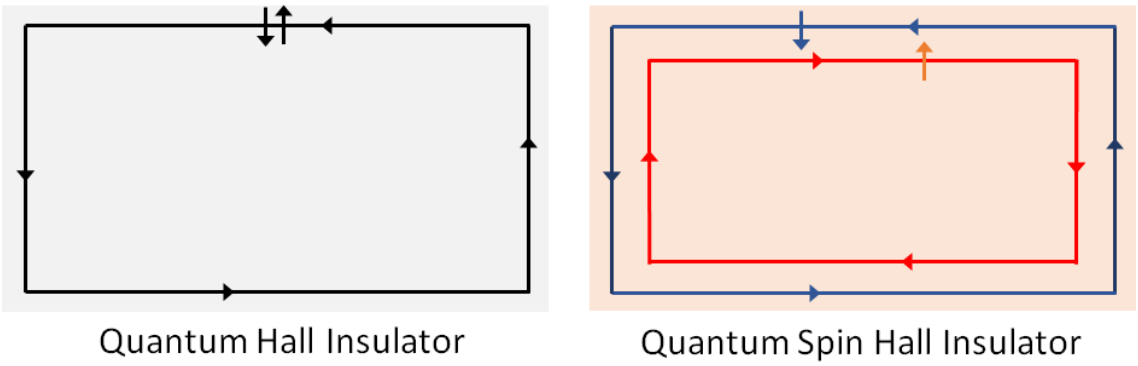

Figure 1.4: Comparison between a QHI (left panel) and QSHI(right panel):A QHI has chiral edge modes reflecting broken TRS, while a QSHI has counter-propagating helical edge modes and preserves TRS

which means $|\Psi>$ and $T|\Psi>$ are two distinct states. Since TRS symmetry means that T commutes with the Hamiltonian, both $|\Psi>$ and $T|\Psi>$ are eigenstates of the same energy eigenvalue, which proves the Kramer's theorem.

If SOC can be neglected, the edge bands are spin degenerate. In the presence of SOC, however, at a general momenta in k-space, the spin up and spin down states are split and the edge bands are non-degenerate (Note that the Kramer's theorem is still valid). However, at the time reversal invariant momenta (i.e. k =0 and $\frac{\pi}{a}$), the bands must cross.

As shown in Fig. 1.5 the two states at k = 0 and k =$\frac{\pi}{a}$ can be connected in two ways. Either they connect *pairwise* like in Fig. 1.5a, or they connect in a staggered fashion like in Fig. 1.5b. In the former case, E_F intersects the bands at even number of points, while for the latter case E_F intersects them at an odd number of points. Now we can imagine shifting the edge bands in energy. In the former case, this can lead to E_F lying in the gap and therefore the edge becomes insulating. This is a manifestation of adiabatical deformation of the Hamiltonian of the system into an trivially insulating state and therefore they belong to the same topological class. On the other hand for Fig. 1.5b, E_F is always guaranteed to cross at least one edge band as long as the TRS is preserved resulting in the edge mode always being metallic and hence the topology of the bulk being non-trivial.

We finally want to point out that all cases where E_F crosses edge bands even number of times can be adiabatically deformed to the situation of E_F crossing zero bands, while

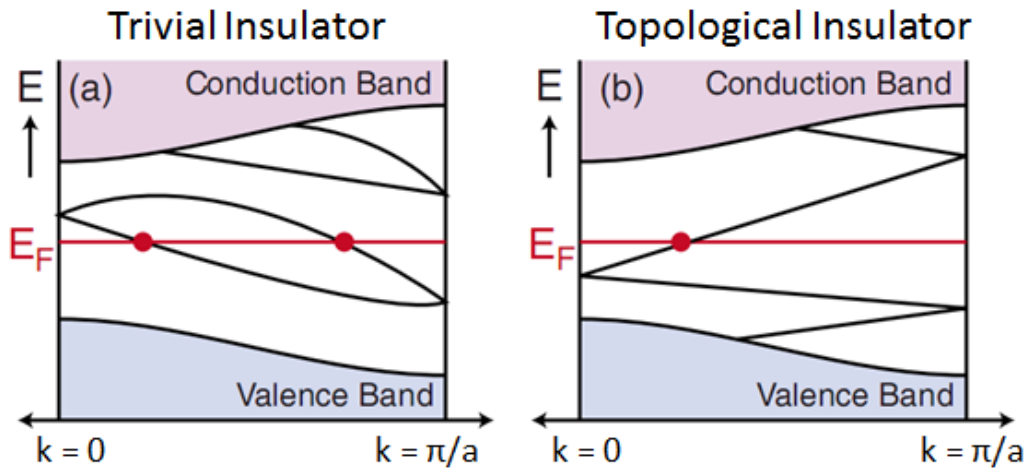

Figure 1.5: **Edge states in a trivial insulator vs. 2D TIs:** (a) Edge states can be adiabatically shifted resulting in zero Fermi crossing and thus become insulating (b) in 2D TIs there is at least one guaranteed (in general odd) crossing and edge states remain metallic. Figure adapted from (Hasan and Kane, 2010).

for the case of odd crossings there must be at least one crossing. Therefore, this system of topological classification of insulators only considers whether there is an even or odd number of Fermi level crossings and hence is a modulo 2 system: this is why these insulators are called Z_2 topological insulators as the topological invariant can only take values of either 0 or 1 (Hasan and Kane, 2010). This analysis can be generalized to 3D insulators, where instead of the edge states in 2D TIs, there are now surface states in 3D TIs. The physical reason behind the existence of such topologically protected surface (edge) states ultimately lies with strong spin-orbit coupling (SOC) in the bulk of the 3D (2D) TIs. In TIs, the SOC is strong enough to invert the bulk bands near the E_F, which results in the change of topological index from 0 to 1 (Zhang et al., 2009). At the boundary, the inverted bands of TIs meet the non-inverted bands of a trivial insulator. This change in band ordering can only be achieved if at the boundary the band gap closes, and this is the qualitative reason for existence of gapless metallic surface (edge) bands in TIs (Hasan and Kane, 2010). We will next discuss some of the properties of these gapless surface (edge) bands.

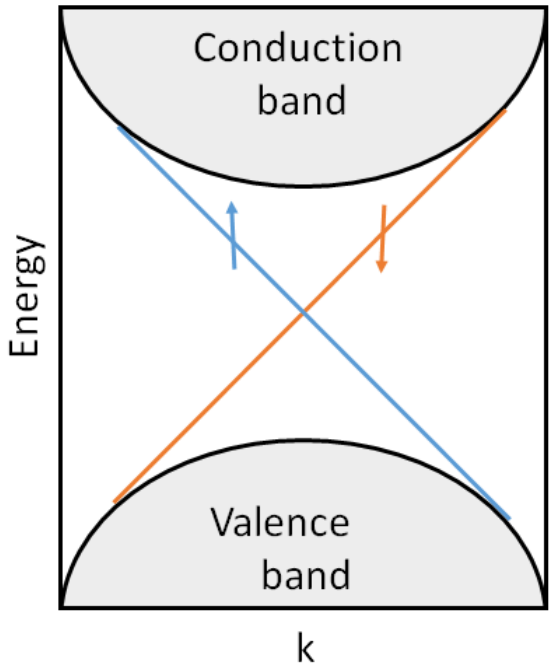

Figure 1.6: **Dispersion relation of topological surface states:** (a) Schematic of the band structure of a 3D TI showing bulk valence and conduction band. The bulk band gap is traversed by linearly dispersing, spin-momentum locked, helical edge modes as indicated by the color and direction of spins.

1.2.2 Topological surface states

The topologically (technically TRS) protected surface states on the boundary of 3D TIs are simply abbreviated as topological surface states (TSSs). As seen in Fig. 1.6, the dispersion of TSSs is $E \sim k$ rather than the usual $E \sim k^2$ dispersion of normal electrons. Such linear energy dispersion indicates Dirac-like nature of the TSSs carriers, and is reminiscent of the graphene bandstructure (Novoselov et al., 2005), which also has linear dispersion. However, there are some crucial differences. The TSSs bands are spin non-degenerate and there exist odd number of Dirac cones per TI surface, while in graphene there are two Dirac cones (even number) and the bands are spin-degenerate. In fact, due to the strong SOC, the spin of TSSs carriers are locked perpendicular to their momenta, a phenomena which has been termed as spin-momentum locking. The Dirac-like nature leads to unusual electronic behavior, which are most easily manifested at high external magnetic fields. For example, the LLs of TSSs show qualitatively different behavior than conventional 2DEGs with energy

of the n^{th} LL given by $E_n \propto \sqrt{nB}$, where B is the applied magnetic field. It is clear to see that this LL structure leads to existence of a n= 0 LL at zero energy (i.e. Dirac point) and unequal spacing between successive LLs (Cheng et al., 2010) both of which are absent for conventional 2DEGs. This novel Landau quantization also leads to associated 1/2-QHE (per surface) in TIs. The spin-momentum locking of surface states plays a crucial role in suppression of backscattering of TSSs carriers from (non-magnetic) disorder or impurities (Qi and Zhang, 2010). This can be understood in following way: backscattering means change of carrier momenta by 180^0, which due to spin-momentum locking leads to rotation of spin of the carriers by 180^0 as well, which is shown schematically in Fig. 1.7.

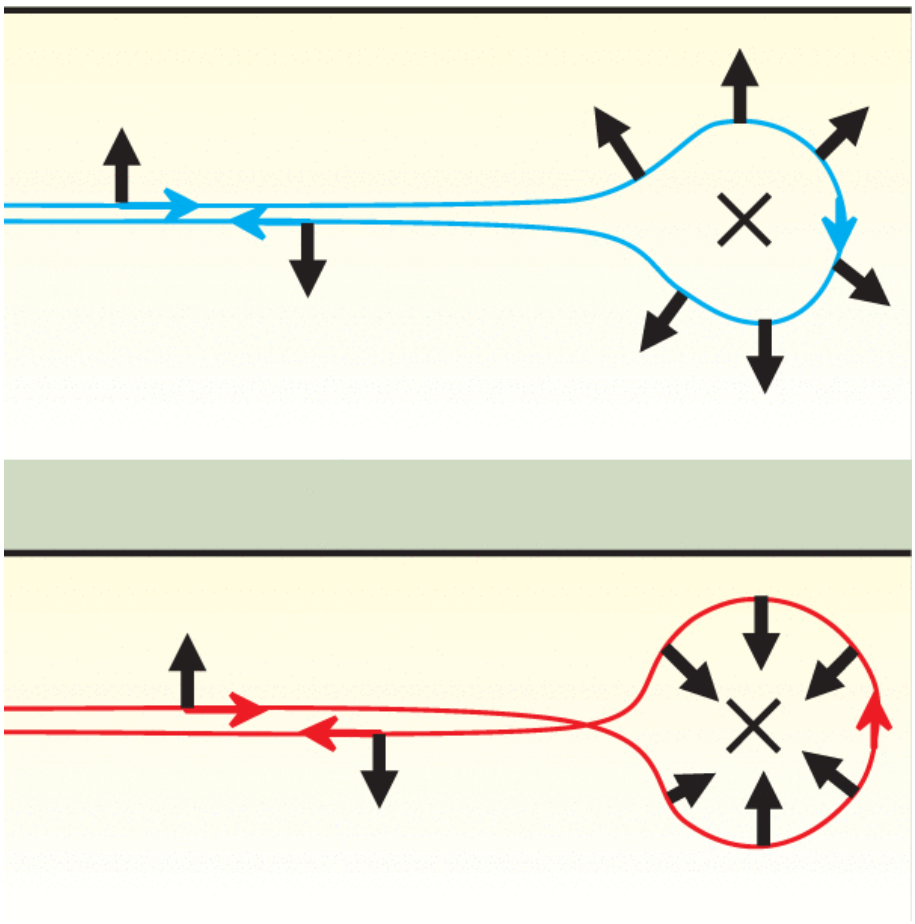

Figure 1.7: **Absence of backscattering of topological surface states:** clockwise (top panel) and anti-clockwise (bottom panel) rotation of momenta lead to π and -π rotation of spin. The fermionic nature of electrons then leads to an overall phase difference of -1 between the paths leading to zero amplitude for backscattering. Figure taken from (Qi and Zhang, 2010)

In quantum mechanical language, such backscattering involves summation of amplitude to backscatter in clockwise (-180^0) and counter-clockwise (+180^0) fashion. The interference between the clockwise and counter-clockwise rotations give total probability to backscatter to be zero. It is clear to see why the probability to backscatter must be zero from looking at the spin 1/2 nature of the fermions. The (counter) clockwise scattering path leads to $(+\pi)-\pi$ rotation of spin, which means the two paths differ by $(\pi + \pi = 2\pi)$ rotation of spin. But for spin 1/2 fermions, where a 4π rotation of spin is needed to come back to the same state, the 2π rotation of the spins leads to an overall negative sign of the wavefunction resulting in destructive interference between the two paths (Qi and Zhang, 2010). While the absence of backscattering does not guarantee dissipationless transport or even high mobility of TSSs, it does lead to suppression of electrical resistance compared to their classical values. If the TIs are subject to a small magnetic field, which destroys the destructive interference effect and therefore the loss of backscattering protection, a small increase in electrical resistance of TI samples is observed. This effect is known as weak-antilocalization effect (Bergman, 1982) and can be used to extract information about the number of independent conduction channels in a TI film (Hikami et al., 1980).

1.2.3 Experimental progress: 3D TI

The first TI material to be predicted (Bernevig et al., 2006) and subsequently experimentally observed were the CdTe-HgTe-CdTe quantum well heterostructures (König et al., 2007). For HgTe layer thickness > 6.3 nm, this system becomes a 2D TI, resulting in helical edge modes. This was followed by prediction and experimental observation of 3D TI state in Bi_xSb_{1-x} alloy (Fu and Kane, 2007; Hsieh et al., 2008). The 3D TI phase in the prototypical family of chalcogenide TIs namely: Bi_2Se_3, Bi_2Te_3 and Sb_2Te_3 was then simultaneously predicted (Zhang et al., 2009) and experimentally observed (Chen et al., 2009; Xia et al., 2009). We want to point out that surface sensitive tools such as angle resolved photo-electron spectroscopy (ARPES), which can directly probe band structure near the surface, and scanning tunneling spectroscopy (STS), which measures local density of states at the surface, played critical role in characterizing the 3D TI phase in these materials.

As shown in Fig. 1.8, ARPES showed that these chalcogenide based TIs had relatively

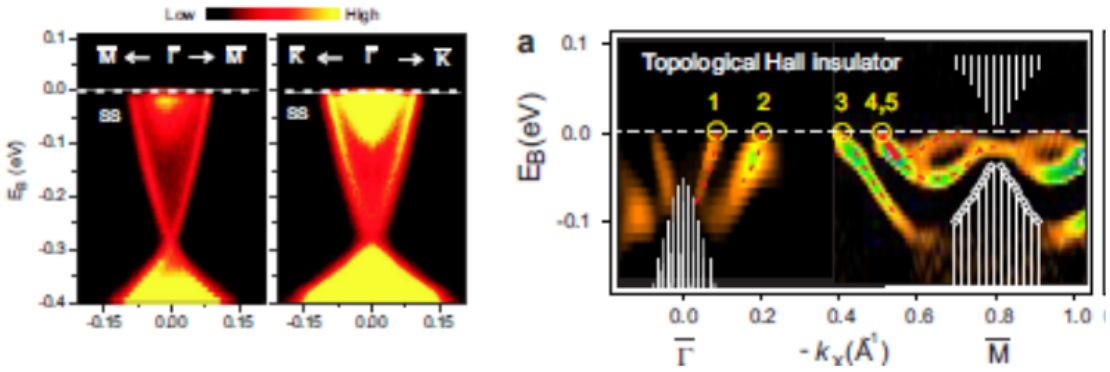

Figure 1.8: **Band structure of Bi_2Se_3 versus $Bi_{0.9}Sb_{0.1}$:** A large bulk band gap and a single topological surface state is observed in Bi_2Se_3 (left panel), while small bulk band gap and five surface states are observed in $Bi_{0.9}Sb_{0.1}$ (right panel) from ARPES.Figures taken from (Hsieh et al., 2008; Xia et al., 2009)

large bulk bandgap (exempified bye Bi_2Se_3) and a single Dirac cone per surface making these much more attractive compared to Bi_xSb_{1-x}, which has complicated surface state band structures with upto five surface states and relatively small bandgap. Furthermore, the alloy nature of Bi_xSb_{1-x} and the small range of x for which TI phase existed in Bi_xSb_{1-x} made the chalcogenide TIs the primary materials for further experimental and theoritical work of TI family. Bi_2Se_3 and Sb_2Te_3 had particularly advantageous over Bi_2Te_3, which has smaller band gap (∼160 meV) and a Dirac cone that is buried beneath the edge of bulk valence band. However, soon after it was realized that all these three compounds had defect densities high enough to make their bulk conducting. Apart from overwhelming the signatures of TSS conduction in electrical measurements due to bulk conduction, such high defect densities also prohibit observation of novel phenomena that are most easily observed near the Dirac point of TSSs. Given this scenario, a major effort in the TI field has been to make bulk of the samples insulating and move the Fermi level closer to the Dirac point. Over the last few years combination of various methods such as thin film growth, external doping and growth of ternary and quaternary solid solutions involving different combinations in the $(Bi_xSb_{1-x})_2(Se_yTe_{1-x})_3$ phase space have been actively pursued to minimize the net defect density with some striking success. This has, for example, led to experimental observation of TSS dominated transport, quantum Hall originating from TSSs and quantum anomalous

Hall effect in magnetic TIs (Analytis et al., 2010b; Brahlek et al., 2014; Chang et al., 2013; Koirala et al., 2015; Xu et al., 2014; Yoshimi et al., 2015). The central work of this thesis is also motivated by similar considerations.

1.3 Scope of present work

In the work presented in this thesis, we seek to understand the role of defects in the electrical properties of Bi_2Se_3 thin films. With this understanding, we then engineer a high quality substrate for Bi_2Se_3 to minimize defects in the film.Finally, we show the TSS dominant transport in these films. This thesis is structured as follows: In chapter 2, we discuss the experimental set up for growth and characterization of TI thin films. Chapters 3 and 4 contain results from our experiments and Chapter 5 contains conclusion and future outlook.

Chapter 2

Growth and measurement techniques

2.1 Growth of topological insulator thin films

Experiments in condensed matter physics often comprise of investigating properties of materials that belong to different phases of matter. Most routinely studied among these materials are the crystalline solids, since they host the most diverse phases of matter. For example, almost all metals, semiconductors, magnets and superconductors are crystalline solids. Frequently, in order to probe various structural and electronic properties of these materials, highest quality samples are required. Over the course of centuries and mostly during the last century different growth methods have been developed with increasing control over the size, purity and quality of the samples being grown.

Generally, in terms of their size, crystals can be divided into four categorizes: bulk crystals, thin films, nanorods and nanocrystals. Essentially going from bulk crystals to nanocrystals, the system size goes from macroscopic (on the order of mm) in all three dimensions to nanoscopic (on the order of nm) in all three dimensions. For example, a thin film would have two macroscopic dimensions and one nanoscopic dimension. The latter three structures with reduced dimensionality are collectively called nanostructures and they can often show physical properties that are different from those of bulk crystals. Furthermore, artificial composition of nanostructures such as thin film heterostructures and superlattices can show emergent phenomena that are unlike those of bulk materials (Chakhalian et al., 2014). Such properties make nanostructures interesting for fundamental research as well as technological advances. In this section we will primarily focus on the growth of TI thin films using molecular beam epitaxy (MBE) method, which is the relevant growth method for work presented in this thesis.

2.1.1 Fundamentals of thin film growth

A thin film growth essentially consists of three steps: 1) creating molecular, atomic or ionic species from a source material 2) transporting them to the deposition surface, which is usually called the substrate and 3) condensation of the species onto the substrate. These steps are shown schematically in Fig. 2.1.

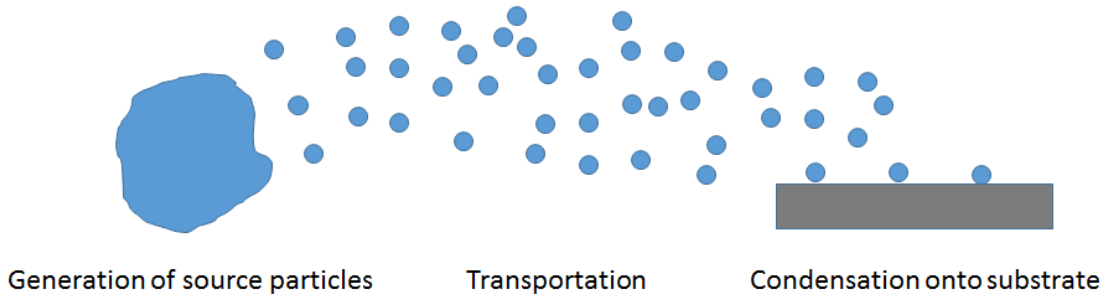

Figure 2.1: **Cartoon depicting three steps involved in thin film growth process:** Species of source material are generated, transported and then condense on the surface of the substrate.

While these are the basic steps involved in all thin film deposition methods, the details of how these processes occurs differ among different methods and depend upon several crucial factors including chemical and structural compatibility of substrate to the desired film, substrate temperature and morphology, background pressure of the growth chamber etc. These processes make different growth methods optimal for different types of thin film growth. Here we will first discuss these three steps involved in thin film growth.

Generation of source particles

The first step in any thin film deposition process is to generate particles of constituents of intended film. This process basically involves extracting particles from some reservoir of source material. This could involve various methods such as heating a piece of source material and evaporating it (this is the primary mode of generating particles in MBE), ejecting particles from a piece of source material by impinging it with energetic ions (this process is used in sputtering) or using electric current (this process is used in electroplating)

or simply opening a valve of cylinder containing gaseous compound containing the element (these are usually called precursor gases) needed for film growth (this process is used in chemical vapor deposition). The particles that are produced can be atomic, molecular or ionic in nature depending upon the process used.

Transportation of generated particles

Once the particles of source material are created they need to be transported to the substrate. In many thin film deposition processes this step occurs naturally. For example, in both MBE and sputtering, once the particles are generated they just 'fly' towards the substrate. However, how this 'flying' occurs is very different in MBE compared to sputtering. In MBE, due to extremely high vacuum in the growth chamber, the evaporating particles do not get scattered by residual gases in the chamber and the transportation is ballistic in nature i.e. they form a beam of particle. On the other hand, due to relatively high pressure in a sputtering chamber, particles suffer multiple scattering while flying out from the source material. This leads to a diffusive transport, which means rather than flowing in a beam they spread out in a fashion similar to a drop of ink mixing in water. In some processes such as electroplating, an electrolyte is neede to carry the ions from source to the substrate.

Condensation onto the substrate

The last step of thin film deposition is condensation of the particles onto the substrate. In many cases this involves some sort of chemical reaction taking place at the substrate. For example in MBE growth of Bi_2Se_3, Bi and Se atoms react at the substrate surface to form Bi_2Se_3 film. This is also the case in chemical vapor deposition, where the precursor gases carrying differet elements react at the substrate surface to form the desired compound, which then starts to grow. In general the condensation of incoming species is usually a complex process, and in the following, we discuss these briefly in the context of MBE growth.

Physisorption, chemisorption and nucleation

When an incoming species of a source impinges the substrate, depending upon their kinetic energy, either they bounce off the surface or they get adsorbed onto it. If the kinetic

energy is too high, then they immediately desorb from the substrate. On the other hand if the incoming species have low enough kinetic energy then they can thermalize, which is a process where they lose some of the kinetic energy to the substrate to be thermally acclimated to the substrate temperature. If the substrate temperature is too high then they will just desorb again. On the other hand if the substrate temperature is low enough, then they can adsorb to the substrate. The adsorption process in thin film growth usually occurs via following mechanism: the incoming species get weakly bound to the substrate by Van der Waals type force (physical adsorption), but they are still mobile enough so that these adatoms move around on the surface until they find a site with deep potential (such as step edges of the substrate), where they chemically react with each-other or with the substrate (chemical adsorption) and form a cluster. Due to the stronger chemical bonding during chemisorption, these adatoms become more stable. These clusters can grow with more incoming adatoms and are called nucleation centers. The film then begins to grow from these nucleation centers.

2.1.2 Growth mode

Depending upon numerous growth parameters, growing films can be of three types: single crystals, polycrystalline and amorphous. Single crystal films are defined by long range ordering of their crystal structure so that the entire sample is made up of a single domain, while polycrystalline films are defined by randomly ordered crystal grains that are usually on the order of ∼10 - 100 nm and an amorphous film is one where the grain size is on the same order as unit cells. In general, polycrystalline and amorphous films are formed when the substrate temperature is low and the deposition rate is high so that the adatoms do not have enough mobility on the substrate surface to rearrange themselves in a ordered way to form crystalline films. Furthermore, structural similarity of substrate to the intended film also plays a crucial role. For example, growth of Bi_2Se_3 on structurally matched In_2Se_3 leads to single crystal films (Koirala et al., 2015), while growth on an amorphous-SiO_2 substrate results in Bi_2Se_3 films that are composed of crystallites that are randomly oriented in the growth plane (Bansal et al., 2014). In most applications of MBE growth, the goal is to optimize various parameters so that single crystal films are obtained. The

process of growth of single crystal film that follows the crystalline ordering of substrate is known as epitaxy.

If the intended thin film and the substrate are the same, then the epitaxy is called homoepitaxy. This is the case, for example, when GaAs thin film is grown on top of GaAs substrate. On the other hand if the substrate is different than the growing film, then the epitaxy is called heteroepitaxy. This is the case for example when Bi_2Se_3 is grown on top of In_2Se_3. During the epitaxial growth of thin films, the growth can proceed through three different modes (Bauer, 1958) as shown in Fig. 2.2.

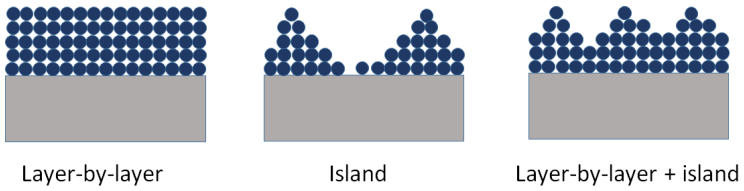

Figure 2.2: **Different epitaxial growth modes:** (left to right) Layer-by-layer growth mode, island growth mode and layer-by-layer + island growth mode.

The first one is called a layer-by-layer growth mode, where a unit-layer completely covers the surface before the growth of the next unit-layer. The next growth mode is the island growth mode, where the film starts to grow from a nucleation center such that it forms 3D multilayered islands. Only when these islands grow bigger and coalesce, then the entire surface of the film is covered. The third growth mode is an in-between mode between layer-by-layer growth mode and island growth mode. In this mode, first few layers grow in layer-by-layer mode and then growth mode changes to island mode. The growth mode by which an epitaxy proceeds is mostly determined by the competition to minimize the surface energy (by energy we mean Gibbs free energy) of the epitaxial system (See (Freund and Suresh, 2004) and references therein). If we denote the surface energy between thin film and vacuum, thin film and substrate, and substrate and vacuum as λ_{FV}, λ_{FS} and λ_{SV}, respectively, then layer-by-layer growth occurs when $\lambda_{FV} + \lambda_{FS} \leq \lambda_{SV}$. Qualitatively it is easy to see why this should be the case. If λ_{SV} is larger than the sum of other two, then by covering the substrate surface with film, the overall energy can be reduced. This means

that the impinging atoms will move around and wet the entire surface of the film, which leads to layer by layer growth. If on the other hand $\lambda_{SV} < \lambda_{FS} + \lambda_{FS}$ then it leads to island growth mode. For the layer-by-layer + island growth mode, after growth of first few layers, the surface energy considerations change from one that favors layer-by-layer growth mode to one that is favorable for island growth mode due to strain relaxation effect. Strain appear in heteroepitaxial growth when the bulk value of the surface lattice constant of the film is different from that of the substrate. If the lattice mismatch is small enough, initially the film is strained to match the lattice spacing of the substrate and can still grow in layer by layer mode. As the film grows thicker, after some critical thickness the strain is relaxed, typically by forming defects such as edge dislocations, as the energy cost of latter would be lower than energy required to maintain the strain energy. At this point the island growth mode becomes preferential to the layer-by-layer growth mode.

Defects and dislocations

Any real material system has defects and disorder in it. Epitaxial thin films can have different types of defects as a result of growth conditions. Defects are broadely classified into four types based on their dimensionality: point defects, line defects, planar defects and bulk defects.

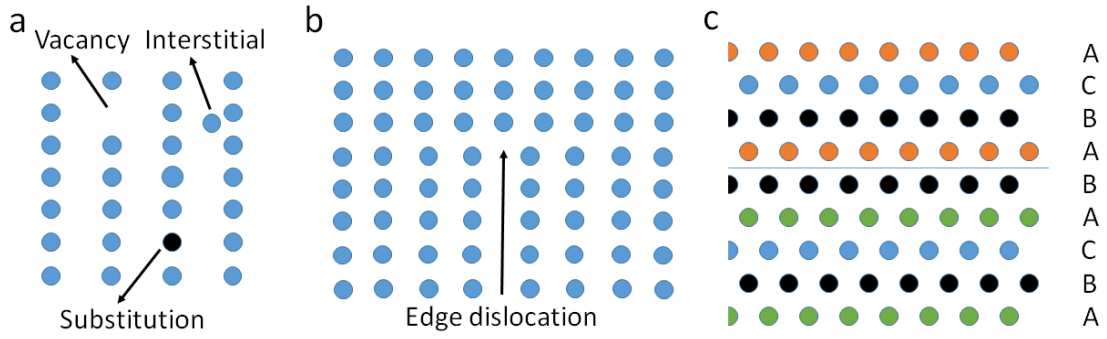

Figure 2.3: **Point, line and planar defects:**(a) substitution, interstitial and vacancy defects are point defects (b) Edge dislocation is a line defect (c) stacking fault ABCA[BA]BCA is a planar defect.

Here we will give a brief example of each. Point defects are created around a single

lattice point and do not extend in space in any dimensions. These defects could be due to misalignment of an atom from its lattice position (interstitial), absence of an atom from its position (vacancy) or a foreign atom in place of a regular atom (substitution). Such defects are created either thermodynamically or due to presence of impurity species during the growth of the thin film. Since they are localized in space, their dimensionality is 0D.These are shown in FIg.2.3a. Line defects are defects along some crystallographic direction of a crystal and therefore 1D in nature. An example of line defect is the edge dislocation shown in Fig.2.3b. Another example of line defects is screw dislocation, where the crystal planes move helically along a linear defect (sort of like a screw; hence the name). Planar defects can occur along the grain boundaries, where different grains grow along different directions. Examples of planar defects are antiphase defects, stacking faults and twin boundary. As shown in the Fig.2.3c, a stacking fault is where the normal ordering of a closed packed crystal structure ..ABCABCABC... has a planar shift leading to ordering of the type ...ABCABABC..... . On the other hand, a twinning-defect is one which introduces a plane of mirror symmetry in the ordering of crystal structure. Finally bulk defects are 3D macroscopic defects such as cracks, voids-which are clusters of vacancies, and precipitates- which are usually formed due to clustering of impurities resulting is a different phase compared to the rest of the film. Defects play an important role in determining electrical and structural properties of the thin films. Usually unintentional defects are deleterious to the electrical properties of the film and growth should be optimized to minimize these defects. On the other hand, sometimes defects are intentionally added to thin films to modulate the electronic structure of thin films. An example of this is doping by Al on GaAs to create GaAs-AlGaAs heterostructures, which then host high mobility 2DEGs that have found utility in various technological applications (See (Manfra, 2013)).

2.1.3 Different thin film growth technique

Having discussed the fundamental aspects of thin film growth, we next briefly discuss different methods of thin film growth routinely used in experiments throughout the world. In general, these methods can be categorized as chemical vapor deposition (CVD) or physical vapor deposition (PVD). In CVD, the constituents of the desired films are usually supplied

as part of volatile precursors, which react near the substrate to produce the desired film and also byproducts. These byproducts are then pumped away from the chamber. In contrast, in PVD constituent elements or molecules are physically ejected from the source by, for example, sputtering or heating and impinge upon the substrate. Since MBE, the growth method used in this work, belongs to PVD method, we will first discuss examples of CVD methods followed by other examples of PVD method. We dedicate a separate section for MBE.

X-CVD and ALD

X-CVD and atomic layer deposition (ALD) are some of the commonly used CVD methods for growth of thin films. A simple schematic of a general CVD system is shown in Fig 2.4. If the film we are trying to deposit is AB, then the precursor gases (AX and BY) containing species (A and B respectively) to be deposited are introduced to the growth chamber, which contains a substrate that is usually heated to optimal temperature. The reaction of these gases near and at the surface of the hot surface results in the deposition of the desired AB thin films. The byproducts of the reaction and residual gases are then pumped out of the chamber.

Due to fast growth rates and uniform deposition of films over large area, CVD is used extensively in production of various materials such as Si used in microelectronic applications (Simmler, 2000), high-κ dielectrics (Javey et al., 2002) and various metal thin films (Hampden-Smith and Kodas, 1995). Recently graphene (Kim et al., 2009) and TI thin films (Cao et al., 2012) have also been grown using CVD method. Given the broad range of materials grown using CVD, different variants of CVD exist.The prefix X- in X-CVD denotes the particular form of CVD used. For example, some CVD deposition are done in ultra high vacuum ($\sim 10^{-8}$ Torr) and are called UHV-CVD, while others are done at moderately low pressure of $\sim$ mTorr and are called LP-CVD, yet more are done with assistance from plasma to enhance the reactivity of precursor gases and are called PE-CVD.

ALD is a specialized version of CVD, where precursor gases are introduced into the chamber alternately. For example, for the growth of Al_2O_3, the precursors are $Al(CH_3)_3$ and H_2O. The reaction between these two species at the substrate leads to deposition of

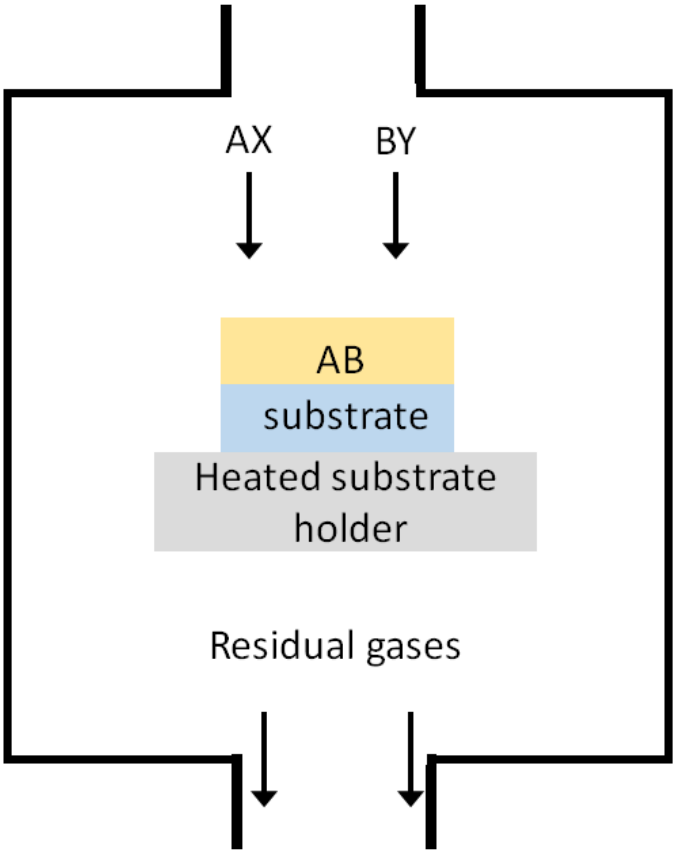

Figure 2.4: **Schematic of a basic chemical vapor deposition system:** Precursor gases are fed into the chamber, where they react in the vicinity of the heated substrate to form the thin film. Byproducts are pumped out from the chamber.

Al_2O_3. In ALD, these species are alternately introduced into the chamber. So for example, H_2O is intrduced to the chamber. Then it will wet the substrate surface, but rest of the H_2O do not stick on top of this wetting layer and are just pumped out of the system. Then, H_2O valve is turned off and $Al(CH_3)_3$ is introduced. $Al(CH_3)_3$ will react with H_2O at the substrate to form a monolayer of Al_2O_3. $Al(CH_3)_3$ will wet this layer but next Al_2O_3 layer will only grow when H_2O is introduced into the chamber again and the cycle continues. Therefore the growth is self-limiting and the thickness of the growing film can be simply controlled by controlling the number of such cycles. Thus, ALD is useful when ultrathin films with precisely defined thickness are required and is often used in deposition of gate dielectrics such as Al_2O_3.

Sputtering

Sputtering is an inexpensive PVD growth method that is used to grow polycrystalline, amorphous and single crystal thin films (Wasa, 2012). A simple schematic is shown in Fig.2.5. In sputtering, the source material and substrate are housed in a chamber which is fed with ∼100 mTorr of heavy and inert gas such as Ar. Ar plasma is created in the sputtering process by stray electron that gets accelerated due to the applied bias voltage between the source and the substrate. If and when it hits a Ar atom, it knocks off an electron from the atom. This process creates two electrons and a Ar^+ ion. If there are enough Ar atoms around, then a Ar plasma is created due to cascading effect. Ar^+ ions are then accelerated towards the source material due to negative potential at the source material with respect to the substrate. The Ar^+ ions with energy on the order of ∼1 keV bombard the source material and knock off source particles near the surface of the source. These particles usually have kinetic energy on the range of ∼10 eV, which then impinge onto the substrate. Due to low efficiency of ionization process, in order to sustain the plasma, Ar

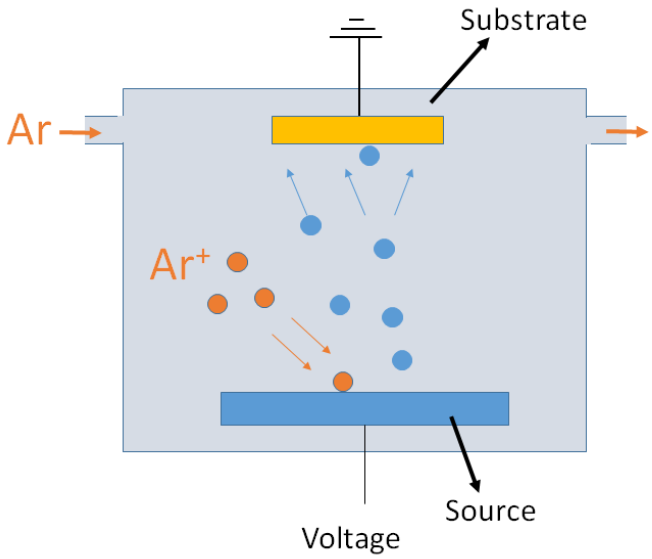

Figure 2.5: **Schematic of a sputtering system:** Argon ions bombard the source ejecting off source particles, which get deposited to the substrate.

pressure of ∼100 mTorr is required in a conventional sputtering system. Modern sputtering systems make use of parallel magnetic field at the surface of the source material to confine

electrons near the source material. Such sputtering set-up, known as magnetron sputtering, have high ionization rates leading to higher deposition rates and can be operated at ∼1 mTorr of Ar pressure. The relatively high pressure of (magnetron) sputtering chamber leads to thin films having significant impurities compared to other PVD systems, which operate at much lower pressure. Furthermore, the high energy of impinging species on the substrate can actually knock off already deposited thin film, which is known as resputtering. Since resputtering rate is material dependent, this could lead to loss of stoichiometry of the deposited thin films.These effects can have serious consequences for experiments where high quality of the film is desired. On the other hand, sputtering is a cheap and quick thin film growth method. Furthermore, sputtering can ablate any material and therefore can be used to deposit almost all materials, which is not always easily accomplished with other PVD systems like MBE.

Pulsed Laser deposition

PLD is a PVD system, where series of intense laser pulses are shone on the source material to evaporate it (See (Christen and Eres, 2008) and references therein for a thorough discussion on PLD). The interaction between laser and source material leads to thermal, mechanical and chemical energy at and near the surface of the source material, which then evaporates and ablates leading to creation of plasma plume, which in addition to the neutral particles also contains ionic species as well as electrons. The vaporized source material then travels towards the (usually heated) substrate and under right conditions epitaxial growth of thin film commences. Each laser pulse is usually ∼picoseconds to nanoseconds long and is followed by ∼100 μs - 10 ms long break. This cycle is repeated and once other growth parameters are optimized, this repetition cycle determines the rate of film growth. A simple schematic of PLD setup is shown in Fig.2.6.

PLD has numerous advantages. Along with the ability to change the intensity, the wavelength of laser can be changed to provide maximal optical absorption for most materials, and therefore PLD can be used to evaporate almost all materials. In PLD, the source consists of the same material as the desired film and for many compounds PLD can transfer stoichiometry of the source material to the growing thin film. This is especially useful in

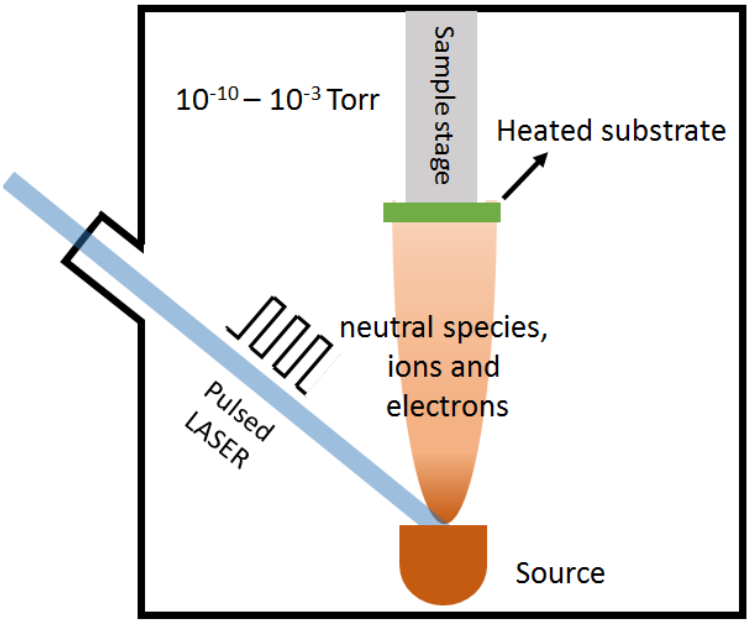

Figure 2.6: **Schematic of a PLD system:** Pulsed laser is shone on the source material, creating a laser plume consisting of neutral particles, ions and electrons, which then impinge upon a heated substrate leading to film growth.

deposition of multi-element compounds, where maintaining stoichiometry with PLD can be easier than other deposition systems where constituent elements are individually deposited to the substrate to form the thin film of the compound. Furthermore, a background gas can be used to enhance stoichiometry of a given film. For example, this process is routinely used in PLD growth of oxides, where PLD is carried out in (sometimes atomic or plasma) oxygen environment to minimized oxygen vacancies in growing films. In addition, the chamber pressure of the PLD system can be anywhere from $\sim 10^{-10}$ Torr to mTorr region depending upon the application. This usually low chamber pressure allows the use of RHEED, which gives real time information about the structural quality of the growing film. Such *insitu* characterization leads to very efficient control of growth parameters and film quality. Since, RHEED is an important part of MBE setup, we will discuss it in some detail in section 2.1.5. Finally, atomic scale control of film thickness can be achieved in PLD growth usually just by controlling the laser pulse. PLD has been very successfully used in growth of high quality films of perovskite based complex oxides such as high temperature

superconductors (Christen and Eres, 2008) and $LaAlO_3$ - $SrTiO_3$ hetreostructures (Ohtomo and Hwang, 2004).

On the other hand, there are some disadvantages to PLD growth. One major drawback is possibility of deposition of particulates (which are pieces of particles upto μm in size) in the growing films, which act as defects in the film and , therefore, are undesirable. Such particulates can be are formed when the material just underneath the surface melts resulting in 'splashing' of droplets of particles. Due to relatively high kinetic energy of ejected particles ($\sim$1 - 10 eV), inter-layer mixing and resputtering can occur during film growth, which can lead to broadened interface for heterostructures and loss of stoichiometry for some materials.

2.1.4 Molecular beam epitaxy[1]

Overview

MBE is a technique for thin film growth on substrates, where elemental sources are heated to produces beams of thermally evaporated (or sublimated) vapor, which adsorb and react at the substrate surface to create epitaxial thin films of desired elements or compounds. For a thorough review of MBE and history of its development, see (Henini, 2012). Here we will outline some of the important ascpects of MBE.

MBE allows atomic scale control on thickness and composition of growing films and is suited for growth of heterostructures, where precise control of layer thickness, interface sharpness and doping concentration are needed to produce desired electronic properties. The chamber pressure of MBE is usually $\sim 10^{-11}$ - 10^{-8} Torr, which is called the ultra high vacuum (UHV) range. This leads to minimal incorporation of unintentional impurities in the growing film. The thermal evaporation process used in MBE produces particles with much lower kinetic energy ($\sim$50 meV) compared to sputtering and PLD, which avoids the problem of resputtering and defect formation sometimes associated with those techniques. Furthermore, the low energy nature of thermal evaporation inherent to MBE leads to very

[1] **Following discussions are based on MBE system in Prof. Oh's lab at Rutgers Univeristy. Other MBE systems can be considerably different in details, but they share the same basic principle of operation described here.**

stable flux of particles against source heating temperature, which makes it very convenient to control the flux of each element by just adjusting the source heating temperature. The real time information of the structural quality of growing films using RHEED helps to optimize growth parameters in an efficient manner.

MBE system: Load lock, Preparation and MBE chambers

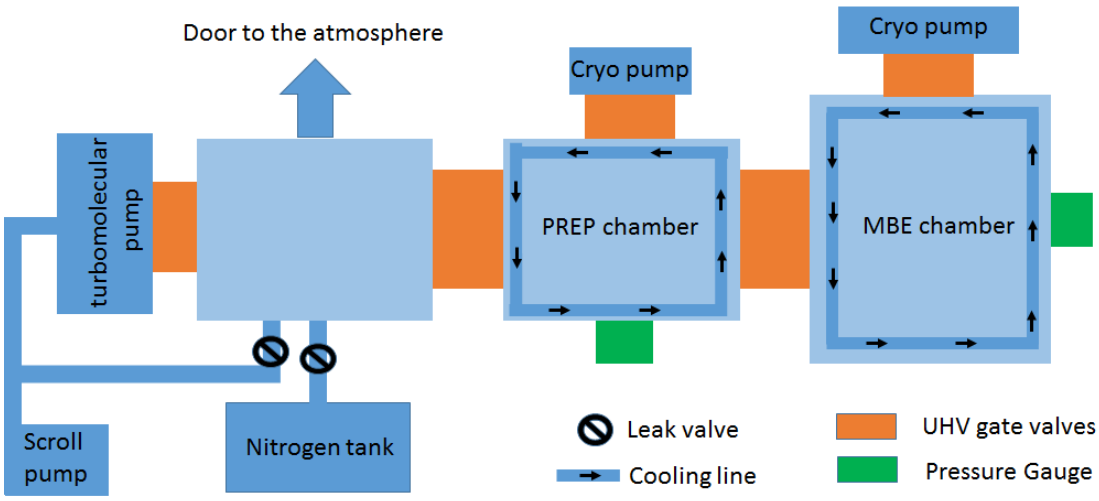

Figure 2.7: **Schematic of a typical MBE system:** A MBE system consists of three chambers: load-lock, preparation and MBE, which can be isolated from each other by UHV gate valves. A combination of pumps is used to attain different vacuum levels, which are monitored using pressure gauges.

As shown in Fig. 2.7, a typical MBE system (like the one at Rutgers University) consists of three chambers that can be isolated from each other using UHV gate valves. We will first explain each component and then discuss their roles in the context of a typical growth cycle of MBE. The MBE chamber, where films are grown, is pumped by a cryogenic pump (or simply cryopump) and contains a pressure gauge to monitor the chamber pressure. Cryopumps operate on a simple principle: gaseous particles condense and get trapped on a cold surface. Essentially, a stage with large surface area is cooled to ∼10 - 20 K, which then traps residual gases and brings down the pressure of the chamber upto $\sim 10^{-10}$ Torr. Since, large amount of gases trapped on the surface can significantly reduce the pumping

speed of a cryopump, they are almost always used below $\sim 10^{-4}$ Torr in order to minimize such effect. For this reason, a UHV gate valve is installed between a cryopump and the chamber so that when the chamber is vented the valve can be closed and the cryopump can be isolated, which dispenses the need to turn off cryopump during such venting event. We mention that other types of pumps such as ion-pumps and turbomolecular pumps are sometimes used in a MBE setup, but we will not discuss them further. In order to reduce the base pressure of the MBE chamber, the chamber walls are usually cooled with water or liquid nitrogen, which also helps to trap the residual gases. Pressure gauge installed in the MBE chamber helps to monitor the chamber pressure. Since MBE chamber pressure is typically less than $\sim 10^{-6}$ Torr, the preferred pressure gauge is the ion gauge, which are suited for measuring pressure in the range of $\sim 10^{-3}$ - 10^{-10} Torr. An ion gauge works by ionizing the residual gases, which then carry current between anode and cathode of the ion gauge. This current is then proportional to the amount of residual gases on the chamber. With (factory-set) proper calibration, the chamber pressure is then known.

Since a key requirement for achieving high quality films is to maintain UHV, it is imperative that the MBE chamber not be exposed to the atmosphere on a regular basis. The other two chambers are included in a MBE system partly due to this reason. A preparation chamber (usually abbreviated to prep chamber) is pumped in exactly the same way as the MBE chamber and is used for sample/substrate preparation. The final chamber is the load-lock chamber, which is frequently exposed to the ambient conditions when substrates are put into the system or when samples are taken out of the system. This chamber is pumped by either a turbomolecular pump or a scroll pump depending upon the pressure of the load-lock chamber. The load-lock is also connected to an inert gas source such as high purity N_2 gas tank, which is required during the venting of the load lock.

We will now explain how these units work during a typical growth cycle of a MBE system. Lets start from the situation prior to putting a new substrate for the film growth. At this point the door to the atmosphere is closed so that the entire system is isolated from the atmosphere and the UHV gate valves connecting the chambers and the leak valves are in closed position. The UHV valves connecting each chamber to the pumps (cryo or turbo) are open. In order to put the new substrate, we have to vent the load-lock to

atmospheric pressure. In order to do so, the UHV gate valve between the load-lock and the turbomolecular pump is closed and the valve to the N_2 gas tank is opened, which fills up the load-lock. When the load-lock is fully vented, the door can be opened and the new substrate can be inserted into the substrate holder. During this time, the valve to N_2 gas tank is kept open to maintain a positive pressure in the load-lock chamber so that there is a constant flow of N_2 from the load-lock to the atmosphere. This process minimizes flow of atmospheric gases into the load-lock and thus helps to prevent contamination of the chamber. Once the new substrate is put into the load-lock chamber, the door is sealed and N_2 valve is closed. While pumping down the load-lock from ambient pressure, first the scroll pump is used to pump it down to $\sim 10^{-3}$ Torr at which point the turbomolecular pump is used to lower the pressure down to $\sim 10^{-5}$ - 10^{-7} Torr. After this, the UHV gate valve between the load-lock and the prep chamber is opened and the substrate is transferred onto the prep chamber after which the UHV gate valve is closed. The pressure in the prep chamber is usually $\sim 10^{-9}$ Torr, but during the substrate transfer it can rise by two order of magnitude due to exposure to the load-lock chamber. Once the base pressure of the prep chamber is attained, the substrate is then transferred from the prep chamber to the MBE chamber. A reverse process is used when taking a sample out of the MBE system. In this way the UHV of the MBE chamber is always maintained.

MBE chamber: Components and Processes

A schematic of a typical MBE chamber is shown in Fig.2.8. It consists of sample stage, effusion cells,various pumps and RHEED setup. The sample stage lies along the axis of the cylindrical chamber and is equipped with a heater so that the substrate can be heated. The substrate is loaded onto the sample stage facing down and can be rotated during growth to maximize the uniformity of growing film. The effusion cells contain crucibles, which house elements needed for a film growth. They are placed uniformly around the lower panel of the MBE chamber and all of them face towards the substrate. Usually elemental sources with purity greater than 99.99% are placed in crucibles, which are made up of materials such as pyrolitic boron nitride, alumina, quartz or tantalum. These are high-temperature resistant materials and suitable for use as crucible. The inside of the effusion cells contain

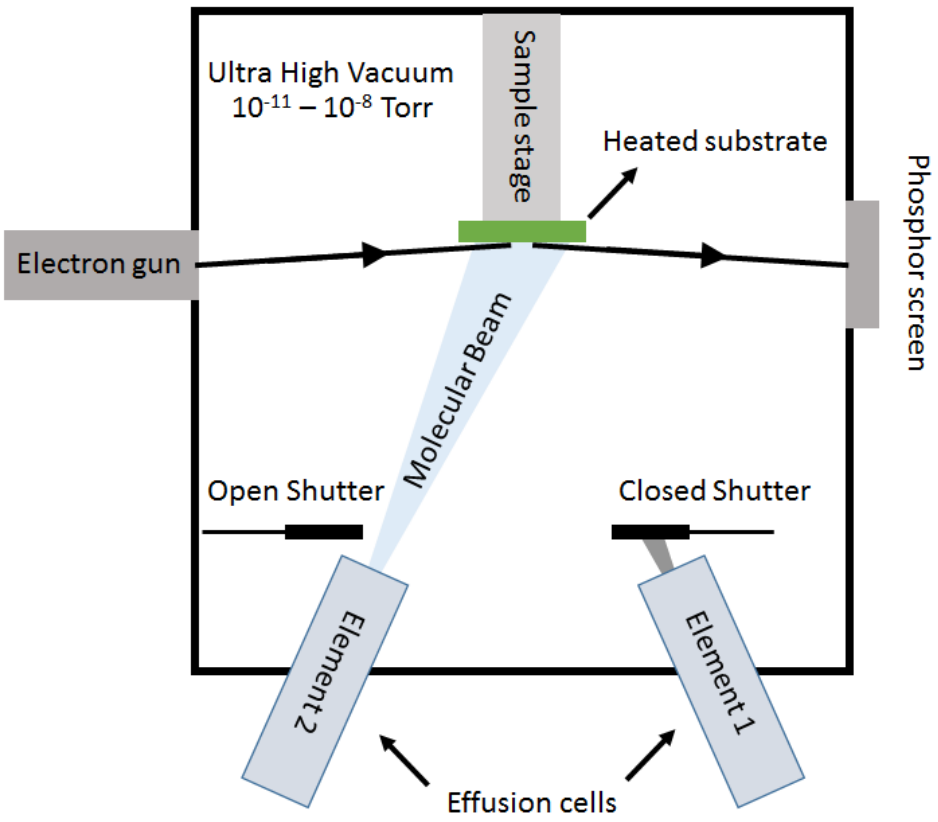

Figure 2.8: **Schematic of a MBE chamber:** In an UHV environment, sources are heated to create molecular beam which impinge on substrate for film growth. RHEED setup is also shown.

heating filaments, which are used to heat the element to the desired temperature. At this temperature, elements start to evaporate (sublimate). Due to the ultra high vacuum environment, the evaporating particles (on average) do not scatter off of each other or residual gases in the MBE chamber while traveling from source to the substrate. The average distance before particles scatter i.e. the mean free path (l) can be estimated using $l \sim 5 \times 10^{-3}/P$, where l is in cm and chamber pressure (P) is in Torr (Henini, 2012). For typical operating pressures of MBE chamber $\sim 10^{-9}$ Torr, l is on the order of km, while the source to substrate distance is on the order of tens of cm. This ballistic motion means that particles travel in a line-of-sight, thus creating a molecular beam. On top of each cell there are mechanical shutters, which can be opened and closed either automatically or manually.

The opening and closing of the shutter determines whether a particular element is deposited to the substrate or not.

There is a one to one correspondence between the temperature of the cell and the amount of evaporation of the elements. Usually the amount of evaporating material is quantified in terms of beam flux, which is the number of atoms (molecules) of an element that impinge on a surface of unit area per unit time. The beam flux can be measured directly and this information can be used to determine the growth rate of the film as follows. If the crystal structure of the desired film is known, we can calculate the areal density of atoms (ρ_{areal}) in the film. Then the time taken to grow a unit layer of the film is $\frac{\rho_{areal}}{beam flux}$. A simple estimate of the growth rate can be made by noting the fact that the areal density of atoms in crystals is usually $\sim 10^{15}$ cm^{-2}. This means that to grow a unit layer of a thin film every $\sim$minute, we need $\sim 10^{13}$ cm^{-2}s^{-1} of beam flux.

In situ and *ex situ* measurement of beam flux

Since accurate measurement of beam flux is crucial not only to determine the growth rate of the film but also to determine the composition of a film, it is imperative that flux be measured as accurately as possible. MBE is usually equipped with a dedicated device to measure the beam flux of evaporating elements. One such device is called a quartz crystal microbalance (QCM), which is capable of detecting minute changes in mass. During QCM measurement, the substrate is moved away from its usual growth position. Instead the QCM head (which contains the quartz crystal) is moved to that position. When molecular beam impinges on the QCM, the depositing film of the element continuously increases the mass of the crystal, which is then measured to give the beam flux.

Quartz is a piezoelectric material, where an application of electric field can create mechanical stress on the material. In a QCM, a gold-coated flat piece of quartz is used. The alternating electric field applied across a quartz using gold electrodes creates transverse oscillation of the system. When, film is deposited on the quartz, the resonance frequency of this oscillation decreases with increasing mass of the system and can be measured. This shift in frequency (Δf) is converted to increase in mass (Δm) using Sauerbrey equation (Sauerbrey, 1959), which states: $\frac{\Delta m}{mass_{initial}} = \frac{\Delta f}{f_{initial}}$. Given the area of the quartz crystal

and mass density and atomic mass of the element being deposited (all of which are known) the flux is easily calculated. Since, the QCM is sensitive to changes in frequency of ∼1 Hz (the resonance frequency is usually on the order of ∼MHz), it can be extremely accurate in measuring flux. We mention that QCM measurement is susceptible to temperature changes of the crystal during measurement due to the radiative heating from the heated cell. To minimize this effect the QCM housing is continuously water-cooled to maintain it at a constant temperature. To further minimize uncertainties QCM measurement can be compared against *ex situ* flux measurement techniques periodically. The growth rate and composition of thin film can be measured *exsitu* by using Rutherford back scattering (RBS). While, RBS is not usually available at many labs, Rutgers maintains its own RBS system, which allows for easy access to RBS measurement.

For RBS measurement, a test film is usually grown such that the film thickness is less than ~ 50 nm or so, which is the thickness regime for which RBS gives the best quantitative result (Zangwill, 1988). The flux value obtained from RBS, which is the true flux within measurement uncertainties, can now be compared to QCM values and a calibration factor can now be established. The calibration factor is just the ratio of the flux measured by RBS to that measured by QCM. Once the calibration factor is found for an element, then the QCM measurement is usually sufficient to give accurate fluxes within $\sim 1\%$. Ideally, such calibration factors should be established when using an element for the first time. In our lab, we use QCM and RBS as the primary methods of establishing beam flux and growth rates.

2.1.5 Strucutral characterization

Reflection high energy electron diffraction

Characterizing the structural quality of thin films is an important aspect of thin film growth. In this regard, reflection high energy electron diffraction (RHEED) is probably the most powerful tool in MBE growth setup because unlike most other structural characterization tools, RHEED is usually housed inside MBE chamber and is tailored to probe the surface of the growing thin film. RHEED provides information on morphology and crystallinity of

the film in real time, which means that one can optimize the sample growth parameters to obtain better film quality in real time. Compare this to the case where RHEED is absent and only *ex situ* characterization is possible. Here one is blind to the quality of the film during the growth and any structural characterization can only be made once the sample is taken out of the MBE chamber. Based on this information, the next sample has to be grown blindly with updated growth parameters and again the structural characterization is only possible at the end of the growth. This process is time and resource consuming and signifies the true power of RHEED for MBE growth of thin films.

Figure 2.8 shows a schematic of RHEED set up in a MBE system. Electron beam with energy of $\sim$ 5 - 20 keV are generated by an electron gun and impinge on the sample at a glancing angle of less than $\sim 1^o$. The electrons get diffracted from the sample and the outgoing beam land on a phosphor screen, which fluoresces. This image is captured by a CCD camera, which is fed to the computer for analysis using commercially available software. In our set up, the beam energy is fixed at 10 keV and the beam width is on the order of 1 mm, which means that a macroscopic portion of the film is sampled ensuring that the RHEED captures the crystalline structure of the sample as a whole rather than a small local spot.

RHEED is an exceptionally surface sensitive tool, which can be understood in terms of the geometry of RHEED and short mean free path of electrons in the sample. As shown in Fig. 2.9 mean free path of electrons in a solid follow a universal curve that is nearly material independent. Since the minimum mean free path is around $\sim$ 5Å for electron energy $\sim$ 50 eV, this is the desired electron energy so that only the electrons that penetrate upto $\sim$ 5 Å are elastically scattered. Since RHEED is a diffraction process, primarily elastically scattered electrons partake in interference phenomena and hence essentially diffraction results from sample depth less than the mean free path of the electrons. Given that $\sim$ 5 Å corresponds to at most a few unit-layers of a film, this sample depth represents only the topmost layers of the growing film, which is why RHEED is surface sensitive. But if the universal curve for mean free path shows lowest mean free path for $\sim$50 eV electrons, how does this correspond to high energy of $\sim$10 keV used in RHEED? The answer lies in the geometry of RHEED setting. Because the electrons impinge the sample at a glancing angle of 1^o, the momentum

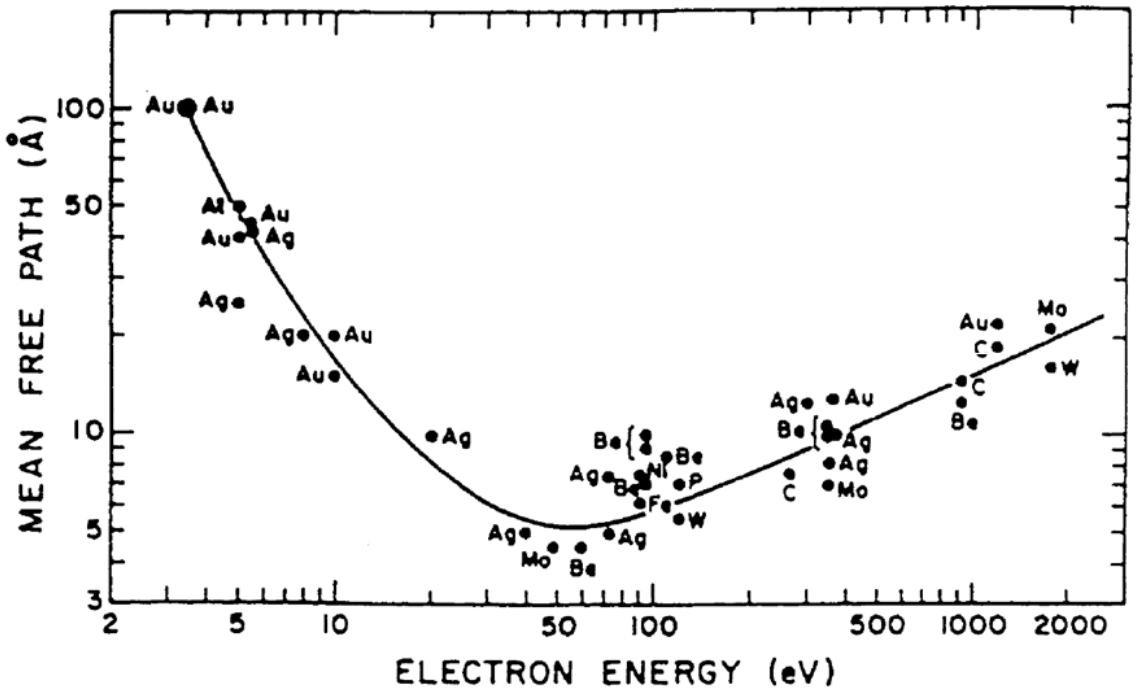

Figure 2.9: Electron mean free path within a solid as a function of kinectic energy of the impinging electrons.Adapted from (Zangwill, 1988).

of the electrons in the film normal direction is $\sim\sin(1^o)$ of the incident momentum. Hence the kinetic energy corresponding to normal component of the momentum is actually ∼50-100 eV, while rest is associated with the momentum parallel to the surface. According to the universal curve shown in Fig. 2.9, the electrons can then travel far along the surface of the film, without penetrating too deep into it.

Due to its surface sensitivity, RHEED can be used to get information about the surface morphology, growth mode of the thin film, surface lattice constant, strain and in certain cases even rate of film growth. First we will discuss the basics of RHEED. Like any other diffraction phenomena, RHEED is governed by the fact that the constructive and destructive interference between scattered waves depend on the path difference. Constructive interference occurs when the path difference is a multiple of the wavelength of the diffracted waves, while destructive interference results from path difference of half wavelength. This relation is mathematically captured by Bragg's law, $dsin\theta = n\lambda$, where d is the lattice spacing, θ is the angle of incidence (or reflection) and λ is the wavelength of the electrons, which is on

the order of few $\AA$ at 10 keV.

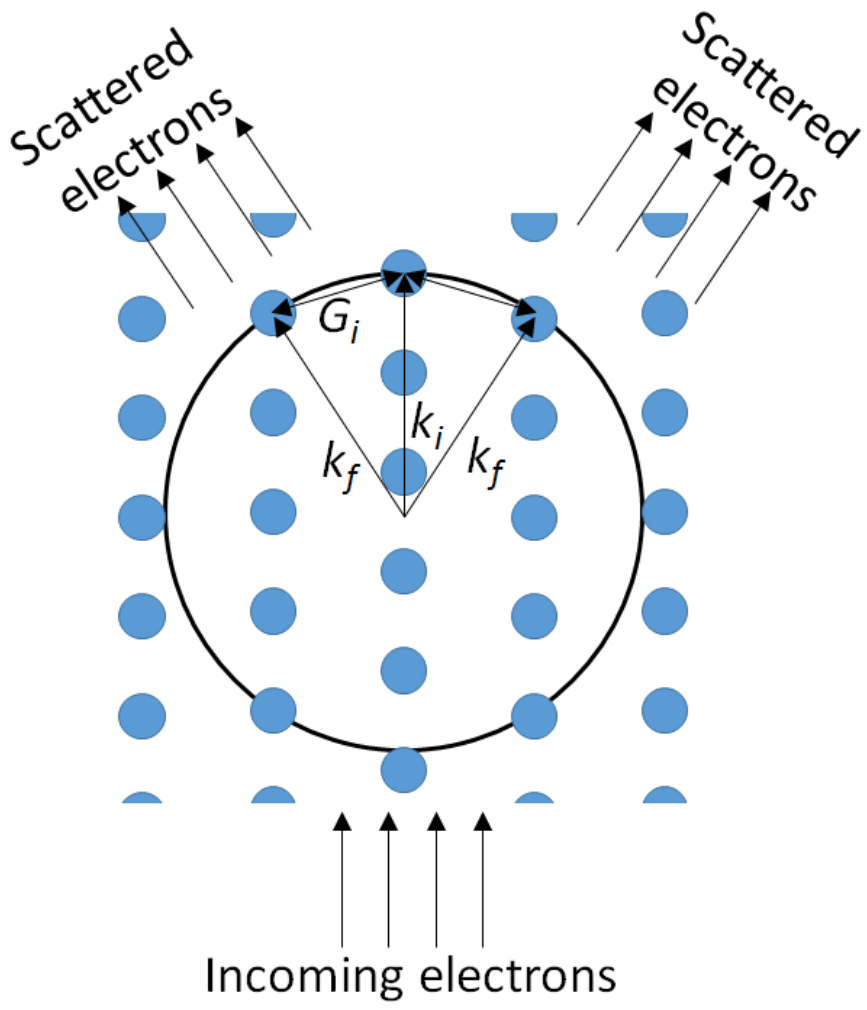

Figure 2.10: **Ewald construction:** (top view) When lattice points of recirocal lattice intersect the Ewald sphere, then the Laue condition $\Delta k = G_i$ is satisfied resulting in constructive interference.

A more intuitive way to visualize RHEED is through Ewald construction as shown in Fig 2.10. First start out by drawing a sphere with radius $k_i = 1/\lambda$, this is the Ewald sphere, where k_i is the wave-vector of the impinging electrons. As we will see later, Ewald sphere simply gives the elastic scattering criteria i.e. $|\boldsymbol{k}_i| = |\boldsymbol{k}_f|$, where $|\boldsymbol{k}_f|$ is the wave-vector of the scattered electrons. Since RHEED is only surface sensitive, for a smooth film surface RHEED electrons usually *see* a 2D lattice. We next draw the reciprocal lattice space (top view) and superimpose it on the Ewald sphere. All the lattice points that intersect the

sphere give the condition for diffraction to occur. This is in fact the pictorial representation of Laue's condition i.e. $\boldsymbol{k}_i - \boldsymbol{k}_f = \boldsymbol{G}_i$, where $\boldsymbol{G}_i$ is the reciprocal lattice vector. We emphasize that Bragg's Law, Ewald's construction and Laue's equation are equivalent descriptions of the same physical phenomena. This argument also applies to the 3D crystal case as is well known from introductory solid state course. However, as shown in Fig. 2.11 there is a big difference between the reciprocal lattice of a 3D crystal versus 2D surface, which will be useful to understand.

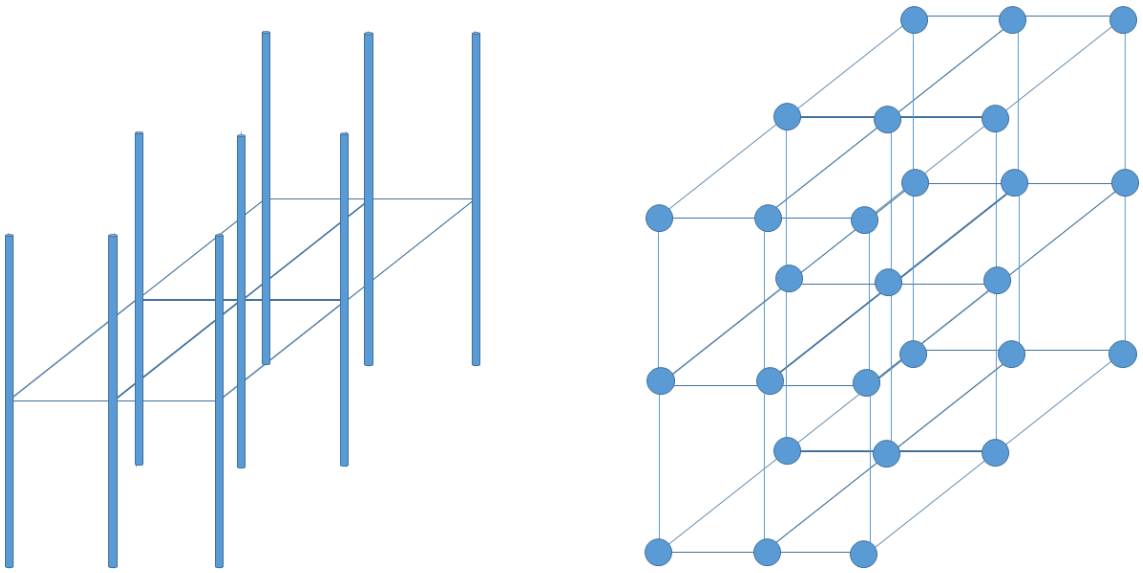

Figure 2.11: **Reciprocal space of 2D versus 3D features:** Reciprocal lattice from (left panel) a 2D surface showing reciprocal rods that extend along the third dimension while (right panel) those from 3D crystals appear as discrete points along the third direction.

The reciprocal transformation of 3D crystal leads to a lattice with well defined lattice points. On the other hand, for a 2D surface, since the third dimension is truncated in real space it leads to the elongation of lattice points in the third dimension of the reciprocal space. An intuitive way to look at this is that a surface is localized in third direction. In ideal case this represents a delta function, whose Fourier transform yields constant value in Fourier space, which leads to elongation along third dimension in the reciprocal space. Therefore, surface reciprocal lattice looks like a series of rods whose axes lie along the third direction. These rods are aptly named reciprocal rods. It is clear that the diffraction pattern in RHEED from a 2D surface versus 3D crystal lattice will show this difference between

their corresponding reciprocal lattice.

The surface of a growing film can be smooth (this is true for layer by layer growth) or it can be composed of 3D islands (this is true for island growth). For the former RHEED electrons *see* a 2D lattice and the diffraction pattern is formed along the points where the reciprocal rods cross the Ewald sphere. Upon rotation of the sample, the reciprocal rods move along the vertical direction of the phosphor screen, while continuously crossing the Ewald sphere. Therefore the diffraction peaks will trace a vertical line along the screen in a continuous fashion. This is shown in Fig. 2.12a, where a diffraction from flat surface leads to sharp streaks.

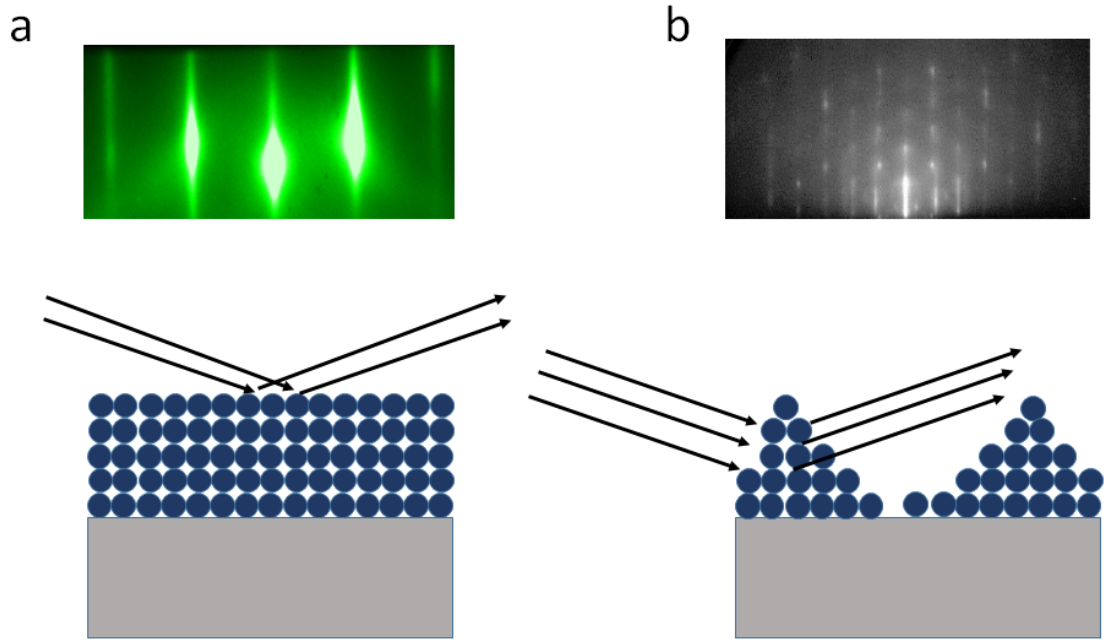

Figure 2.12: **RHEED diffraction from 2D versus 3D features:** (a) RHEED pattern from a flat 2D surface appear as sharp streaks, while (b) those from 3D islands appear as multiple spots along a vertical line. Figure (b) adapted from (Tanikawa et al., 2001)

On the other hand when the surface is not smooth and has 3D features in it, electrons can penetrate these structures and form a transmission diffraction pattern. Since the reciprocal lattice of the 3D crystal is composed of discrete points, when the sample is rotated, the lattice points move up and down but the diffraction pattern only appears when one of them intersects the Ewald sphere. The discreetness of the lattice points corresponds to

discreteness of diffraction pattern, where under sample rotation the diffraction patterns blink on and off rather than continuously tracing a vertical path, which was the case for 2D flat surfaces. Furhtermore, even if the sample is not rotated, the discreetness of 3D lattice can be seen as shown in Fig. 2.12b, where spots are clearly visible along the vertical line. In addition, RHEED pattern also give a lot of other useful information about the quality of the crystal surface. For the highest quality single crystals such as those used as substrates for MBE growth of thin films, the diffraction patterns are sharp and crisp. Qualitatively, the diffraction spots become sharper and crisper as the surface becomes smoother and also when domain size of the crystals increases. In addition to these diffraction spots there are lines in diagonal direction that are visible in RHEED pattern of single crystal, which are known as kikuchi lines. These kikuchi lines form due to diffraction from inelastic electrons and their presence indicates a high degree of crystallinity of the sample (Ichimiya and Cohen, 2004).

Apart from the morphology of the growing film, RHEED can give quantitative information about the crystal structure of the growing film. One of the routinely extracted quantity from RHEED pattern is the in-plane lattice constant of the growing films. By measuring the distance between 0th order and 1st order diffraction spots in RHEED pattern and by accurately measuring the distance between sample and the screen, we can get the scattering angle of the diffracted electrons. Bragg equation can now be used to find the lattice constant of the film. On the other hand, we can know the lattice constant of the growing film just by comparing the diffraction pattern of the film to the diffraction pattern of the substrate. For this the lattice constant of the substrate must be known and they should share the same surface lattice symmetry. Both of these two criteria are usually true for MBE growth. Now we can simply measure the spacing of diffraction spots from substrate and the film, which are proportional to their corresponding reciprocal lattice vectors. The ratio of these two numbers must be equal to the inverse of the ratio of their corresponding lattice constants (since reciprocal lattice vectors are inversely proportional to real space lattice constants). Since the substrate lattice constant is known, now the in-plane lattice constant of the film can also be determined.

Finally we mention that for layer-by-layer growth mode, the growth rate of the film can be determined from the oscillations in RHEED intensity, which have the same periodicity

as the time needed for growth of a unit layer of the film. This can be easily understood from following argument. At the beginning of a growth of the next layer of the film the surface is smooth leading to brighter RHEED pattern. When the next layer starts to grow, the surface looks rougher due to incomplete coverage of the film by the growing layer. Finally when the layer is complete, the surface becomes smooth again and the intensity increases again. Thus the intensity oscillates with same rate as the growth rate of the thin film.

Complimentary *ex situ* characterization

Techniques such as atomic force microscopy (AFM), scanning tunneling microscopy (STM), X-ray diffraction (XRD) and transmission electron microscopy (TEM) are some of the *ex situ* tools used to probe the structure of a thin film. AFM, STM and TEM directly measure quantities associated with real space of the film such as film morphology, grain boundaries and defects and are therefore in some sense are considered local probes. On the other hand, XRD being an interference phenomena gives information about the reciprocal-space of the thin film, which gives information about crystallinity of the film on a global scale. Altogether these techniques help to determine the structural quality of thin films and provide critical feedback to optimize the growth parameters to obatain highest quality thin films. We will briefly discuss some of the *ex situ* tools that are commonly used during our thin film growth process.

AFM is used to measure the profile of the surface of a sample, which is known as surface morphology. As the name suggests, AFM ultimately relies on the force that atoms feel when they are brought close to each other. In this case, a measurement tip that is attached to a cantilever is brought close to the sample surface. The tip begins to feel the force from the atoms at the surface, which being short ranged in nature strongly depends on the distance between tip and the surface. If a sample surface is not smooth, which is usually the case for any real material, as the tip is moved laterally across the sample surface, the force on the tip changes with the change on the height of the sample surface. In experiments, the tip-sample distance is kept fixed by monitoring the deflection of cantilever, which is used to control piezoactuators that move the sample vertically to maintain constant deflection of the cantilever. The signal from the piezoactuators are then used to determine the height

of the sample surface as a function of the lateral directions. This produces a 3D map of the surface. AFM is thus an useful tool in determining the morphology, surface roughness and grain size of thin films.

In addition to AFM, XRD is another powerful tool that is commonly used to figure out the crystal structure and phases of bulk crystals and thin films. Being a diffraction phenomenon, the argument used for analysis of RHEED also applies here. However, XRD is mostly used as a bulk probe rather than surface sensitive probe, since X-rays easily penetrate ~ 100 μm into most materials. For Bi_2Se_3 thin films, which always grow in one particular crystallographic direction without formation of secondary phases, the primary use of X-ray is to extract the out of plane lattice constant of the film. Due to this reason, we sparingly use XRD in our film growth.

STM can measure the topography of a sample surface on atomic level. This is achieved by voltage biasing a atomically sharp metallic tip that floats few Å away from the sample surface and measuring a tunneling current between them. This current depends upon the tip-sample separation and the local density of states of the sample. In order to measure the topography, the tip can be moved across the sample surface. At the same time, a feed-back control loop adjusts the tip-sample separation in order to maintain a constant current through the tip. The resulting change can then be imaged as change in sample height. The tunneling nature of STM measurement requires that the sample be conducting with extremely clean surfaces (UHV condition). In many cases STM chamber and MBE chambers are connected so that the sample can be measured without breaking vacuum.

2.1.6 Growth considerations for pnictogen chalogenide TIs

The prototypical family of pnictogen chalcogenide TIs such as Bi_2Se_3, Sb_2Te_3 and Bi_2Te_3 are all layered materials just like graphite. A material is considered as layered if within a layer there is strong chemical bonding between the atoms, while between adjacent layers the bonding is weak Van der Waal's type. This very weak out of plane bonding leads to very different epitaxial rules for these materials compared to epitaxy of (conventional) covalently bonded compounds such as GaAs. Epitaxial growth of such layered materials is called van der Waal's epitaxy (Koma et al., 1984). Here we will discuss some of the features of this

type of epitaxy in the context of growth of Bi_2Se_3 on Al_2O_3.

Van der Waal's epitaxy

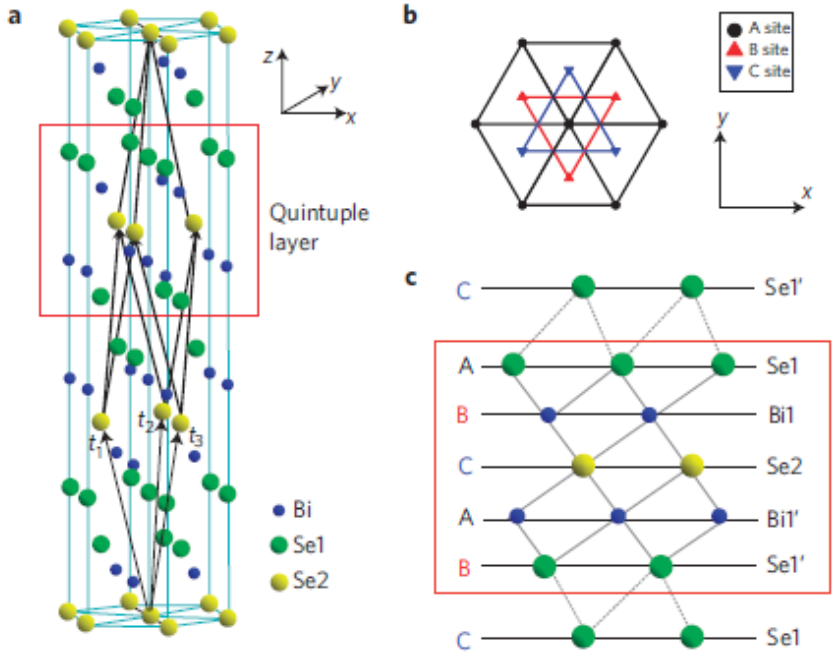

Figure 2.13: **Unit cell of Bi_2Se_3:** (a) primitive rhomohedral and conventional hexagonal unit cell (b) top view of the arrangement of atoms and (c) side view of a quintuple layer consisting of -Se-Bi-Se-Bi-Se- stacks. Figure taken from (Zhang et al., 2009).

Bi_2Se_3, Sb_2Te_3 and Bi_2Te_3 all share the same rhombohedral crystal structure as shown in Fig. 2.13a for Bi_2Se_3. While the primitive unit cell is the rhombohedral cell, it is often easier to visualize them in hexagonal unit cell basis, both of which are shown in Fig. 2.13a. The first thing to notice is that along the c-axis (z direction), the crystal is composed of repeated stacking of -Se-Bi-Se-Bi-Se- units. This unit is called a quintuple layer (QL; see Fig. 2.13c) and is ∼1 nm in height. The chemical bonding within the QL is of strong covalent type, while two adjacent QLs are held together by a weak Van der Waals type bonding. During epitaxy of these TI materials, the films always grow along the c-axis and therefore the layered nature comes to play an important part.

For heteroepitaxy of covalently bonded materials, due to strong bonding between the substrate and the film, and between additional layers of the growing film, lattice matching and surface crystal structures of the substrate are the most important criteria. Without a good fit of either of these requirements, such heteroepitaxy is almost impossible. On the other hand, for growth of layered materials, constraints in these criteria are far more relaxed. For example, this is seen from successful growth of epitaxial Bi_2Se_3 on variety of substrates with widely varying lattice mismatch. To name a few, Bi_2Se_3 has been grown on Al_2O_3(0001) (Bansal et al., 2012) and Si(111) (Bansal et al., 2011; Kim et al., 2011) which have ∼14% and ∼-7% mismatch compared to Bi_2Se_3, while still maintain a hexagonal surface structure. On the other hand Bi_2Se_3 has also been successfully grown on substrates that have completely different surface structure to that of Bi_2Se_3. One of the most extreme examples is growth of Bi_2Se_3 films on amorphous SiO_2 substrate (Bansal et al., 2014), which does not provide any crystalline template for growth. Even in such substrates reasonably good quality Bi_2Se_3 films have been achieved. The question of how such structural mismatch between substrates and the film affect defect formation and electrical properties of Bi_2Se_3 thin films is the central work of this thesis and we will discuss it in detail in Chapter 3. Here, we will give a simple outline of growth of Bi_2Se_3 on Al_2O_3, which captures the essence of growth requirement for Bi_2Se_3 growth on all other substrates.

Growth of Bi_2Se_3 and protective capping [2]

Polished single crystal Al_2O_3(0001) substrates with dimension of 10 mm x 10 mm x5 mm (L x W x H) were purchase from commercial vendors. Such polished surfaces are atomically flat with average surface roughness less than 3 Å, which is crucial for epitaxial growth of thin films. The (0001) of the substrate indicates that the substrate has a hexagonal symmetry and the surface normal is the c-axis direction. Therefore, the surface of Al_2O_3(0001) and Bi_2Se_3(0001) share the same crystal symmetry. The substrates were checked under optical microscope to check for extended defects or impurities on the surface. This was followed by cleaning the substrate by exposing it to a UV generated ozone, which removes organic contaminants from the substrate. After that the substrate was loaded into the growth

[2] **Similar but slightly different growth parameters were used in (Bansal et al., 2012).**

chamber. Inside the growth chamber, the substrate was heated to 750 ^{o}C in an oxygen environment of 10^{-6} Torr. This oxygen environment further helps to clean the organic contaminant on the substrate surface by facilitating formation of CO_2, which can be pumped away. For other substrates, these steps are slightly different in terms of cleaning temperature or introduction of oxygen into the chamber, but the general idea of heating substrates to remove the adsorbates and contaminants still holds. After 10 minutes at 750 ^{o}C, the substrate was cooled down to 135 ^{o}C. Meanwhile, Bi and Se sources are heated to ∼570 ^{o}C and ∼175 ^{o}C. At these temperatures the usual fluxes of Bi and Se are ∼ 2 x 10^{13}/cm^{2}s and ∼ 25 x 10^{13}/cm^{2}s respectively. After allowing the sources to thermally stabilize for about half an hour, we are ready to deposit the film.

Here we would like to digress a little and explain the growth mechanism of Bi_2Se_3. Se has a very high vapor pressure and has a sticking coefficient of ∼0 on Al_2O_3 surface at temperatures above ∼100 ^{o}C. Sticking coefficient is the ratio of atoms that get adsorbed to the substrate to the ratio of impinging atoms. Similarly, Bi sticking coefficient is 0 for temperatures above ∼200 ^{o}C. Therefore, individually neither Bi nor Se would stick to Al_2O_3 at temperatures above ∼200 ^{0}C. However, when codeposited, Bi_2Se_3 will grow even at the elevated temperatures. Furthermore, just like with Al_2O_3, Se does not stick to Bi_2Se_3 at temperatures above ∼100 ^{o}C, which means that above this temperature, growth rate of Bi_2Se_3 is always determined by Bi flux. This situation is similar to that of GaAs, where the growth rate is determined solely by Ga flux. The stoichiometric ratio of 2:3 in Bi_2Se_3 suggests that for Bi flux of ∼ 2 x 10^{13}/cm^{2}s only ∼ 3 x 10^{13}/cm^{2}s Se flux is necessary. On the other hand Se flux used in growth is usually 10 times higher than Bi flux. This has two fold reason: 1) the dominant native defects in Bi_2Se_3 are Se vacancy and using high Se flux could mitigate such vacancy formation and 2) such high flux does not adversely affect the growth in any other way.

Having briefly explained growth dynamics of Bi_2Se_3, we now follow on with growth of Bi_2Se_3 on Al_2O_3. Figure 2.14a shows the RHEED pattern of the cleaned substrate. Prior to growth of the film, the shutter protecting the substrate is opened. This is followed by co-deposition of Bi and Se. In practice this is achieved in MBE by simultaneously opening the shutters at the top of each elemental cell. Using growth rates calculated from previously

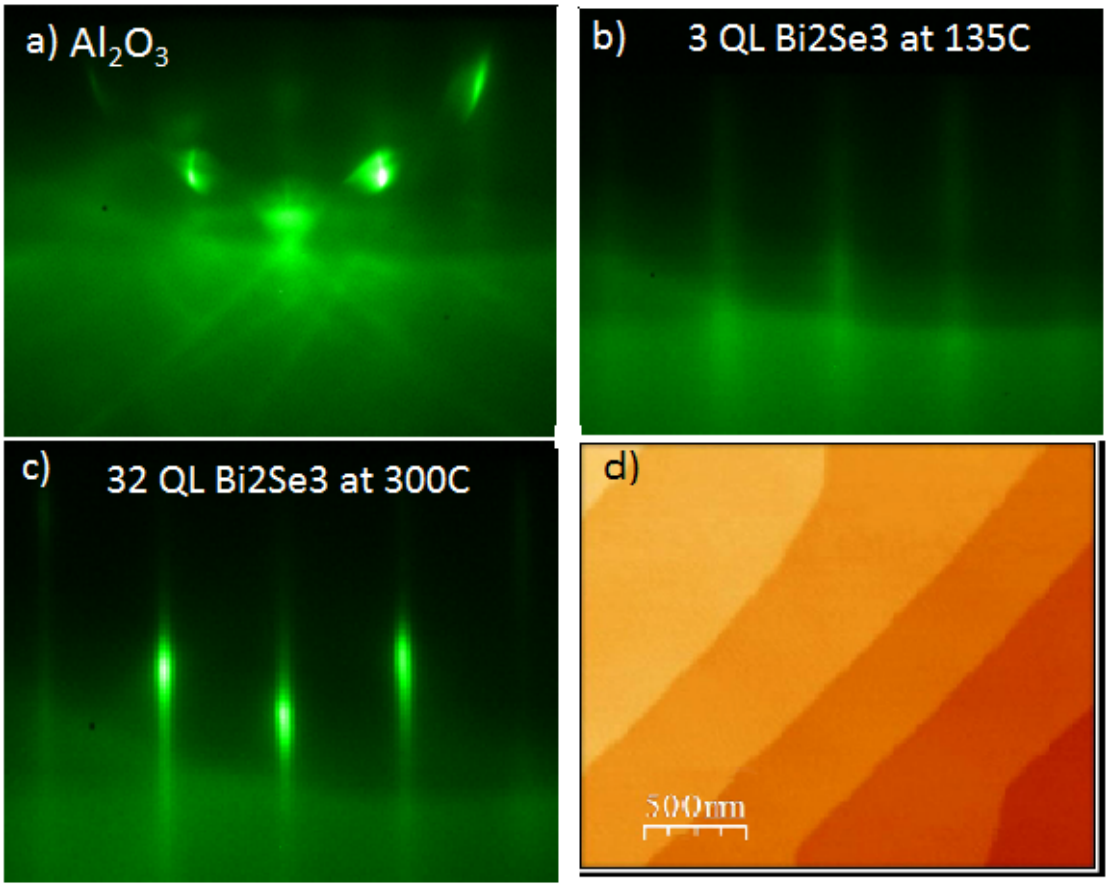

Figure 2.14: **Evolution of film quality during growth:** RHEED pattern of (a) bare Al_2O_3 substrate, (b) 3 QL Bi_2Se_3 at 135 ^{0}C and (c) 32 QL Bi_2Se_3 at 300 ^{0}C, (d) AFM image of a typical Bi_2Se_3 film grown on Al_2O_3 (Courtesy: Eliav Edrey).

obtained flux values from QCM and/or RBS measurement, the shutters are opened so that 3 QL of Bi_2Se_3 is grown at 135 ^{o}C. Apart from the growth shutter, every other shutter is controlled using LABVIEW programs in order to minimize the human error factor. Once the 3 QL Bi_2Se_3 growth is completed, the computer closes Bi shutter to stop further growth. However, it should be noted that Se shutter is kept open at all times during the growth due to reasons discussed in preceding paragraph. The RHEED pattern after 3 QL growth is shown in Fig. 2.14b. As expected, the RHEED pattern gets more diffuse compared to that of the substrate due to poorer crystallinity. However, the film is still 2D in nature.

After the deposition of 3 QL film at 135 ^{o}C, the substrate temperature is slowly increased to 300 ^{o}C. After 10 minutes of annealing at 300 ^{o}C, RHEED pattern improves considerably.

This is because at this elevated temperature, the atoms on the film surface can get rearranged due to extra energy, which leads to improved crystallinity. At this point further film deposition can be done by simply opening the Bi shutter for desired amount of time. Figure 2.14c shows RHEED from a 32 QL growth of Bi_2Se_3, which clearly shows superior RHEED streaks consistent with atomically smooth terraces and absence of 3D islands. Figure 2.14d shows an AFM image showing large smooth terraces of Bi_2Se_3 consistent with observation from RHEED. After film growth, the substrate temperature is lowered towards room temperature, while Bi cell is cooled down to its idle temperature of 300 ^{0}C. At substrate temperature of 135^{0}C, the growth shutter and Se shutter are closed in order to prevent Se sticking to the film surface. Se cell temperature is lowered to room temperature.

When growth temperature falls below 80 ^{0}C, the sample can be transferred to the prep chamber, taken out and measured. Alternatively,the sample can be allowed to cool down to lower temperatures, where it can be capped by a protective capping layer.

The necessity for capping a Bi_2Se_3 film could arise due to several reasons. If the films are grown for the purpose of *ex situ* ARPES or STM characterization, then pristine surface are required. Any exposure to atmospheric contaminants renders them useless for such measurements. Secondly, the electrical properties of Bi_2Se_3 are highly sensitive to atmosphere and deteriorate fairly quickly on the order of minutes to hours. Capping layers help to preserve the film quality over long atmospheric exposure times. The most common capping material for Bi_2Se_3 is Se, however MoO_3 capping has also been used (Edmonds et al., 2014) on films grown for electrical measurements. $\sim$100 nm of Se or $\sim$50 nm MoO_3/ 50 nm Se capping seem to be very effective against environmental degradation. Se is the preferred capping material for aforementioned ARPES and STM measurements due to its property to sublimate at low temperatures.Se capped samples are transported from MBE chamber to ARPES or STM chamber, which also operate under UHV conditions. Inside the prep chamber of those facilities, Se capping can be completely desorbed when the samples are heated to $\sim$ 200^{0}C revealing pristine sample surfaces. Having discussed the growth and structural characterization of the films, we now discuss electrical measurement techniques used to characterize electrical properties of the film such as carrier densities and carrier mobilities.

2.2 Electrical transport

In the previous section we discussed the growth and structural characterization of thin films. Ultimately, however, as physicists we seek to understand the novel physical phenomena associate with these films. As discussed in the introductory chapter, the TSSs are the most interesting manifestation of the non-trivial topology of TIs and detecting the transport signature of these TSSs has been a major focus of the TI community. While we will defer our results from such measurements to next two chapters, here we will outline the method of electrical measurements used in our lab.

2.2.1 Drude model

The basic idea of measurements in physics resides in perturbing the system and measuring its response. In electrical transport, electric field acts as the perturbation and the response of the system could include flow of charge, which is captured by the idea of measuring electrical conductivity (although resistivity or resistance is the directly measured quantity in experiments). At the beginning of 20th century, Drude proposed a model to explain such phenomena in solids. We begin by emphasizing that Drude model is a purely classical theory and therefore does not capture the quantum nature of solids at all. However, by incorporating some of the results from quantum mechanics into Drude model, this simple picture can still account for a variety of transport phenomena. In fact, majority of our transport data can be analyzed within the framework of modified Drude model and this is what we will expound on in the following.

In response to an applied electric field, charges flow in conductors creating current. If an external electric field $\vec{E}$ is applied to an electron in a solid, then the force $\vec{F}$ on the free electron is given by

$$\vec{F} = \frac{d\vec{p}}{dt} = e\vec{E} \tag{2.1}$$

where, $\vec{p}$, t and e are momentum, time and electronic charge respectively. This formula suggests that the electron will keep on accelerating and velocity will linearly increase in time. This obviously does not happen in a material. When an electric field ($\vec{E}$) is applied to a material, the current through the material (which is proprotional to the electron drift velocity)

will increase initially for some time but will reach a steady state quite quickly. The increase in temperature of the material indicates that the electron dissipates excess energy into the system. We now know that these dissipative processes are caused by scattering/collison of electrons from impurity potentials and phonons.

Clearly, (2.1) needs to be modified in presence of such dissipative scenario. We will now include the effect of such collisions. Lets say that at time t, the momentum of an electron is $\vec{p}(t)$. In a given infinitesimal time interval dt, the momentum is $\vec{p}(t+dt)$. If there is collison during this time then on average $\vec{p}(t+dt) = 0$, otherwise its $\vec{p}(t) + e\vec{E}dt$. However, there is a probability associated with having such a collision in time interval dt. Let us assume this probability to be dt/τ. Then the change in momentum over this infinitesimal time is $\vec{p}(t+dt) = (1 - dt/\tau)(\vec{p}(t) + e\vec{E}dt)$. Rearranging, it can be written as $\frac{d\vec{p}}{dt} = -\frac{\vec{p}}{\tau} + e\vec{E}$. In steady state, the left hand side is zero and the equation becomes $p = e\tau E$. Since $p = mv$ and taking into all the n number of electrons going through the unit area of the system into account, we find $nev = ne^2\tau E/m$. The left hand side is by definition current density j and we end up the familiar equation:

$$j = \frac{ne^2\tau}{m}E \equiv \sigma E \tag{2.2}$$

where we identify the prefactor as electrical conductivity. We further write the $\sigma = \frac{ne^2\tau}{m} \equiv ne\mu$, where μ is the mobility of the charge carriers and τ is called the relaxation time. In experiments, σ and n can be directly measured and therefore mobility can be extracted. Up until now m that entered into (2.2) has been taken to be the free electron mass. However, we know that in crystals the effect of periodic crystal potential renormalizes the mass of the electrons into what is known as effective mass m^*. This mass can be orders of magnitude different than the bare electron mass in many materials. Replacing the bare electron mass by the effective mass in (2.2) makes Drude model suitable for analysis of many transport properties.

2.2.2 Hall Effect: Carrier density

In the presence of electric field and magnetic field, electrons experience Lorentz force $F_{Lorentz} = eE - evB$. The response of the carriers in a solid to transverse electric and

magnetic fields can be used to find the carrier density of a material. This was first demonstrated by Edwin Hall and the name bears his name: Hall effect. As shown in Fig. 2.15,

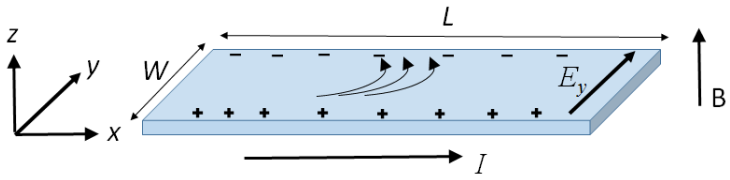

Figure 2.15: **Hall Effect:** Lorentz force due to mutually perpendicular current I and magnetic field B deflect charges creating Hall electric field (E_y), which can be measured to extract carrier density of the sample

if the current (I) runs along x direction and magnetic field along z direction, the Lorentz force creates a drift of electrons toward the $+y$ direction. As more electrons move towards $+y$, this imbalance between charges create an electric field E_y, which counters the Lorentz force. At steady state then, $eE_y = evB$. Since the voltage drop across y-direction (V_{Hall}) is just WE_y, where W (L, H) is the width (length, height) of the sample. We can now compute Hall resistance as $R_{Hall} = V_{Hall}/I$. Furthermore I can be written in terms of current density as $I = jWH = nevWH$. We can now substitue these into the expression for R_{Hall} to get $R_{Hall} = B/ne$, where n is the areal carrier density of the sample. This is the method that we employ to extract carrier density in our samples. We mention that at extremely high magnetic fields, when the effect of quantized cyclotron orbits (in other words Landau levels) become dominant, this semiclassical bheavior becomes inadequate. This is for example the case in QHI discussed in Chapter 3, where R_{Hall} spectacularly deviates from linear B field dependence.

2.2.3 Experimental set up

Sample Preparation and low temperature measurement systems

Once the sample is taken out of the MBE chamber, it is immediately transported to another room for electrical measurement. The sample is attached to the sample holder as shown in Fig. 2.16. We use double sided copper tape to make such attachments, since apart from adhesion they also provide proper thermal conduction between the sample holder and the

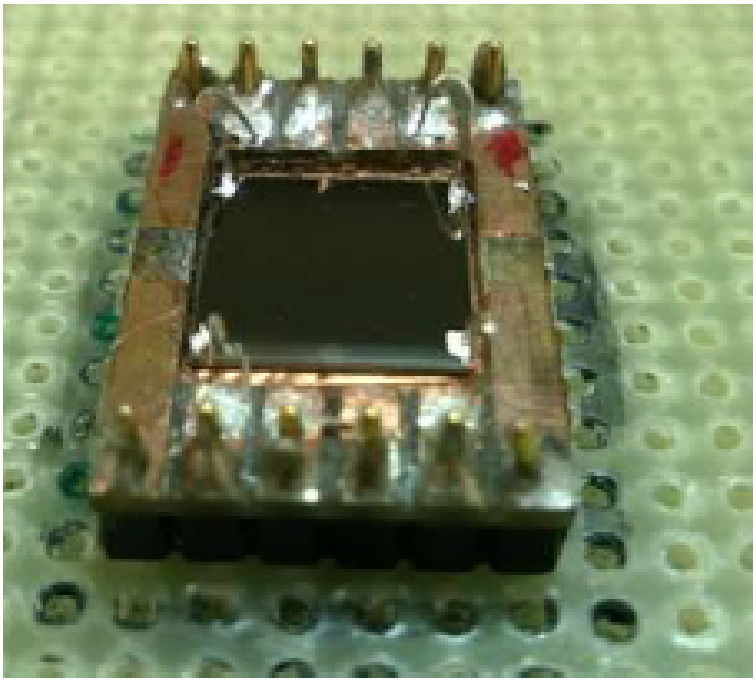

Figure 2.16: **Electrical connection of films to sample holder:** A Bi_2Se_3 film electrically connected to sample holder with In wire in Van der Pauw geometry

sample. Once the sample is attached to the holder, pressed indium wires are used to make electrical contacts from the sample to the holder. The holder has a 8-pin DIP type connector, which gets connected to electrical wires whose other ends are connected to source-meter such as Keithley 2400 for resistance measurement. In our lab, we routinely perform low temperature magnetoresistance and Hall resistance measurement of our samples. We have two systems with different capabilites of base temperature and magnetic field. The first is a cryogen free closed-cycle displex system from Advanced Research System (ARS), which can reach base temperature of ∼5 K. The system includes electromagnets from GMW, which can produce upto 0.6 T magnetic field. Being a cryogen-free system, it is cheaper to run and is used almost everyday. The second is a liquid He4 cryostat from Amreican magnetics Inc., which has a base temperature of ∼ 1.5 K. The system also has a superconducting magnet, which can produce up 9 T. At the center of the bore is the sample space, so the sample experiences a very uniform magnetic field. Since it requires liquid He4 to cool the magent and the sample, this system is more expensive to operate than the ARS system. In either system electrical measurements and magnetic field are both controlled by custom

built LABVIEW programs.

Measurement Geometry

In measurement of the electrical properties of the films, we either use Hall bar geometry or a Van der Pauw (VdP) geometry, both of which are schematically shown in Fig. 2.17. Both these measurements employ four-point measurement system, which simply means that separate pair of electrical leads are used to source current and measure voltage. The advantage of four point measurement is it avoids measurement of contact resistances and lead resistances, which are unavoidable with two point measurements. Our goal is to measure longitudinal sheet resitance (R_{sheet}) and Hall resistance (R_{Hall}) of a given sample. From these measured quantities, sheet carrier density and mobility of the films can be extracted. First lets dicuss the VdP geometry. Here the leads are placed on four corners of the sample.

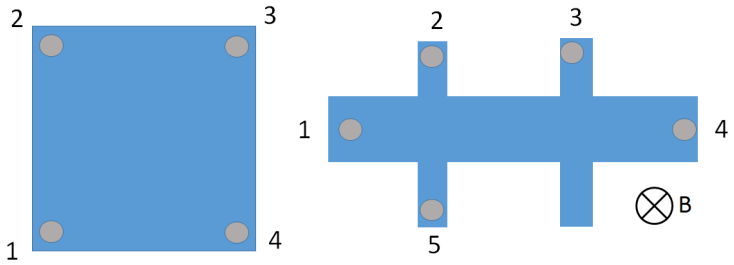

Figure 2.17: **Electrical measurement Geometries:** Van der Pauw geometry (left panel) and Hall bar geometry(right panel) The circles represent measurement leads and the magnetic field is applied into the plane or the paper

For longitudinal resistance along x-direction, we run current through leads 1 to 2 and measure voltage across leads 4 and 3. We write the measured resistance as $R_{12,43} = V_{43}/I_{12}$. Similarly longitudinal resistance along y-axis is measured as $R_{14,23}$. For Hall resistance, we measure $R_{13,42}$. L.J. van der Pauw (van der Pauw, 1958) showed that these values must be related by:

$$e^{\frac{-\pi R_{12,34}}{R_{sheet}}} + e^{\frac{-\pi R_{14,23}}{R_{sheet}}} = 1 \tag{2.3}$$

In (2.3), if we replace $R_{14,23}$ and $R_{12,43}$ with their average, which we call R_{long}, then we immediately get:

$$R_{sheet} = \frac{\pi}{ln(2)} R_{long}$$

There are a series of assumptions van der Pauw made in order to get (2.3). These include isotropic and homogeneous samples, uniform thickness, large sample size compared to areas of the leads and absence of holes in the system. In almost all of our films these requirements are approximately met. Using R_{sheet} and R_{Hall}, sheet carrier density and mobility can be easily extracted.

In the Hall bar geometry, longitudinal resistance is measured as $R_{14,23}$ and Hall resistance is measured as $R_{14,52}$. Given the length (L) and width (W) of the Hall bar, $R_{sheet} = R_{14,23} \times W/L$ and again the sheet carrier density and mobility can be extracted.

We now discuss some of the advantages and disadvantages of each of these geometry. VdP geometry can be set up easily and quickly. This is particularly important when measuring uncapped TI films, where we want to minimize the ambient exposure of the film. By comparing capped samples in either measruement geometry, we have found that values obtained from VdP stay within few percent of those obtained from Hall bar geometry. Such a small cost in accuracy is acceptable given the enormous benefit of this measurement technique. On the other hand, Hall bar allows for a more clinical measurement of resistances as the measurement leads are well defined and well outside of the active measurement area of the sample. This leads to significantly less mixing of lognitudinal and Hall resistances compared to VdP geometry. However the time and fabrication process involved in making samll Hall bars can lead to severe degradation of Bi_2Te_3 thin films.

Solution to resistance mixing

Discussion in preceding section assumed that the measurement leads in either geometry were perfectly aligned. In reality, especially in VdP set up, the leads are misaligned from their *ideal* positions. Such misalignment of leads brings about mixing of the longitudinal and Hall resistance. In other words, experimentally measured longitudinal resistance $R_{long,exp}$ will pick up small portion of the Hall resistance and *vice versa*. While careful alignment of leads can alleviate this problem to some extent, it is impossible to get rid of them due to the fact that leads are placed manually onto the films and the error in alignment can not be eradicated. On the other hand, the properties of longitudinal and Hall resistances can be used to remove the mixing. Rather than presenting the details of data analysis, we give

the physical reason as to why such mixing can be removed simply with post measurement data analysis. The key idea is that the R_{sheet} is an even function of magnetic field, while $R_{Hall} \propto B$ is clearly an odd function of magnetic field. Then the raw experimental data can be (anti)symmetrized with respect of magnetic field, B, to get the actual resistance values using following equations:

$$R_{long,unmixed}(B) = \frac{R_{long,exp}(B) + R_{long,exp}(-B)}{2}$$

$$R_{Hall,unmixed}(B) = \frac{R_{Hall,exp}(B) - R_{Hall,exp}(-B)}{2}$$

2.3 Coclusion

Growth, structural characterization and electrical characterization of Bi_2Se_3 thin films constitute the primary experimental work relevant to this dissertation. Having explained each of these procedures in some detail in this chapter, we will discuss relevant experimental results obtained by using these techniques in the next chapter.

Chapter 3

Epitaxial engineering of high quality Bi_2Se_3 films

Sections 2 and 3 of this chapter are reprinted (with minor changes) with permission from (Koirala et al., 2015)

3.1 Electrical properties of Bi_2Se_3[1]

TIs should have insulating bulk and metallic TSSs. However in reality, Bi_2Se_3, Bi_2Te_3, Sb_2Te_3 all have quite conducting bulk and low TSS carrier mobility. Both of these things are undesirable and one of the central efforts in the field of TIs has been to minimize the bulk conduction while simultaneously enhancing TSS conduction. In this chapter, we will discuss how we have achieved extremely high quality Bi_2Se_3 film, which has low carrier density, minimal bulk conduction and highest reported TSS carrier mobility. The key to achieving such results lies in understanding how defects affect the electrical properties of the films. On the growth side, this corresponds to growing Bi_2Se_3 thin films on chemically and structurally matched artificial buffer layers, which is where the full force of MBE can be brought to action.

3.1.1 Why bulk is conducting in Bi_2Se_3: Mott criteria

All real material have some level of defects and disorder in them. In Bi_2Se_3 the dominant defects are thought to be Se vacancies, which happen when a Se atom is absent from its usual lattice position. Some amount of such defects are naturally favored by the thermodynamics of the material, but they can also be created due to extrinsic effects. For example, such defects can be created at the interface between Bi_2Se_3 and the substrates during film growth

[1] **Parts of this section is adapted from (Brahlek et al., 2015)**

or they can be created due to environmental exposure. In the following, to streamline our discussion, we will assume Se vacancy to be the dominant defect.

When a Se atom leaves Bi_2Se_3 host lattice, it leaves behind Se vacancy and two electrons.

$$Se \longleftrightarrow Se^{2+}_{Vac} + 2e^{-}$$

Consider such a vacancy in Bi_2Se_3, which can be considered as an individual atom with atomic -like bound states. However, since these atoms are embedded in Bi_2Se_3 rather than in vacuum, the Coulomb potential gets rescaled, which leads to rescaled atomic orbitals with effective Bohr radius $a_B = \epsilon\frac{m}{m^*}a_H$, where ϵ, m, m^* and a_H are dielectric constant of Bi_2Se_3, bare electronic mass, effective mass of bulk electrons in Bi_2Se_3 and free space Bohr radius respectively. For Bi_2Se_3, where $\epsilon \sim$ 50-110 and $m^* \approx 0.15\ m$, this gives $a_B \approx$ 15 - 30 nm. Physically, this corresponds to size of the Se vacancy in Bi_2Se_3. As the number of vacancies increase, the atomic-like orbitals begin to overlap and the electrons bound to vacancies become mobile. The bulk of Bi_2Se_3 thus becomes metallic. This qualitative argument was put into quantitative foothold by Sir Neville Mott in 1960s by a simple criteria $a_B N_C^{1/3} = 0.26$, which states that above the critical vacancy density N_C, bulk of Bi_2Se_3 becomes conducting. This gives $N_C \sim 10^{14}\ cm^{-3}$, which is a rather small value compared to semiconductors like Si and GaAs ($N_C \sim 10^{18} cm^{-3}$). The important point is that the lowest defect density achieved in Bi_2Se_3 bulk crystals is $\sim 10^{16}\ cm^{-3}$ (Butch et al., 2010) and therefore the bulk must be conducting according to the Mott criteria. These crystals were indeed conducting in the bulk (Butch et al., 2010). Given that the lowest defect densities achieved in experiments are two order of magnitude higher than N_C, this suggests that at least deep in the bulk of the material, E_F lies near the bottom of the bulk conduction band.

3.1.2 Ineterfacial versus bulk defects: Band bending

If E_F at the surface ($E_{F,Surface}$) of Bi_2Se_3 is different than at the bulk ($E_{F,Bulk}$), then the charges flow until E_F is equilibrated everywhere. This creates a spatial imbalance of charge near the surface of Bi_2Se_3 resulting in an electric potential in the region, which bend the bulk bands in the vicinity of the surface. If initially $E_{F,Surface} < E_{F,Bulk}$, then some electrons flow from nearby bulk towards the surface until equilibrium is achieved. If

we consider the total charge (electrons as well as the ions), then the surface now has net negative charge, while nearby bulk region has net positive charge. This creates additional electric potential energy in this region that decreases from the surface to the nearby bulk, where it eventually goes to zero. Now the electronic states in this area (i.e. the energy bands) are shifted by this additional new potential energy, which gives rise to energy bands bending in this region. In this case the bands bend upward near the surface, and this region is called a depletion region. If the initial scenario was reversed i.e. $E_{F,Surface} > E_{F,Bulk}$, then by similar arguments, the bulk bands bend downward and the region is called an accumulation region. On the other hand if $E_{F,Surface} = E_{F,Bulk}$ then no band bending occurs and this scenario is called the flat band scenario.

We can estimate the sheet carrier density that corresponds to the flat band scenario. Due to spin polarized 2D nature of the TSSs, energy of TSSs carriers (E_{TSS}) is related to the surface carrier density (n_{TSS}) as:

$$E_{TSS} = \hbar v_F \sqrt{4\pi n_{TSS}} \tag{3.1}$$

Next, assume that $E_{F,Bulk}$ is pinned at the bottom of the bulk conduction band. In Bi_2Se_3 bottom of the bulk conduction band lies $\approx$ 200 meV above the Dirac point and the Fermi velocity (v_F) of the TSSs is $\approx 4\times10^5$ m/s (See (Brahlek et al., 2015) and references therein). Then, using Eq. (3.1) we can see that for E_{TSS} to be level with the bottom of the bulk conduction band, n_{TSS} must be $\approx 5\times10^{12} cm^{-2}$. Therefore, $E_{F,surface}$ lies at the bottom of conduction band and leads to flat band scenario. For $n_{TSS} > 5\times10^{12} cm^{-2}$, the bands bend downward and *vice versa*. These three scenarios are shown in Fig. 3.1. In experiments, both upward and downward bending of the bulk bands have been observed. There are some important differences between upward and downward band bending scenarios. In the accumulation region where the bulk bands bend downward, the confining potential quantizes the bulk band in this area, which gives rise to non-topological 2DEG states near the surface of the film. Such scenario does not exist in the case of upward band bending for ($n-type$ doped) Bi_2Se_3. This non-topological 2DEG conducts in addition to TSSs and is an undesired consequence of downward band bending.

Another major difference between these two scenarios is that in the upward band bending

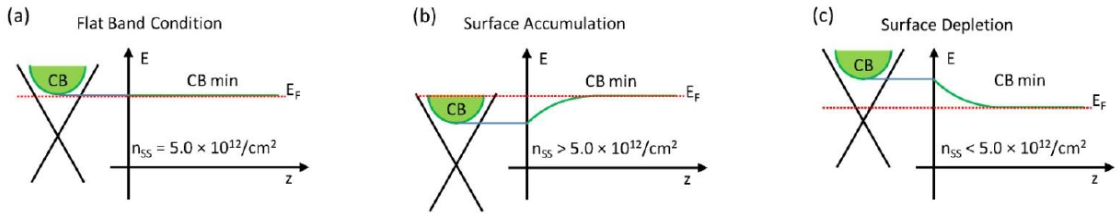

Figure 3.1: **Band bending in Bi_2Se_3:** If $n_{TSS} \approx 5 \times 10^{12}$ cm^{-2}, then (a) the bands remain flat, for higher values (b) bands bend downward and for lower values (c) they bend upward. Figure taken from (Brahlek et al., 2015).

scenario, the Mott criteria which makes the bulk conducting can be circumvented for films thinner than approximately twice the depletion region. In this scenario E_F in the bulk can be made to fall below the bottom of the bulk conduction band and the bulk then becomes insulating. This can be qualitatively understood as follows. Upward band bending is a result of electron transfer from depletion region to the surface; if the film itself is thinner than this region then there are not enough charges left in the bulk to equilibrate the E_F. Therefore only other way to do so is that the E_F in the bulk now must fall below the conduction band bottom resulting in insulating bulk. The factor of 2 is because there are two surfaces to be considered in TI thin films rather than a single one. Using Possion equations and reasonable parameters for Band bending in Bi_2Se_3, Brahlek et. al (Brahlek et al., 2015) have estimated the depletion region to be on the order of 50 - 100 nm. Films thinner than these length scales still preserve their topological properties and can be easily fabricated by MBE thus making this an attractive route towards obtaining bulk insulating thin films. In fact recent experiments on carefully prepared Bi_2Se_3 thin films have indeed shown that bulk is indeed highly insulating and the transport is dominated by TSSs (Brahlek et al., 2014; Koirala et al., 2015). On the other had bulk cannot be made insulating by thinning the films in downward band bending samples.

We now briefly discuss the reason for difference in $E_{F,Surface}$ and $E_{F,Bulk}$ before equilibration. Before equilibration, the E_F is locally set by charged defects. Therefore defects created at the surface determine the $E_{F,Surface}$ and defects in the bulk determine the $E_{F,Bulk}$. Since we want $E_{F,Surface} < E_{F,Bulk}$ for upward band bending and ultimately insulating bulk in the limit, minimizing surface defects becomes an important criteria. Since

thin films are grown on substrates and the interface between them is directly affected by substrates, it is clear that choice of substrates play an important role in interfacial defect formation and therefore the electrical properties of TI thin films.

3.1.3 Electrical Properties of Bi_2Se_3 thin films grown on conventional substrates

As discussed in Chapter 2, due to its layered nature Bi_2Se_3 films can be grown on a variety of substrates. These have included substrates such as $Al_2O_3(0001)$, Si(111), $SrTiO_3(111)$, InP(111) and amorphous-SiO_2 to name a few. To elucidate the connection between substrates, defects and electrical properties of Bi_2Se_3 thin films, we will focus on films grown on $Al_2O_3(0001)$ (Bansal et al., 2012) and Si(111)(Kim et al., 2011) in the following.

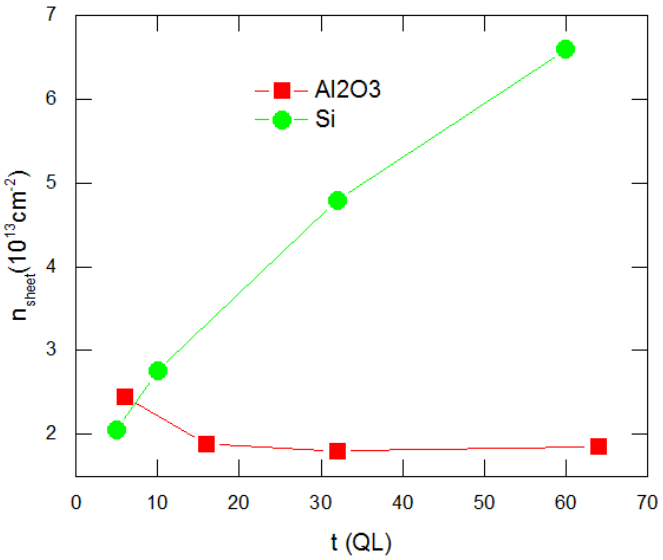

Figure 3.2: **Different dependencies of n_{sheet} on film thickness for films grown on Al_2O_3 and Si:** For Si film, there is a clear thickness dependence indicating both bulk and interfacial defects contribute similarly, while for films grown on Al_2O_3, nearly thickness independent means that interfacial defects are the dominant defects. Data taken from measurements done in Prof. Oh's lab by Namrata Bansal and Y.S. Kim.

Figure 3.2 shows the sheet carrier density (n_{sheet}; where n_{sheet} = volume carrier density x film thickness) as a function of film thickness (t) for both types of films measured at 1.5 K and in magnetic field upto 1 T. For films grown on $Al_2O_3(0001)$, the sheet carrier density

is almost independent of the thickness while those grown on Si(111) show $n_{sheet} \sim t^{1/2}$. This different thickness dependence indicates that in films grown on $Al_2O_3(0001)$ interfacial/surface defects dominate leading to nearly thickness independent behavior of n_{sheet} , while in films grown on Si(111) a combination of both interfacial and bulk defects dominate the electrical properties of the film. This also means that two dimensional transport channels dominate the conduction in the former, while in the latter clearly there are three dimensional bulk channels in addition to any two dimensional transport channels. Furthermore, since the magnitude of $n_{sheet} \sim 2\times\ 10^{13}$ cm^{-2} observed for films grown on $Al_2O_3(0001)$ is greater than $2 \times (5\times\ 10^{12}$ cm$^{-2})$, there is clearly downward band bending in these films (the prefactor 2 is to account for two surfaces of the film). Therefore, based on band bending arguments presented in previous section, non-topological 2DEGs exist in these films and contribute to the transport in addition to TSSs channel. Indeed, such 2DEGs have been reported in experiments done in these films (Bansal et al., 2012).

The different types of dominant defects in films grown on $Al_2O_3(0001)$ and Si(111) are presumably related to the difference in the substrates. $Al_2O_3(0001)$ is inert but has a lattice mismatch of $\sim 14\%$ to Bi_2Se_3, while Si is more reactive but the lattice mismatch is only $\sim -7\%$. It is natural to postulate that a substrate that is both structurally and chemically compatible with Bi_2Se_3 could minimize both interfacial and bulk defects resulting in high quality films with dominant TSSs conduction.

3.2 Bi_2Se_3 on In_2Se_3 based buffer

Commercial substrates are far from being structurally and chemically compatible to Bi_2Se_3, with current selections either increasing bulk defects or creating interfacial defects (Bansal et al., 2012, 2014; Guo et al., 2013; Hellerstedt et al., 2014; Kim et al., 2011). However, by starting with a standard substrate, molecular beam epitaxy (MBE) does allow a virtual-substrate composed of an electrically insulating buffer layer to be engineered on the atomic-scale. Here we show that an isostructural buffer layer consisting of 20 quintuple layers (QL; 1 QL $\sim$ 1 nm) In_2Se_3 followed by 20 QL $(Bi_{0.5}In_{0.5})_2Se_3$ grown on an $Al_2O_3(0001)$ substrate indeed serves as an ideal template for high quality Bi_2Se_3 growth with minimal interfacial and bulk defects.This suppression of material defects has led to low carrier density Bi_2Se_3

films with the highest reported TSS mobility, which culminated in our observation of the quantum Hall effect (QHE).

3.2.1 Growth of Bi_2Se_3 on In_2Se_3 based buffer layer

Bi_2Se_3 and In_2Se_3 share the same crystal structure with covalently bonded QLs, which are held together by weak Van der Waal's force. The inplane lattice constant of In_2Se_3 is 4.05 Å leading to only -3% lattice mismatch with Bi_2Se_3. Unlike Bi_2Se_3, In_2Se_3 is just a band insulator with bandgap of ∼1.3 eV. However, as far as we know, large single crystal substrates of In_2Se_3 are not commercially available. On the other hand In_2Se_3 can be grown pretty much exactly the same way as Bi_2Se_3 using MBE. Furthermore, high quality solid solution $(Bi_{1-x}In_x)_2Se_3$ can also be easily grown on MBE . For $x > 0.25$, it has been shown that this solid solution is also a band insulator (Brahlek et al., 2012). All these attributes make In_2Se_3 an attractive virtual substrate for epitaxy of Bi_2Se_3.

However, a substrate is still required to grow either In_2Se_3 or Bi_2Se_3. From discussions in previous section and Fig. 3.3d, we see that, except for a thin disordered layer, extremely high quality Bi_2Se_3 can be grown on $Al_2O_3(0001)$.Therefore, we decided to grow In_2Se_3 on $Al_2O_3(0001)$ following similar recipe as for Bi_2Se_3 growth. Unlike the case of Bi_2Se_3 growth on $Al_2O_3(0001)$ where well defined single crystalline thin films were obtained, In_2Se_3 grew in a disordered form. A likely explanation for this is that unlike Bi_2Se_3, In_2Se_3 has at least three polymorphic phases (Emziane et al., 2000) and when deposited directly onto the poorly lattice matched $Al_2O_3(0001)$ substrate it grows in a disordered form. Therefore, to grow a high-quality, single-phase In_2Se_3 layer requires an initial seed layer of 3 QL Bi_2Se_3 that is deposited at 135 ^{o}C. After the growth, the sample is heated to 300 ^{o}C. This serves as a template for the deposition of 20 QL thick In_2Se_3 layer. In contrast to In_2Se_3 grown on $Al_2O_3(0001)$, In_2Se_3 grown on top of Bi_2Se_3 is single phase, c-axis oriented and atomically flat. However, at this stage the underlying 3 QL of Bi_2Se_3 remains conducting, which is undesirable for transport studies of the main Bi_2Se_3 layer to be grown later. In order to make it electrically insulating we heat this entire layer up to 600 C where the Bi_2Se_3 seed layer diffuses through the In_2Se_3 and evaporates away, which leaves behind the high quality, insulating In_2Se_3 layer directly on the $Al_2O_3(0001)$ substrate. (This was confirmed

by Rutherford backscattering on a test sample, where 50 QL Bi_2Se_3 - 10 QL In_2Se_3 film only showed 10 QL $Bi_{0.02}In_{0.98})_2Se_3$ after annealing to 600 ^oC.) The sample was then cooled to 275 ^oC for further growth. On top of this a 20-QL thick insulating layer of $Bi_{0.5}In_{0.5})_2Se_3$ is then deposited at 275 C, which acts to suppress In diffusion into the Bi_2Se_3 layer to be grown on top(see next section). This entire structure forms the In_2Se_3 based buffer layer and we refer to it as BIS-BL from here on. On top of this BIS-BL, desired thickness of Bi_2Se_3 is grown for measurement. The growth process is shown schematically in Fig. 3.3a.

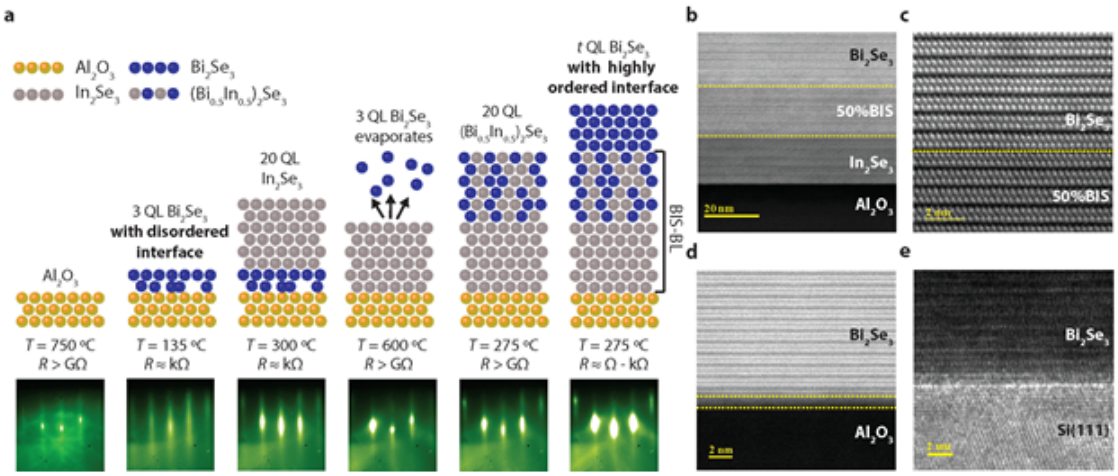

Figure 3.3: **Growth process of Bi_2Se_3 films on the 20 QL In_2Se_3 20 QL $Bi_{0.5}In_{0.5})_2Se_3$ buffer layer (BIS-BL):** (a) Cartoon showing each stage of film growth along with the corresponding growth temperature (T), sheet resistance (R) and RHEED images. HAADF-STEM image of Bi_2Se_3 grown on (b) BIS-BL, which (c) shows an atomically-sharp interface between Bi_2Se_3 and BIS-BL, while (d) Bi_2Se_3 grown directly on $Al_2O_3(0001)$ has clearly disordered interface. (e) TEM image of Bi_2Se_3 grown on Si(111). In (b) and (c), $(Bi_{0.5}In_{0.5})_2Se_3$ is written as 50%BIS. Figure taken from (Koirala et al., 2015)

RHEED images in Fig. 3.3a indicates that the film growth remains two dimensional throughout for the BIS-BL, and results in a flat highly crystalline Bi_2Se_3 layer. Further, Figure 3.3b and 3.3c show high-angle annular dark-field scanning transmission electron microscopy (HAADF-STEM) images of a 50 QL Bi_2Se_3 film indicating highly ordered growth. The most important feature of the films grown on BIS-BL that can be seen in Figure 3.3c, is the sharp, defect-free interface between Bi_2Se_3 and $Bi_{0.5}In_{0.5})_2Se_3$. This is in contrast to Bi_2Se_3 films grown on commonly used substrates such as $Al_2O_3(0001)$ and Si(111), where

the interface is more disordered as indicated by STEM/TEM images shown in Fig. 3.3d and 3.3e, respectively.

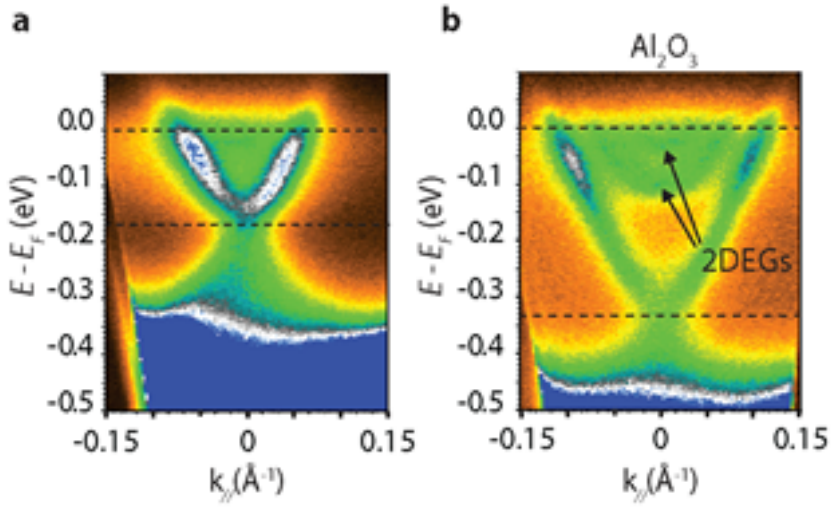

Figure 3.4: **Confirmation of non-trivial topology of Bi_2Se_3 grown on BIS-BL:** ARPES of (a) 30 QL Bi_2Se_3 grown on BIS-BL and (b) 50 QL Bi_2Se_3 grown on Al_2O_3. Both films clearly show TSSs, while film grown on Al_2O_3 also shows 2DEG states formed due to downward bandbending of the bulk bands. Figure taken from (Koirala et al., 2015).

3.2.2 Confirmation of non-trivial topology

We will next show that the Bi_2Se_3 films grown on BIS-BL are still topological insulators. These measurements were partly inspired by the fact that solid solution $Bi_{1-x}In_x)_2Se_3$ goes through a topological phase transition around critical indium concentration $x_c \approx 0.04$ -0.07 (Brahlek et al., 2012; Wu et al., 2013). For $x < x_c$, the solid solution is a topological insulator, while for $x > x_c$ it is a trivial material. If there is significant In diffusion from BIS-BL to Bi_2Se_3, then it could turn into a trivial material.

As a direct evidence of TI nature of the film we performed ARPES measurement on these films [2]. Figure 3.4a shows the ARPES image of a 30 QL thick Bi_2Se_3 grown on BIS-BL. As a comparison we also show ARPES spectra of 50 QL thick Bi_2Se_3 film grown directly on $Al_2O_3(0001)$ in Fig. 3.4b. Both these films clearly show the TSSs, which is definitive

[2] ARPES measurements were performed by Prof. Daniel Dessau's group at University of Colorado

evidence of TI nature of the film. Further, we can compare the position of the surface Fermi levels (E_F) of Bi_2Se_3 grown on both substrates: For the film grown on $Al_2O_3(0001)$, E_F $\sim$ 0.33 eV above the Dirac point. At this level, the conduction band is clearly occupied as 2DEG (two-dimensional electron gas) states that form due to downward band bending of bulk conduction band near the surface. In contrast, for the film grown on BIS-BL, E_F $\sim$0.17 eV above the Dirac point, which implies that on the surface only the TSS bands are occupied. This also means that there is upward band bending in these films, which is a requirement for bulk of TI thin films to be truly insulating.

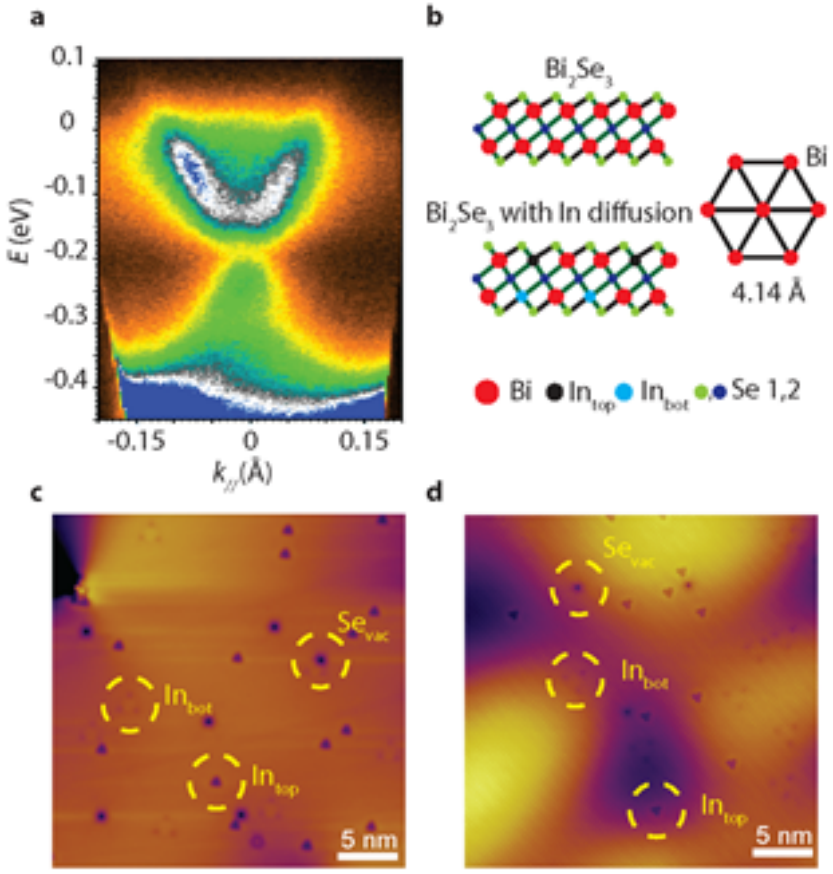

Figure 3.5: **ARPES and STM of Bi_2Se_3 grown on BIS-BL:** (a) ARPES indicating gapped TSS on 5 QL thick Bi_2Se_3. (b) cartoon of a QL of Bi_2Se_3 along with hexagonal arrangement of Bi atoms within a single layer. (c-d) STM topography image showing In_top , In_{bot} and Se_{vac} defects on the topmost QL of (c) 30 QL and (d) 5 QL thick Bi_2Se_3. Figure taken from (Koirala et al., 2015)

We have also measured a 5 QL thick film grown on BIS-BL with ARPES. The TI nature

of Bi_2Se_3 films grown on BIS-BL even in ultrathin regime is shown by observation of gapped TSS for a 5 QL thick Bi_2Se_3 as is indicated by the ARPES image in Fig. 3.5a. Such gapped TSS have been observed in ultra-thin Bi_2Se_3 grown on 6H-SiC(0001) with the gap attributed to hybridization of top and bottom TSS (Zhang et al., 2010). This is direct evidence of non-trivial nature of Bi_2Se_3 grown on top of BIS-BL even in the ultrathin limit. Such an observation means that the In diffusion should be much less than ∼3%, where a signature of the topological phase transition starts to appear. In the following, we give an estimate of such diffusion. Figure 3.5b shows a cartoon of a quintuple layer (QL) of Bi_2Se_3, which consists of alternate layers of Se-Bi-Se-Bi-Se. For Bi_2Se_3 grown on BIS-BL some In diffusion from BIS-BL to Bi_2Se_3 is observed, which is shown schematically in Fig. 3.5b (bottom left image). Diffused In atoms preferentially occupy the Bi sites in the upper and lower Bi layers within a QL and are denoted as In_{top} and In_{bot}, respectively. Figures 3.5c and 3.5d show scanning tunneling microscopy (STM) images[3] of 30 QL and 5 QL Bi_2Se_3 films grown on BIS-BL respectively with three kinds of defects identified Se vacancy (Se_{vac}), In_{top} and In_{bot}. By counting In_{top} and In_{bot} on the surface and calculating the areal number density of Bi (ρ_{Bi}), we can estimate the percentage of In diffusion (In%) in Bi_2Se_3. In order to calculate ρ_{Bi}, we note that Bi atoms are arranged in hexagonal pattern within a monolayer of Bi. A schematic of such a hexagonal unit for Bi layer is shown on Fig. 3.5b. Since the in-plane lattice constant of Bi2Se3 is ∼4.14 Å, the area of the hexagonal unit is $\sim 4.45 \times 10^{-15}$ cm^2. There are 3 Bi atoms in one hexagonal unit,$\rho_{\mathrm{Bi}} \approx 6.74 \times 10^{14}$ cm^{-2}. From the STM image in Fig. 3.5d we can count ∼11 In_{top} and ∼9 In_{bot} in a 30 nm × 30 nm area ($area$). This gives In% = $(In_{top}+In_{bot})/(area \times 2\rho_{\mathrm{Bi}})100\%$ on the topmost QL of Bi_2Se_3 to be ∼0.2% for 5 QL Bi_2Se_3, where 2 in the denominator accounts for two Bi layers within a QL. Similar calculations for a 30 QL thick film also give ∼0.2% In diffusion. Together, ARPES and STM conclusively show that Bi_2Se_3 grown on BIS-BL is a topological insulator.

3.2.3 Electrical transport measurement

Transport measurements are the most sensitive probe to study the presence of defects that supply carriers and cause defect induced scattering. Therefore, to compare the defect

[3]STM measurements were performed by Jixia Dai and Prof. Weida Wu at Rutgers University

density in Bi_2Se_3 grown on the BIS-BL to films grown on $Al_2O_3(0001)$ (from (Bansal et al., 2012)) and Si(111) substrates (from (Kim et al., 2011)) , we show in Fig. 3.6 the sheet carrier density (n_{sheet}) and mobility (μ), respectively, extracted from the low magnetic field Hall measurement ($|B| \leq 0.5$ T) at T = 1.5 K as a function of thickness (t).

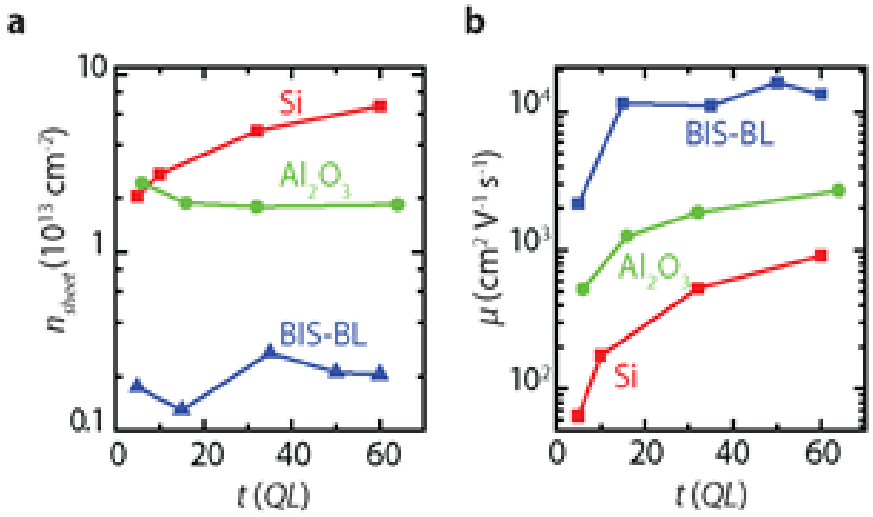

Figure 3.6: **Superior electrical properties of Bi_2Se_3 grown on BIS-Bl compared to those grown on $Al_2O_3(0001)$ and Si(111):** (a) sheet carrier densities and (b) Hall mobilities of Bi_2Se_3 films grown on BIS-BL, $Al_2O_3(0001)$ and Si(111) for various film thicknesses clearly an order of magnitude improvement in each quantity for films grown on BIS-BL. Figure taken from (Koirala et al., 2015)

As shown in Fig. 3.6b, the highest mobility for Bi_2Se_3 grown on BIS-BL exceeds 16,000 $cm^2V^{-1}s^{-1}$, which is about an order of magnitude larger than the mobility of films grown on $Al_2O_3(0001)$ and Si(111) and this directly shows that BIS-BL significantly suppresses net defect density. For the entire thickness range of 5 to 60 QL Bi_2Se_3 grown on BIS-BL, n_{sheet} $\sim$ 3 - 5 $\times$ 10^{12} cm^{-2}, whereas films grown on $Al_2O_3(0001)$ and Si(111) exhibit an order of magnitude larger values of n_{sheet}, similarly implying significantly larger defect densities. Further, the thickness independence for films grown on BIS-BL and $Al_2O_3(0001)$ show that the dominant defects come from the interface, whereas films grown on Si(111) have significant thickness dependence ($n_{sheet} \sim t^{1/2}$) implying a combination of both interfacial and bulk defects (Kim et al., 2011). Lastly, like films grown on $Al_2O_3(0001)$, some non-linearity in the Hall effect was observed at higher field in films on BIS-BL, indicating multiple conduction channels. However, non-linear Hall fitting can be used to estimate the

total carrier density, which is found to be $\leq 5 \times 10^{12}$ cm^{-2} over the entire thickness range for BIS-BL, and $\sim 40 \times 10^{12}$ cm^{-2} for films grown on Al_2O_3 (which we will discuss below). By simultaneously suppressing both interfacial and bulk defects with this BIS-BL, this is the first time such a large improvement in both n_{sheet} and μ has been observed in any TI films.

As mentioned above, the non-linearity in the Hall Effect was observed at fields higher than ~0.5 T for all films, which usually indicates multiple conduction channels with different mobilities. Figure 3.7a shows Hall effect for 5, 25 and 60 QL thick films up to a magnetic field of 9 T. Except for the 5 QL thick film, which shows a weak non-linearity, all the other films show pronounced non-linearity similar to 25 and 60 QL thick films. For the non-linear Hall effect, the sheet carrier density calculated from low field Hall slope gives a mobility-weighted-average of different carrier species rather than carrier density of any single species. In order to specify the sheet carrier density and mobility of individual species we have used the two-carrier model to fit the Hall Effect data

$$R_{Hall}(B) = \frac{-B}{e} \frac{(n_1\mu_1^2 + n_2\mu_2^2) + B^2\mu_1^2\mu_2^2(n_1 + n_2)}{(n_1\mu_1 + n_2\mu_2)^2 + B^2\mu_1^2\mu_2^2(n_1 + n_2)^2} \tag{3.2}$$

where $R_{Hall}(B)$ is the Hall resistance, B is the applied magnetic field, e is the electronic charge and n_i and μ_i are the sheet carrier density and mobility, respectively, of i^{th} species with i = 1, 2. n_i and μ_i are the fitting parameters. Experimentally, there are only two independent parameters: we have fixed $R_{Hall}(B)$/B to the low field slope of the Hall effect, where locally $R_{Hall}(B)$ was linear. We have also used the zero field sheet resistance (R_{sheet}) = $1/[e(n_1\mu_1 + n_2\mu_2)]$ to provide an additional constraint to the fitting. This reduces the number of independent fitting parameters to just two. The model fits very well to the data as is shown in inset of Fig. 3.7a for a 25 QL thick film. Figure 3.7 also shows the sheet carrier densities (n_1 and n_2) obtained from the fit along with the sheet carrier density (n_{LOW}) obtained from the low field Hall effect for comparison. n_1 clearly shows negligible thickness dependence as is the case for n_{LOW}. n_2 shows sample-to-sample variation but is essentially within ~2 - 4 $\times 10^{12}$ cm^{-2}for films thicker than 15 QL with no clear thickness dependence within the thickness range of measured samples. In Fig. 3.7c, we show corresponding mobilities μ_1 and μ_2 for the two channels along with the low field mobility (μ_{LOW}) for

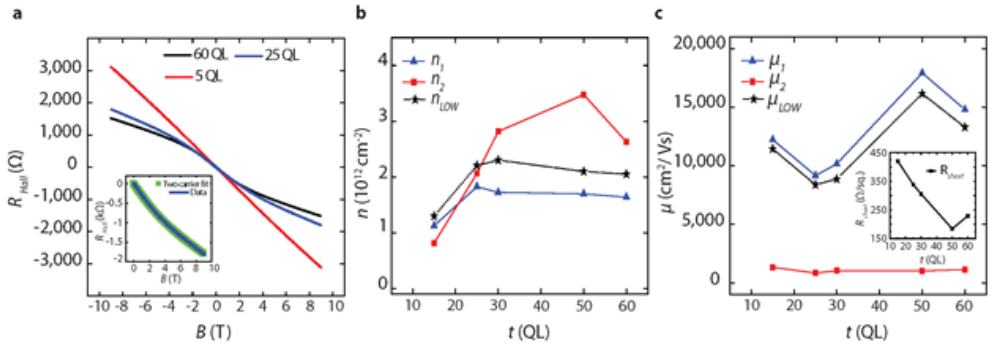

Figure 3.7: **Two carrier model fitting to nonlinear Hall effect:** (a) Non-linear Hall effect in 5, 25 and 50 QL thick Bi_2Se_3; inset shows two carrier fit to the Hall effect for 25 QL thick sample. (b) Sheet carrier density and (c) mobility obtained from two-carrier fit as a function of film thickness, for comparison low field Hall effect data are also shown; the inset shows the zero field sheet resistance as a function of film thickness. Figure taken from (Koirala et al., 2015)

comparison.μ_1 is comparable but consistently higher than μ_{LOW} as is expected since μ_{LOW} gives the weighted mobility of both channels rather than that of the high mobility channel alone. The fact that n_{LOW} (μ_{LOW}) is very close to n_1 (μ_1) suggests that the conduction is dominated by this high mobility channel. According to the detailed discussion given in next section, the high mobility channel is likely to be the TSS at the top surface and the lower mobility channel is that at the bottom surface.

3.2.4 Consistency of transport data with TSS conduction

From Hall measurement, it is clear that low field sheet carrier density (n_{LOW}) is less than $\sim 2 \times 10^{12}$ cm^{-2} in the entire thickness range. Two-carrier fitting from the Hall effect measurement gives a total sheet carrier density ($n_{tot} = n_1 + n_2$) to be at most $\sim 5 \times 10^{12}$ cm^{-2}. In Bi_2Se_3, when the total sheet carrier density is $\sim 1 \times 10^{13}$ cm^{-2} (or equivalently $\sim 5 \times 10^{12}$ cm^{-2} per surface) the surface Fermi energy lies at the bottom of the bulk conduction band (Bianchi et al., 2010; Brahlek et al., 2014). Given that the total carrier density $n_1 + n_2$, is much smaller than $\sim 1 \times 10^{13}$ cm^{-2}for films grown on BIS-BL, they should have, if anything, upward band bending resulting in formation of a depletion region. Such upward band bending cannot form quantum well states or 2DEG (Bianchi et al., 2010; Brahlek et al., 2015). Therefore, the most consistent interpretation of the observed channels

with thickness independent sheet carrier density is that both of them originate from the TSS. This is also supported by ARPES data, where the surface E_F lies in the bulk band gap and no such 2DEGs are observed. In contrast ARPES measurements on Bi_2Se_3 grown directly on Al_2O_3 clearly show presence of such 2DEG states. In order to show the existence of a 2DEG state is unlikely to be present, we can estimate the expected sheet carrier density of TSS if either n1 or n2 originates from 2DEGs. Let us assume that $n_1 \approx 1.8 \times 10^{12}$ cm^{-2} is due to 2DEG carriers. Then we can get the Fermi wave-vector for 2DEG using $k_{F,2DEG}$ $=\sqrt{2\pi n_1}$. This results in $k_{F,2DEG} = 0.034$ $\AA$. Using the ARPES spectrum of Bi_2Se_3 grown on Al_2O_3, we can extrapolate the Fermi wave-vector of corresponding TSS ($k_{F,TSS}$) at this $k_{F,2DEG}$. As shown in FIg. 3.8, such extrapolation yields $k_{F,TSS} \approx 0.088$ $\AA$. From $k_{F,TSS}$ we can get $n_{sheet,TSS} = k^2_{F,TSS}/4\pi \approx \approx 6.1 \times 10^{12}$ cm^{-2} for corresponding TSS, where the 4 in the denominator is due to the non-degenerate nature of TSS. Similar estimation assuming $n_2 \approx 3 \times 10^{12}$ cm^{-2} to come from 2DEG yields $n_{sheet,TSS} \approx 6.8 \times 10^{12}$ cm^{-2}. This gives a combined TSS and 2DEG sheet carrier density of$\sim 7.9 \times 10^{12}$ cm^{-2} ($\sim 9.8 \times 10^{12}$ cm^{-2}) from a single surface assuming n_1 (n_2) originates from 2DEG state. For simplicity if we assume the other surface to have similar carrier density, then the total carrier density would be well above $\sim 10^{13}$ cm^{-2}, which is over three times that of what is observed from Hall effect which rules out the presence of 2DEGs. Therefore, it is most natural to associate the two channels to the TSSs from the top and bottom surfaces, respectively. Naturally, the following question arises: which of the two TSSs is responsible for the higher mobility channel? This can be indirectly answered from the capping layer samples. Considering that the mobilities of the Se and MoO3 capped films are substantially reduced from uncapped samples, it seems that the higher mobility channel originates from the top TSS; if the high mobility channel originated from the bottom TSS, such dramatic reduction would not be expected with capping.

3.2.5 Evidence of TSS conduction from cyclotron resonance

While transport measurement and ARPES are both consistent with TSS conduction, for definitive evidence of TSS conduction, we extracted cyclotron mass of the carriers from

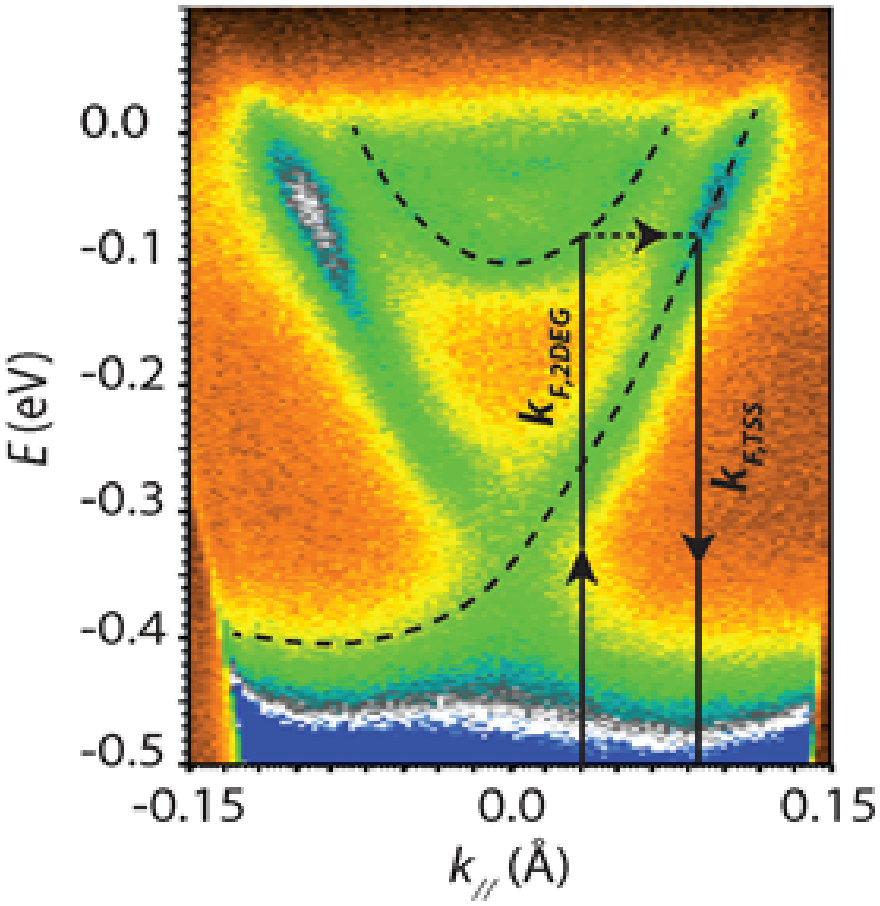

Figure 3.8: Extrapolation of TSS wave vector from that of 2DEG using ARPES of Bi_2Se_3 grown on Al_2O_3. Figure taken from (Koirala et al., 2015).

cyclotron measurement using time domain magneto-optical THz(TDMTS)[4] measurement. As we will discuss later, TSSs carriers show peculiar dependency of their cyclotron mass on Fermi level, which helps us to distinguish them from bulk or non-topological 2DEG carriers.

Time domain magneto-optical THz measurement

Cyclotron resonance can be observed in complex Faraday rotation measurements in TDMTS. We refer the readers to (Wu et al., 2015) for details of the measurement geometry and here

[4]THz measurement was done by Liang Wu and Pro. N. Peter Armitage at the Johns Hopkins University.

simply outline the measurement procedure. In order to measure the complex Faraday rotation (FR), the phase modulation technique was used to measure the polarization states accurately which allows us to measure Exx(t) and Exy(t) simultaneously in a single scan. Faraday rotation can be obtained by θ_F = arctan(Exy(ω)/Exx(ω) = θ'_F +i θ''_F after Fourier transforming into the frequency domain.As we will see later,the dip position in the imaginary part indicates cyclotron resonance (CR) frequency. The negative Faraday rotation indicates that carriers are electrons in both films. We fit the data by Drude-Lorentz model with a Drude term, a phonon term and a term for the background dielectric constant (ϵ_{inf}) coming from higher energy absorptions. The formula for conductance in magnetic field is :

$$G_{\pm} = -i\epsilon_0\omega d[\frac{\omega_{pD}^2}{-\omega^2 - i\Gamma_D\omega \mp \omega_c\omega} + \frac{\omega_{pDL}^2}{\omega_{DL}^2 - \omega^2 - i\Gamma_{DL}\omega \mp \omega_{cDL}\omega} + \epsilon_{\text{inf}} - 1] \tag{3.3}$$

where ω_p's represents the plasma frequencies, Γ's represents scattering rates, d is the film thickness and the $\pm$ sign denotes the response to right/left circularly polarized light respectively. We constrained the parameters of the phonon and the high-frequency terms by those extracted from zero-field conductance value (as explained below) and only allowed the cyclotron frequency (ω_c) and the scattering rate to vary. From $G_{\pm}$ we can calculate the complex transmission for right and left circularly polarized light $t_{\pm}$. Then we can calculate the complex FR by $tan(\theta_F) = -i(t_+ - t_-)/(t_+ + t_-)$. From the fits we can accurately extract the cyclotron frequency, ω_c, for the Drude component from which the cyclotron mass (m^*) is calculated using ω_c = eB /($2\pi m^*$).Similarly, we fitted the zero field real conductance spectra by an oscillator model with a Drude term describing free electron-like motion, a Drude-Lorentz term modeling the phonon and a lattice polarizability (ϵ_{inf}) term that originates from absorptions outside the spectral range.

$$G(\omega) = [\frac{\omega_{pD}^2}{i\omega - \Gamma_D} - \frac{i\omega\omega_{pDL}^2}{\omega_{DL}^2 - \omega^2 - i\Gamma_{DL}\omega} - i(\epsilon_{\text{inf}} - 1)]\epsilon_0 d \tag{3.4}$$

Cyclotron mass and carrier density

CR measurement using TDMTS were performed on two 16 QL films grown on BIS-BL: this measurement provides cyclotron mass (m^*), total sheet carrier density (n_{tot}) and average mobility ($\mu_{optical}$). To prevent ambient contamination during ~1 day delay between growth (at Rutgers University) and TDMTS measurement (at the Johns Hopkins University), one

film was capped by ∼20 nm Se and another was capped by ∼50 nm MoO_3. Sharp CR

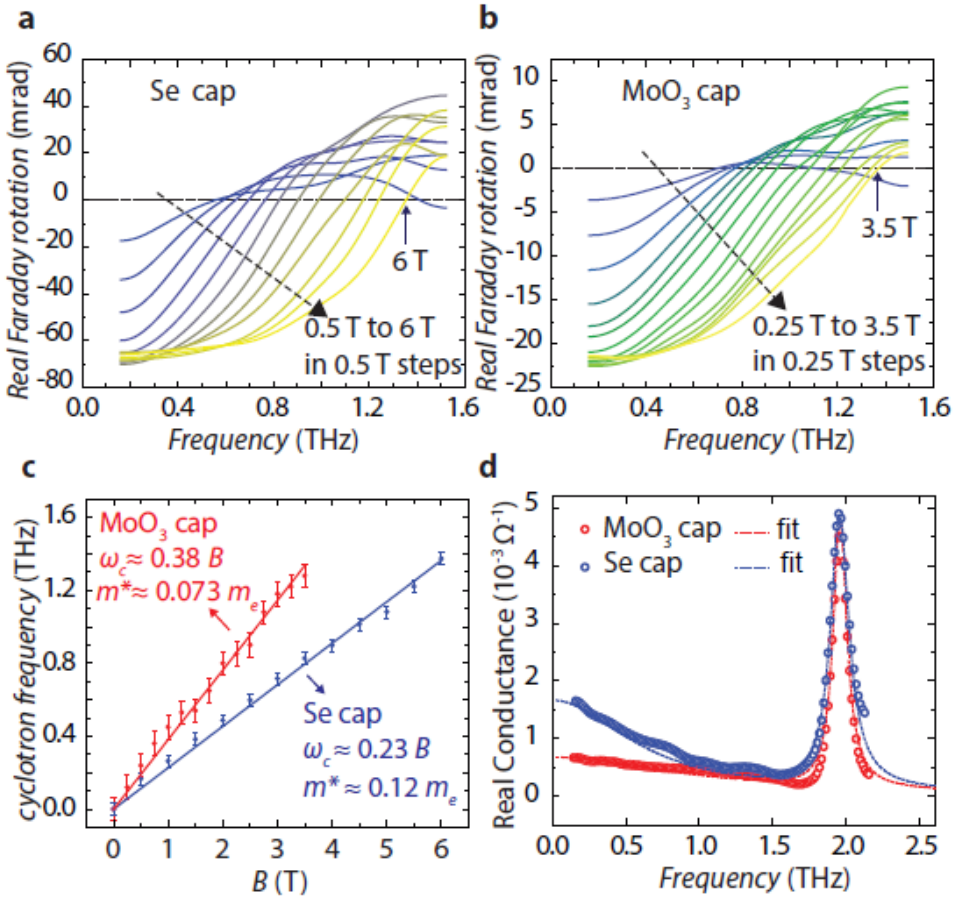

Figure 3.9: **Cyclotron resonance and zero field real conductance of two 16 QL thick Bi_2Se_3 films grown on BIS-BL and capped by 20 nm Se and 50 nm MoO_3 respectively:** Real part of complex Faraday rotation at different magnetic fields for (a) Se-capped and (b) MoO_3-capped film. For both (a) and (b), dashed arrows indicate the direction of increasing magnetic field. (c) CR frequencies at different magnetic fields for both films. Solid lines are linear fit of $\omega_c = eB/(2\pi m^*)$. (d) Zero field real conductance as a function of frequency along with Drude-Lorentz fit for both films. The peaks near 1.9 THz correspond to bulk phonon mode of Bi_2Se_3. Figure taken from (Koirala et al., 2015).

features were observed in measurements of the complex Faraday rotation (FR) angle. Figure 3.9a (Fig. 3.9b) shows the real part of Faraday rotation (FR) for a Se- (MoO_3-) capped film for different magnetic fields. The inflection point of real part of the FR represents the CR, which shifts to higher frequency with increasing B. As shown in Fig. 3.9c for both samples, fitting the FR data provides the CR frequency (ω_c) for each B from which m^* is obtained by using a linear fit $\omega_c = eB/(2\pi m^*)$. In order to obtain n_{tot} and $\mu_{optical}$, we extracted

spectral weight (ω_{pD}^2) and scattering rate (Γ_D) from the DrudeLorentz fit of the zero field real conductance shown in Fig. 3.9d .

We can then get $\mu_{optical}$ = e/($2\pi\Gamma_D$ m*) and n_{tot} from:

$$\omega_{pD}^2 d = \frac{n_{tot} e^2}{m^* \epsilon_0} \tag{3.5}$$

Additionally, if the carriers populate the TSS, then the Fermi wave-vector (k_F) can be obtained solely from spectral weight using:

$$\omega_{pD}^2 d = \frac{k_F(A + 2Bk_F)e^2}{2\pi\hbar^2\epsilon_0} \tag{3.6}$$

where e is the electronic charge, ϵ_0 is the free-space permittivity, and A = 2.02 eVÅ and B = 10.44 eVÅ^2 are the TSS band parameters up to quadratic term (i.e. $E_{TSS} = Ak + Bk^2$) obtained from the fitting (Jenkins et al., 2010). From k_F, the sheet carrier density (n_{TSS}) and effective mass (m_{TSS}) of Dirac-like TSS carriers can be calculated using $n_{TSS} = k_F^2/(2\pi)$ (assuming similar carrier density for two TSSs, which is consistent with Hall measurement) and $m_{TSS} = \hbar k_F/v_F$, where v_F=$dE/\hbar dk$ is the Fermi velocity of TSS.

film	$\omega_{pD}^2 d$ (THz^{2}nm)	m^*/m_e	m_{TSS}/m_e	n_{tot} (10^{12} cm^{-2})	n_{TSS} (10^{12} cm^{-2})	$\mu_{optical}$ (cm^{2}V^{-1}s^{-1})	n_{sheet} (10^{12} cm^{-2})	μ_{Hall} (cm^{2}V^{-1}s^{-1})
Se-capped	2.3 ± 0.1×10^4	0.12 ± 0.01	0.12 ± 0.01	3.5 ± 0.2	3.4 ± 0.2	4,700	3.1	3,600
MoO_3-capped	1.2 ± 0.1×10^4	0.073 ± 0.007	0.080 ± 0.005	1.1 ± 0.2	1.2 ± 0.2	3,800	1.1	3,300
Uncapped	-	-	-	-	-	-	1.3	11,400

Figure 3.10: **Cyclotron resonance measurement confirming the TSS transport:** Spectral density ($\omega_{pD}^2 d$) is obtained from fit of zero field real conductance in TDMTS measurement. Calculated effective mass of TSS (m_{TSS}) agrees with cyclotron mass (m^*) as do optical sheet carrier densities, n_{tot} and n_{TSS}, obtained from equations (3.5) and (3.6), respectively, indicating TSS as the origin of cyclotron resonance. A comparison of optical sheet carrier densities and mobility ($\mu_{optical}$) with Hall sheet carrier density (n_{sheet}) and Hall mobility (μ_{Hall}), respectively, is also presented. For the uncapped film no optical measurements were performed due to surface aging effect. Figure taken from (Koirala et al., 2015).

In Fig. 3.10, we list $\omega_{pD}^2 d$, m^*, m_{TSS}, n_{tot}, n_{TSS}, $\mu_{optical}$, Hall carrier density (n_{sheet}) and Hall mobility (μ_{Hall}) for the two samples (Hall data were obtained from different but

nominally identically prepared samples as those used in TDMTS measurement). In addition, Hall data for a fresh uncapped 15 QL thick film is also shown for comparison. For calculation of $\mu_{optical}$, Γ_D of 0.5 THz and 1 THz were used for Se-capped and MoO_3-capped films, respectively. The smaller mobilities obtained for capped samples as compared to uncapped one implies that the capping layers introduce additional surface-scattering sites: in the case of the Se capping, additional carriers as well. From Fi.3.10 we can see a reduced carrier density for MoO_3-capped film as compared to the Se-capped one because MoO3 depletes (n-type) carriers from Bi_2Se_3 due to its higher electron affinity. The correspondingly smaller $m^* \approx 0.073m_e$ in $MoO_3$3-capped sample compared to $m^* \approx 0.12m_e$ for Se-capped sample is strong evidence that CR comes from TSS carriers because the effective masses of bulk or 2DEG carriers are carrier density independent ($\sim 0.11 - 0.13m_e$) (Analytis et al., 2010a; Bianchi et al., 2010), while the effective mass of Dirac-like carriers in TSS scales with carrier density ($m_{TSS} \propto k_F \propto \sqrt{n_{TSS}}$). Agreement between measured m^* and calculated m_{TSS} gives quantitative evidence of CR originating from TSS carriers. Additionally, agreement between n_{tot}, n_{TSS} and n_{sheet} indicate that the TSS conduction accounts for total observed carriers in these films.

3.3 Conclusion

In conclusion, commonly available substrates are not an ideal growth template for the TI Bi_2Se_3, which inevitably suffers from both interfacial and bulk defects. However, the flexibility of MBE has allowed us to engineer an atomic-scale virtual substrate that is tailored to produce high-quality Bi_2Se_3 thin films. We have shown that this scheme significantly lowers interfacial and bulk defects, resulting in the highest reported mobility of TSS channels. The development of such high mobility TI films is a major step toward accessing new quantum phenomena, which have been inaccessible to most experimental probes due to parallel bulk conduction and low mobilities.

Chapter 4

Observation of QHE from topological surface states

In topological insulators (TIs), Dirac-like nature of topological surface states (TSSs) results in an unusual Landau level structure leading to half-quantized quantum Hall effect (QHE) from each surface (See (Morimoto et al., 2015) and references therein). Until recently, no QHE was observed in TI compounds due to high carrier density and conducting bulk. Here we show that Bi_2Se_3 thin films grown on BIS-BL buffer layer show QHE that originate from TSSs. Furthermore,by changing substrate from Al_2O_3 to $SrTiO_3$, we have been able to study QHE in TIs as a function of gate voltage.

4.1 QHE from topological surface states versus regular 2DEGs

As we discussed in Chapter 1, in perpendicular magnetic fields the parabolic dispersion ($E \sim k^2$) of normal 2DEGs changes into discreet Landau levels given by $E_n = \hbar\omega_c(n+1/2)$, where $\omega_c = eB/m^*$ is the cyclotron frequency and n = 0,1,2... denotes the LL index. Such LL structure leads to QHE where the Hall conductance is quantized as $\sigma_{xy} = \frac{\nu e^2}{h}$ where ν = n + 1 = 1,2,3 etc.. On the other hand for Dirac-like TSSs with $E \sim k$ dispersion, LLs are given by $E_n = sgn(n)v_F\sqrt{2e\hbar|n|B}$, where n = 0, ±1,±2....(Cheng et al., 2010; Goerbig, 2011; Hanaguri et al., 2010). Such LL structure leads to QHE from TSS which are quantized as $\sigma_{xy} = \frac{\nu e^2}{h}$ (for each surface), where ν = n +1/2 = ±1/2,±3/2,±5/2 etc...

It is clear to see that σ_{xy} from one surface of TIs would then be quantized at half-integer values, which is in contrast to integered values of σ_{xy} observed in normal 2DEG. Such half-integer quantization of σ_{xy} is an inherent feature of Dirac-like electrons. We must now mention that in an experiment both surfaces of TIs are measured simultaneously. Then in

an experiment total Hall conductance ($\sigma_{xy,total}$) is sum of Hall conductance from top surface ($\sigma_{xy,T}$) and Hall conductance from bottom surface ($\sigma_{xy,B}$).Then $\sigma_{xy,total} = \sigma_{xy,T} + \sigma_{xy,B} = (n_T + \frac{1}{2})\frac{e^2}{h} + (n_B + \frac{1}{2})\frac{e^2}{h} = (n_B + n_T + 1)\frac{e^2}{h}$, where n_T and n_B are LL indices of top and bottom surface states respectively. Therefore in QHE experiment of TIs, the measured quantity i.e. $\sigma_{xy,total}$ is always integered valued. In fact since Dirac electrons are always predicted to come in pairs by the so called no-go theorem, half-integered values of σ_{xy} is impossible to measure in the context of Dirac electrons (Nielsen and Ninomiya, 1981).

Now if the top and bottom surfaces are degenerate (i.e. $n_T = n_B$), then $n_T + n_B$ always results in an even-number. Therefore $\sigma_{xy,total} = (n_B + n_T + 1)\frac{e^2}{h} = (even - number + 1)\frac{e^2}{h}$ is only odd integered. However, in real samples the top and bottom surfaces are not guranteed to be degenerate (for example top and bottom surface could have different carrier densities) and $\sigma_{xy,total}$ takes on both even and odd values (Xu et al., 2014; Yoshimi et al., 2015). However, in principle, top and bottom surfaces can be made degenerate (for example by applying top and bottom gating to independently control the carrier density of top and bottom surfaces) and then $\sigma_{xy,total}$ can be made to have odd integered values only. Having discussed the conceptual aspects of QHE from TIs, we next discuss the experimental results.

4.1.1 QHE in Bi_2Se_3 grown on In_2Se_3 based buffer layer

For QHE measurement we grew an 8 QL thick Bi_2Se_3 on BIS-BL buffer layer (as explained in previous chapter) and capped it with both MoO_3 and Se in order to prevent ambient contamination of the film. The film was then taken to National High Magnetic Field Lab in Tallahasse, Florida and measured in perpendicular magnetic fields upto ± 34.5 T. Immediately before measurement, sample was hand patterened into *mm-sized* Hall bar pattern.

Figure 4.1a and 4.1b show the Hall (R_{Hall}) and the longitudinal sheet resistance (R_{sheet}), respectively, as a function of magnetic field at various temperatures for this film. The sheet carrier density of the film was $\sim 7 \times 10^{11}$ cm^{-2} as measured from low field Hall slope ($\leq$ 9 T). The data for 0.3 K shows that R_{sheet} vanishes (0.0 ± 0.5) above 31 T indicating dissipationless transport, with simultaneous perfect quantization of R_{Hall} = (1.00000 ± 0.00004)h/e2 (25813 ± 1) above 29 T. These measurements correspond to $\sigma_{xy,total} = \frac{e^2}{h}$.

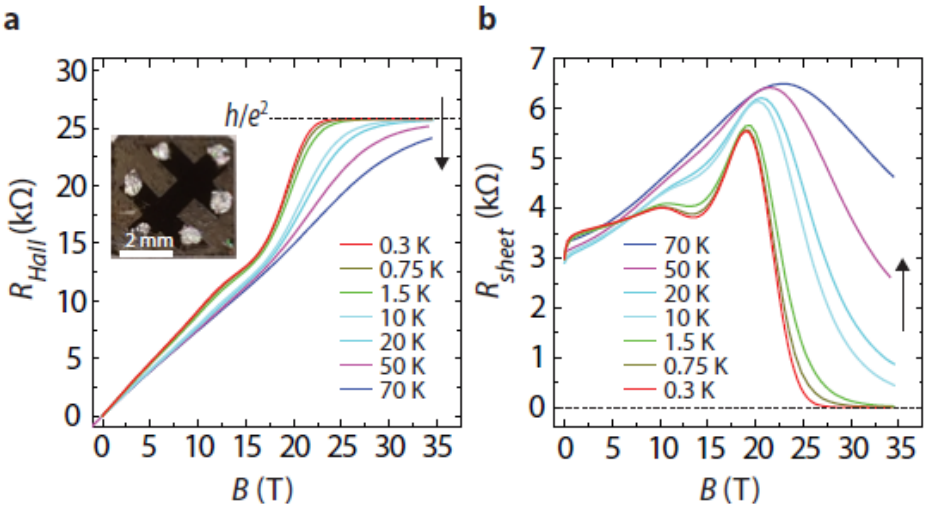

Figure 4.1: **Quantum Hall Effect in an 8 QL thick Bi_2Se_3 film grown on BIS-BL and capped by both MoO_3 and Se:** (a) Hall resistance at different temperatures in magnetic field up to 34.5 T, which quantizes to $(1.00000 \pm 0.00004)h/e^2$ ($25813 \pm 1\ \Omega$) at low temperatures. The inset shows the Hall-bar pattern of the measured film. (b) Corresponding longitudinal sheet resistance, which drops to zero ($0.0 \pm 0.5\ \Omega$) when Hall resistance quantizes to h/e^2. The vertical arrows indicate the direction of increasing temperature. Figure taken from (Koirala et al., 2015).

Together these indicate that E_F of both the top and bottom surface states have fallen below the first Landau level. As shown in Fig. 4.1a and 4.1b, at the maximum field the quantum-Hall-plateau vanishes between 20 to 50 K, but hints of the QHE persists even up to 70 K. We have shown that TSSs transport dominate in these films with highly insulating bulk, and therefore, the QHE must come from TSSs.

4.2 Gate tuned QHE in TI films

Ability to tune sheet carrier density(or equivalently E_F) gives an opportunity to measure how transport characteristics change with E_F. Experimentally, this is done by applying gate voltage to the sample. In principle, such gate voltage could be applied from either top or bottom (or both) sides of the film. However, this is not an easy task to do for Bi_2Se_3 films grown on Al_2O_3 since the thickness of Al_2O_3 substrate ($\sim$500 μm) prohibits efficient back gating due to its low dielectric constant ($\sim$9 - 11), while extensive lithographic process involved in top-gate fabrication create increased defects leading to high carrier density,

which makes it difficult to effectively tune the chemical potential through the Dirac point of TSSs. We can circumvent this problem by replacing Al_2O_3 with ∼500 μm $SrTiO_3$ substrate for the buffer layer growth, which owing to its large dielectric constant of ∼20,000 at low temperature ($\leq$ 20 K) allows for efficient gating of Bi_2Se_3 films (Müller and Burkard, 1979). By applying gate voltage, we have observed not only surface dominated transport in these films but also TSSs originated QHE in high magnetic fields.

4.2.1 Ambipolar transport: TSS dominated transport

We substitued Al_2O_3 with $SrTiO_3$ for the In_2Se_3 based buffer layer growth. Furthermore, we made the buffer layer thinner, which now consists of 5 QL In_2Se_3 - 4 QL $(Bi_{0.5}In_{0.5})_2Se_3$ (We will continue to call it BIS-BL). The rest of the film structure remains the same. The reason for thinning the BiS-BL is that we want to apply back gating and thinner BIS-BL makes gating more efficient. Structurally, films grown on top of $SrTiO_3$ are of slightly inferior quality to those grown on Al_2O_3. Films were capped by 50 nm MoO_3/ 50 nm Se to protect against ambient contamination. MoO_3 capping also lowers the sheet carrier density of thin films (Edmonds et al., 2014), which helps to gate the thin films efficiently. ∼50 nm thick Cu was sputtered onto back of the substrate to act as back gate lead. *mm-sized* Hall bar structure were then hand patterned and pressed indium wires were used to make electrical contacts.

We report on measurements done in two different films: one 8 QL thick and the other 10 QL. We measured the 8 QL thick film in AMI system with base T = 1.5 K and maximum B = ± 9 T. Figure 4.2a shows Hall resistance (R_{Hall}; left side) and sheet resistance (R_{sheet}; right side) as a function of magnetic field for different applied gate voltages. As back gate voltage (V_G) is decreased from 0 V to -15 V, the magnitude of (negative) Hall slope increases and then starts to decrease for V_G <-15 V, crossing over to positive values for V_G < -35 V. Similarly R_{sheet} increases upto V_G = -20 V and decreases for V_G < -35 V. This behavior is clearly evident in Fig. 4.2b and in Fig. 4.2c, where we have plotted zero field conductance (σ_{xx}) and n_{sheet}, respectively, using data obtained from Fig.4.2a. A clear minimum in conductance and change of sign for carrier type is observed between -35 V < V_G < -20 V, indicating tuning of the chemical potential through the Dirac point.The

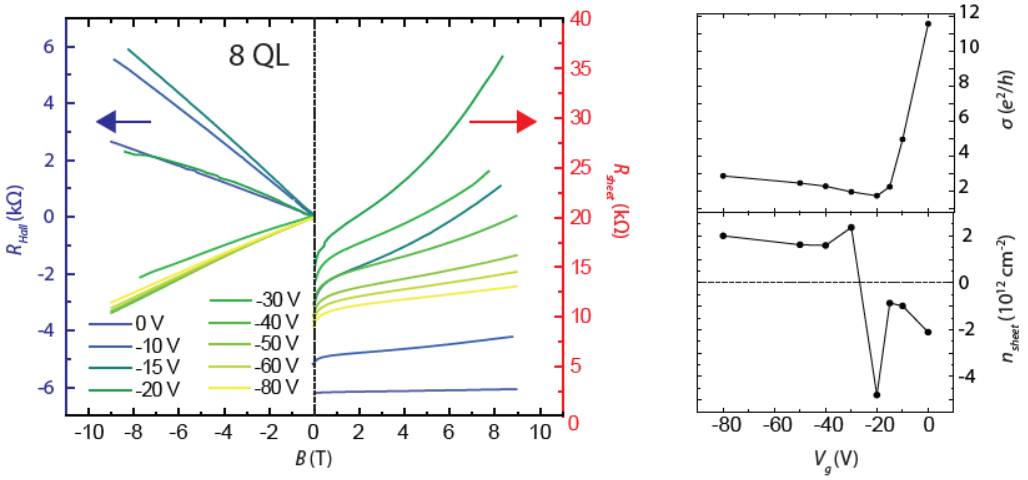

Figure 4.2: R_{Hall}, R_{sheet}, σ_{xx} **and** n_{sheet} **of an** MoO_3**/Se capped 8 QL thick** Bi_2Se_3 **film grown on BIS-BL at different gate voltages:** (a) Slope of R_{Hall} changes from negative to positive (left panel) and R_{sheet} increases and then decreases(right panel) as V_G decreases from 0 to -80 V. (b) σ_{xx} and (c) $n_{sheet} \equiv \frac{1}{e \times dR_{Hall}/dB}$ extracted from (a) clearly show the minimum in conductivity and change in carrier type, respectively, at $V_G \sim 30$ V indicating that the E_F goes through the Dirac point.

anomalous increase in n_{sheet} near the charge neutrality point (-35 V $< V_G <$ -20 V) is an effect of competition between p- and n-type carriers, which tend to cancel the Hall signal, thus resulting in apparently high n_{sheet}. Such effect has been previously attributed to formation of electron-hole puddles in TIs due to insufficient screening of impurity potential at very low carrier densities (Adam et al., 2012; Kim et al., 2012). For $V_G <$ -35 V, R_{Hall} is nearly linear again and the (positive) slope decreases with decreasing V_G indicating that the carriers change completely to p-type.This simultaneous observation of minimum in σ_{xx} and change in carrier type with application of V_G is consistent with E_F passing through the Dirac point of TSSs as shown schematically in Fig 4.3. Therefore, such ambipolar behavior clearly indicates that the conduction is dominated by TSS channel.

4.2.2 Odd integered QHE from TSSs

We also measured a 10 QL thick film on magnetic field upto 34.5 T at T = 0.35 K. Figure 4.4a shows R_{sheet} (right side) and R_{Hall} (left side) as a function of magnetic field for different back gate voltages. The low field results are qualitatively similar to those for 8 QL sample,

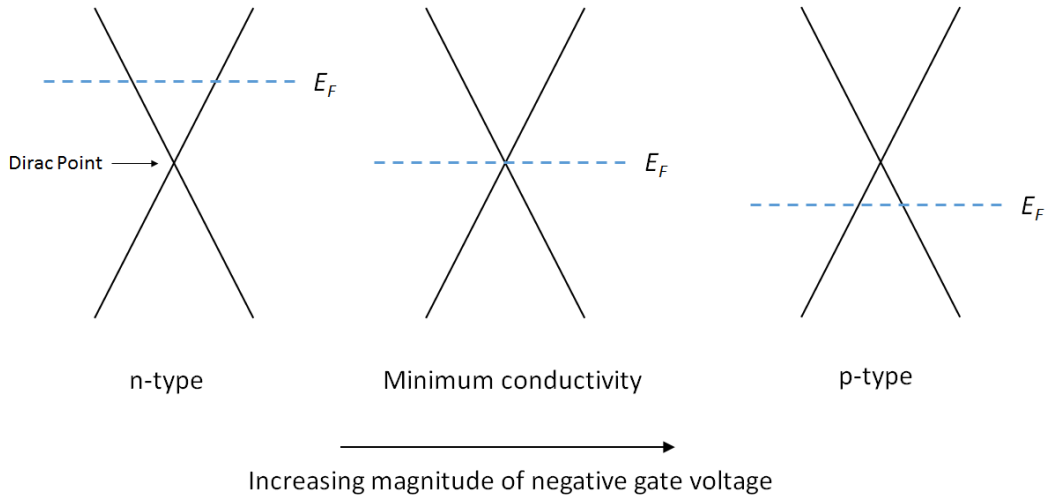

Figure 4.3: **Cartoon of evolution of E_F with gate voltage:** With increasing magnitude of V_G, E_F goes from upper Dirac cone with n-type carriers (left) through the Dirac point (middle) to the lower Dirac cone with p-type carriers (right). At the Dirac point, the conductivity is minimum.

again indicating that TSS conduction dominate in this film. One notable difference from 8 QL film is that R_{Hall} for 10 QL film becomes quite non-linear for $V_G < V_{G0}$ = -58 V, where we define V_{G0} as the V_G where zero field R_{sheet} shows a peak (See inset of Fig. 4.4a). For V_G = -70 V, R_{Hall} shows strong non-linearity and fluctuates around zero. For V_G = -100 V, while it is still non-linear, the overall slope of R_{Hall} is positive which indicates that the majority carriers in the film are now holes rather than the electrons. A likely scenario is that due to the increased thickness of 10 QL sample, gating becomes less effective at the top surface compared to 8 QL film resulting in increased non-linearity of R_{Hall} observed for $V_G < V_{G0}$. Now we discuss the high field behavior of R_{Hall} and R_{sheet} shown in Fig. 4.4a. For -40V $< V_G <$ 0 V, with decreasing V_G, increasingly developed plateaus in R_{Hall} are observed around $\frac{h}{e^2}$, while dips in R_{sheet} are also observed both of which are hallmarks of the QHE. We note that the minimum value of R_{sheet} we observe is $\sim$300 Ω rather than the ideal value of 0, which indicates that some dissipative channels exist in the film even in QH insulator state. This is in contrast to films grown on Al_2O_3, where truly dissipationless transprot was observed. This observation is consistent with structural inferiority of films grown on $SrTiO_3$. In order to get a clearer picture of all the features observed in R_{Hall}, we took derivative of R_{Hall} w.r.t. magnetic field (dR_{Hall}/dB). In Fig.4.42b, we plot R_{sheet},

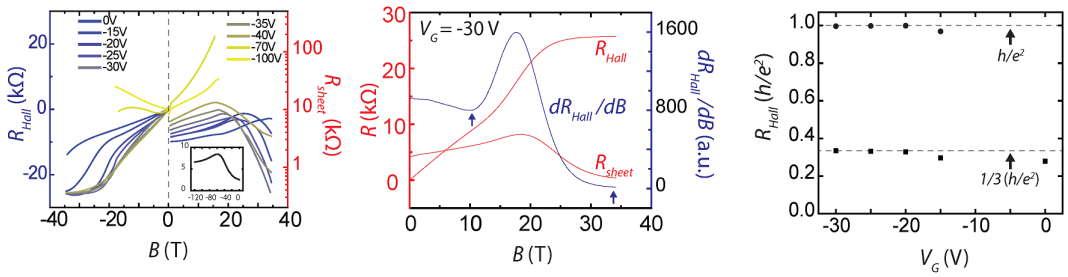

Figure 4.4: **Evolution of QHE with gate voltage in a MoO_3/Se capped 10 QL thick Bi_2Se_3 film grown on BIS-BL:** (a) For -40V $< V_G <$ 0 V R_{Hall} (left panel) and R_{sheet} (right panel) show increasingly developed plateau at $\approx h/e^2$ and dip towards 0, respectively, indicating QHE. The inset shows zero-field R_{sheet} as function of V_G. (b) minimium (zero) in dR_{Hall}/dB represents developing (fully developed) plateau in R_{Hall} as indicated by vertical arrows(c) R_{Hall} plateaus at h/e^2 and developing plateaus at $h/3e^2$ are observed for several V_G values, which indicates degeneracy between top and bottom surfaces.

R_{Hall} and R_{Hall}/dB for V_G = -30 V. As indicated by vertical arrows, R_{Hall}/dB plot goes to zero (shows a minima) at B = ∼33 T (∼10 T), which corresponds to a fully developed (developing) plateau in R_{Hall}. We have followed similar procedures for other V_G values and plotted the results in Fig. 4.4c. Only R_{Hall} plateaus at $\frac{h}{e^2}$ and developing plateaus at $\frac{h}{3e^2}$ are observed, while we did not observe any plateau-like features at $\frac{h}{2e^2}$. Such odd integered R_{Hall} plateaus are hallmarks of QHE originating from Dirac-like TSS carriers when the top and bottom surfaces are degenerate. We did not observe either dips in R_{sheet} or plateaus in R_{Hall} for Vg = -70 V and -100 V. In fact, for these V_G values, R_{sheet} monotonically increases with B without sign of saturation. More experimental data is required to fully understand why QHE seems to disppear on the p-type side of the film. However,we point out that scanning tunneling spectroscopy studies performed in Bi_2Se_3 measure LL spectrum only discerned LL ≥ 0 (i.e. on the n-type side) (Cheng et al., 2010; Hanaguri et al., 2010). Lack of observation of QHE in p-type regime in our measurement is consistent with this result. Hanaguri et al. listed smaller Fermi velocity of TSS on p-type side and proximity of Dirac cone to bulk valence band as possible reasons for suppression of LL < 0 (Hanaguri et al., 2010). Further studies will be required to fully understand this issue.

4.3 Conclusion

In TIs, Dirac-like nature of TSSs results in an unusual Landau level structure leading to quantum Hall effect (QHE) from each surface. We have observed dissipation-less QHE in Bi_2Se_3 grown on BIS-BL (on Al_2O_3). By substituting Al_2O_3 with $SrTiO_3$ substrates, we achieved not only ambipolar transport but also observed the gate-voltage dependence of TSS originated QHE. Of particular interest are the $\nu = 1$, 3 states that signify the TSS origin of QHE in n-type region and absence of QHE in p-type region. .

Chapter 5

Epilogue

The field of topological insulators has expanded considerably since its inception only ten years ago. Initially, surface sensitive probes such as ARPES and STM were used to rapidly confirm the existence of topological insulator phase in its most studied host material system: the pnictogen-chalcogenide compounds. Even though they have a promising band structure with relatively large bulk band gap and single Dirac-like topological surface state, these layered compounds have high defect density leading to highly conducting bulk. A major effort in the field has been to minimize the bulk conduction. While several routes along the lines of compensation doping have been pursued to minimize net defect density, in this dissertation we have focused on a different route, whence we have grown cleaner films and thus reduced the total defect density in these films.

5.1 Summary of results

In Chapter 3, we discussed growth of Bi_2Se_3 on artificially create buffer layer based on In_2Se_3. The structural and chemical compatibility between the two compounds led to growth of high quality films. Using ARPES and STM we showed that these films are topological insulators. Transport measurement and cyclotron resonance measurement together showed that these films were dominated by record-high-mobility topological surface state carriers. Finally, low carrier density and high mobility led to our observation of topological surface state originated quantum Hall effect.

In Chapter 4, we went a step forward with this idea and replace Al_2O_3 substrate with $SrTiO_3$ substrate .This allowed us to study field effect modulation of these low carrer density Bi_2Se_3 films. The ambipolar transport observed at low magnetic fields showed that the TSS dominate the transport. At high magnetic fields, odd integered QHE was observed on

electron doped side indicating that top and bottom TSSs are degenerately occupied. On the other hand, no signature of QHE was observed on the hole doped side, which while consistent with previous Landau level spectroscopy measurements, needs further study.

5.2 Outlook and Future Research

These high quality thin films have the prospect of being used as the standard template for future experiments on TI films. For example, only very recently Wu et al. (Wu et al. (2016)) used these films to observe axion dynamics and topological magnetoelectric effect. On a different but related field, these films could be used to search for ferromagnetism in magnetically doped Bi_2Se_3, which up to now has not shown a reliable evidence of ferromagnetism. On the other hand, recent observation of room temperature interfacial ferromagnetism in EuS-Bi_2Se_3 system (Katmis et al., 2016) suggests that heterostructures of magnetic insulator -TI could lead to potentially higher Curie temperature and therefore observation of QAHE at higher temperature. The ultimate goal of such approach is to observe quantum anomalous Hall (QAHE) effect in Bi_2Se_3. Yet another direction for future research would be to use layered superconductors such as FeSe or $NbSe_2$ to grow Bi_2Se_3 and search for topological superconductivity and Majoranan modes (Qi and Zhang, 2011).

On the application side, in addition to producing high quality samples, these samples will also need to be protected against ambient contamination, which tend to rapidly degrade their electrical properties. Appropriate capping materials could alleviate this situation. In this context newer TI materials should also be pursued. Recent predictions of TI phase in oxides (Yan et al., 2013) is an exciting development in this front, since oxides are much more stable against ambient contamination.

References

Adam, S., Hwang, E., and Sarma, S. D. (2012). Two-dimensional transport and screening in topological insulator surface states. *Physical Review B*, 85(23):235413.

Analytis, J. G., Chu, J.-H., Chen, Y., Corredor, F., McDonald, R. D., Shen, Z., and Fisher, I. R. (2010a). Bulk Fermi surface coexistence with Dirac surface state in Bi2Se3: A comparison of photoemission and Shubnikov–de Haas measurements. *Physical Review B*, 81(20):205407.

Analytis, J. G., McDonald, R. D., Riggs, S. C., Chu, J.-H., Boebinger, G., and Fisher, I. R. (2010b). Two-dimensional surface state in the quantum limit of a topological insulator. *Nature Physics*, 6(12):960–964.

Avron, J. E., Osadchy, D., and Seiler, R. (2003). A topological look at the quantum Hall effect. *Physics Today*, 56(8):38–42.

Bansal, N., Kim, Y. S., Brahlek, M., Edrey, E., and Oh, S. (2012). Thickness-independent transport channels in topological insulator Bi2Se3 thin films. *Physical Review Letters*, 109(11):116804.

Bansal, N., Kim, Y. S., Edrey, E., Brahlek, M., Horibe, Y., Iida, K., Tanimura, M., Li, G.-H., Feng, T., Lee, H.-D., et al. (2011). Epitaxial growth of topological insulator Bi2Se3 film on Si(111) with atomically sharp interface. *Thin Solid Films*, 520(1):224–229.

Bansal, N., Koirala, N., Brahlek, M., Han, M.-G., Zhu, Y., Cao, Y., Waugh, J., Dessau, D. S., and Oh, S. (2014). Robust topological surface states of Bi2Se3 thin films on amorphous SiO2/Si substrate and a large ambipolar gating effect. *Applied Physics Letters*, 104(24):241606.

Bauer, E. (1958). Phänomenologische theorie der kristallabscheidung an oberflächen. ii. *Zeitschrift für Kristallographie-Crystalline Materials*, 110(1-6):395–431.

Bergman, G. (1982). Influence of spin-orbit coupling on weak localization. *Physical Review Letters*, 48(15):1046.

Bernevig, B. A., Hughes, T. L., and Zhang, S.-C. (2006). Quantum spin Hall effect and topological phase transition in HgTe quantum wells. *Science*, 314(5806):1757–1761.

Bernevig, B. A. and Zhang, S.-C. (2006). Quantum spin Hall effect. *Physical Review Letters*, 96(10):106802.

Berry, M. V. (1984). Quantal phase factors accompanying adiabatic changes. In *Proceedings of the Royal Society of London A: Mathematical, Physical and Engineering Sciences*, volume 392, pages 45–57. The Royal Society.

Bianchi, M., Guan, D., Bao, S., Mi, J., Iversen, B. B., King, P. D., and Hofmann, P. (2010). Coexistence of the topological state and a two-dimensional electron gas on the surface of Bi2Se3. *Nature Communications*, 1:128.

Brahlek, M., Bansal, N., Koirala, N., Xu, S.-Y., Neupane, M., Liu, C., Hasan, M. Z., and Oh, S. (2012). Topological-metal to band-insulator transition in (Bi1-xInx)2Se3 thin films. *Physical Review Letters*, 109(18):186403.

Brahlek, M., Koirala, N., Bansal, N., and Oh, S. (2015). Transport properties of topological insulators: Band bending, bulk metal-to-insulator transition, and weak anti-localization. *Solid State Communications*, 215:54–62.

Brahlek, M., Koirala, N., Salehi, M., Bansal, N., and Oh, S. (2014). Emergence of decoupled surface transport channels in bulk insulating Bi2Se3 thin films. *Physical Review Letters*, 113(2):026801.

Butch, N. P., Kirshenbaum, K., Syers, P., Sushkov, A. B., Jenkins, G. S., Drew, H. D., and Paglione, J. (2010). Strong surface scattering in ultrahigh-mobility bi 2 se 3 topological insulator crystals. *Physical Review B*, 81(24):241301.

Cao, H., Venkatasubramanian, R., Liu, C., Pierce, J., Yang, H., Hasan, M. Z., Wu, Y., and Chen, Y. P. (2012). Topological insulator Bi2Te3 films synthesized by metal organic chemical vapor deposition. *Applied Physics Letters*, 101(16):162104.

Chakhalian, J., Freeland, J. W., Millis, A. J., Panagopoulos, C., and Rondinelli, J. M. (2014). Colloquium: Emergent properties in plane view: Strong correlations at oxide interfaces. *Reviews of Modern Physics*, 86(4):1189.

Chang, C.-Z., Zhang, J., Feng, X., Shen, J., Zhang, Z., Guo, M., Li, K., Ou, Y., Wei, P., Wang, L.-L., et al. (2013). Experimental observation of the quantum anomalous Hall effect in a magnetic topological insulator. *Science*, 340(6129):167–170.

Chen, Y., Analytis, J., Chu, J.-H., Liu, Z., Mo, S.-K., Qi, X.-L., Zhang, H., Lu, D., Dai, X., Fang, Z., et al. (2009). Experimental realization of a three-dimensional topological insulator, Bi2Te3. *Science*, 325(5937):178–181.

Cheng, P., Song, C., Zhang, T., Zhang, Y., Wang, Y., Jia, J.-F., Wang, J., Wang, Y., Zhu, B.-F., Chen, X., et al. (2010). Landau quantization of topological surface states in Bi2Se3. *Physical Review Letters*, 105(7):076801.

Chern, S.-s. (1946). Characteristic classes of Hermitian manifolds. *Annals of Mathematics*, pages 85–121.

Christen, H. M. and Eres, G. (2008). Recent advances in pulsed-laser deposition of complex oxides. *Journal of Physics: Condensed Matter*, 20(26):264005.

Edmonds, M. T., Hellerstedt, J. T., Tadich, A., Schenk, A., ODonnell, K. M., Tosado, J., Butch, N. P., Syers, P., Paglione, J., and Fuhrer, M. S. (2014). Air-stable electron depletion of Bi2Se3 using molybdenum trioxide into the topological regime. *ACS nano*, 8(6):6400–6406.

Emziane, M., Marsillac, S., and Bernede, J. (2000). Preparation of highly oriented α-In2Se3 thin films by a simple technique. *Materials chemistry and physics*, 62(1):84–87.

Freund, L. B. and Suresh, S. (2004). *Thin film materials: stress, defect formation and surface evolution*. Cambridge University Press.

Fu, L. and Kane, C. L. (2007). Topological insulators with inversion symmetry. *Physical Review B*, 76(4):045302.

Fu, L., Kane, C. L., and Mele, E. J. (2007a). Topological insulators in three dimensions. *Physical Review Letters*, 98(10):106803.

Fu, L., Kane, C. L., and Mele, E. J. (2007b). Topological insulators in three dimensions. *Physical Review Letters*, 98(10):106803.

Goerbig, M. (2011). Electronic properties of graphene in a strong magnetic field. *Reviews of Modern Physics*, 83(4):1193.

Goetzberger, A., Klausmann, E., and Schulz, M. (1976). Interface states on semiconductor/insulator surfaces. *Critical Reviews in Solid State and Material Sciences*, 6(1):1–43.

Guo, X., Xu, Z., Liu, H., Zhao, B., Dai, X., He, H., Wang, J., Liu, H., Ho, W., and Xie, M. (2013). Single domain Bi2Se3 films grown on InP(111) A by molecular-beam epitaxy. *Applied Physics Letters*, 102(15):151604.

Haldane, F. D. M. (1988). Model for a quantum Hall effect without Landau levels: Condensed-matter realization of the" parity anomaly". *Physical Review Letters*, 61(18):2015.

Hampden-Smith, M. J. and Kodas, T. T. (1995). Chemical vapor deposition of metals: Part 1. An overview of CVD processes. *Chemical Vapor Deposition*, 1(1):8–23.

Hanaguri, T., Igarashi, K., Kawamura, M., Takagi, H., and Sasagawa, T. (2010). Momentum-resolved Landau-level spectroscopy of Dirac surface state in Bi2Se3. *Physical Review B*, 82(8):081305.

Hasan, M. Z. and Kane, C. L. (2010). Colloquium: topological insulators. *Reviews of Modern Physics*, 82(4):3045.

Hellerstedt, J., Edmonds, M. T., Chen, J., Cullen, W. G., Zheng, C., and Fuhrer, M. S. (2014). Thickness and growth-condition dependence of in-situ mobility and carrier density of epitaxial thin-film Bi2Se3. *Applied Physics Letters*, 105(17):173506.

Henini, M. (2012). *Molecular beam epitaxy: from research to mass production*. Newnes.

Hikami, S., Larkin, A. I., and Nagaoka, Y. (1980). Spin-orbit interaction and magnetoresistance in the two dimensional random system. *Progress of Theoretical Physics*, 63(2):707–710.

Hsieh, D., Qian, D., Wray, L., Xia, Y., Hor, Y. S., Cava, R., and Hasan, M. Z. (2008). A topological Dirac insulator in a quantum spin Hall phase. *Nature*, 452(7190):970–974.

Ichimiya, A. and Cohen, P. I. (2004). *Reflection high-energy electron diffraction*. Cambridge University Press.

Javey, A., Kim, H., Brink, M., Wang, Q., Ural, A., Guo, J., McIntyre, P., McEuen, P., Lundstrom, M., and Dai, H. (2002). High-κ dielectrics for advanced carbon-nanotube transistors and logic gates. *Nature Materials*, 1(4):241–246.

Jenkins, G. S., Sushkov, A., Schmadel, D., Butch, N., Syers, P., Paglione, J., and Drew, H. (2010). Terahertz Kerr and reflectivity measurements on the topological insulator Bi2Se3. *Physical Review B*, 82(12):125120.

Jotzu, G., Messer, M., Desbuquois, R., Lebrat, M., Uehlinger, T., Greif, D., and Esslinger, T. (2014). Experimental realization of the topological Haldane model with ultracold fermions. *Nature*, 515(7526):237–240.

Kane, C. L. and Mele, E. J. (2005a). Quantum spin Hall effect in graphene. *Physical Review Letters*, 95(22):226801.

Kane, C. L. and Mele, E. J. (2005b). Z2 topological order and the quantum spin Hall effect. *Physical Review Letters*, 95(14):146802.

Katmis, F., Lauter, V., Nogueira, F. S., Assaf, B. A., Jamer, M. E., Wei, P., Satpati, B., Freeland, J. W., Eremin, I., Heiman, D., et al. (2016). A high-temperature ferromagnetic topological insulating phase by proximity coupling. *Nature*.

Kim, D., Cho, S., Butch, N. P., Syers, P., Kirshenbaum, K., Adam, S., Paglione, J., and Fuhrer, M. S. (2012). Surface conduction of topological Dirac electrons in bulk insulating Bi2Se3. *Nature Physics*, 8(6):459–463.

Kim, K. S., Zhao, Y., Jang, H., Lee, S. Y., Kim, J. M., Kim, K. S., Ahn, J.-H., Kim, P., Choi, J.-Y., and Hong, B. H. (2009). Large-scale pattern growth of graphene films for stretchable transparent electrodes. *Nature*, 457(7230):706–710.

Kim, Y. S., Brahlek, M., Bansal, N., Edrey, E., Kapilevich, G. A., Iida, K., Tanimura, M., Horibe, Y., Cheong, S.-W., and Oh, S. (2011). Thickness-dependent bulk properties and weak antilocalization effect in topological insulator Bi2Se3. *Physical Review B*, 84(7):073109.

Klitzing, K. v., Dorda, G., and Pepper, M. (1980). New method for high-accuracy determination of the fine-structure constant based on quantized Hall resistance. *Physical Review Letters*, 45(6):494.

Kohmoto, M. (1985). Topological invariant and the quantization of the Hall conductance. *Annals of Physics*, 160(2):343–354.

Koirala, N., Brahlek, M., Salehi, M., Wu, L., Dai, J., Waugh, J., Nummy, T., Han, M.-G., Moon, J., Zhu, Y., et al. (2015). Record surface state mobility and quantum Hall effect in topological insulator thin films via interface engineering. *Nano Letters*, 15(12):8245–8249.

Koma, A., Sunouchi, K., and Miyajima, T. (1984). Fabrication and characterization of heterostructures with subnanometer thickness. *Microelectronic Engineering*, 2(1):129–136.

König, M., Wiedmann, S., Brüne, C., Roth, A., Buhmann, H., Molenkamp, L. W., Qi, X.-L., and Zhang, S.-C. (2007). Quantum spin Hall insulator state in HgTe quantum wells. *Science*, 318(5851):766–770.

Laughlin, R. B. (1981). Quantized Hall conductivity in two dimensions. *Physical Review B*, 23(10):5632.

Manfra, M. J. (2013). Molecular beam epitaxy of ultra-high quality AlGaAs/GaAs heterostructures: Enabling physics in low-dimensional electronic systems. *arXiv preprint arXiv:1309.2717*.

Moore, J. E. and Balents, L. (2007). Topological invariants of time-reversal-invariant band structures. *Physical Review B*, 75(12):121306.

Morimoto, T., Furusaki, A., and Nagaosa, N. (2015). Charge and spin transport in edge channels of a $\nu = 0$ quantum Hall system on the surface of topological insulators. *Physical Review Letters*, 114(14):146803.

Müller, K. A. and Burkard, H. (1979). SrTiO3: An intrinsic quantum paraelectric below 4 K. *Physical Review B*, 19(7):3593.

Nielsen, H. B. and Ninomiya, M. (1981). A no-go theorem for regularizing chiral fermions. *Physics Letters B*, 105(2):219–223.

Novoselov, K., Geim, A. K., Morozov, S., Jiang, D., Katsnelson, M., Grigorieva, I., Dubonos, S., and Firsov, A. (2005). Two-dimensional gas of massless Dirac fermions in graphene. *Nature*, 438(7065):197–200.

Ohtomo, A. and Hwang, H. (2004). A high-mobility electron gas at the LaAlO3/SrTiO3 heterointerface. *Nature*, 427(6973):423–426.

Qi, X.-L., Hughes, T. L., and Zhang, S.-C. (2008). Topological field theory of time-reversal invariant insulators. *Physical Review B*, 78(19):195424.

Qi, X.-L., Wu, Y.-S., and Zhang, S.-C. (2006). Topological quantization of the spin Hall effect in two-dimensional paramagnetic semiconductors. *Physical Review B*, 74(8):085308.

Qi, X.-L. and Zhang, S.-C. (2010). The quantum spin Hall effect and topological insulators. *Physics Today*, 63(1):33–38.

Qi, X.-L. and Zhang, S.-C. (2011). Topological insulators and superconductors. *Reviews of Modern Physics*, 83(4):1057.

Roy, R. (2009). Topological phases and the quantum spin Hall effect in three dimensions. *Physical Review B*, 79(19):195322.

Sauerbrey, G. (1959). Use of quartz vibration for weighing thin films on a microbalance. *J. Physik*, 155:206–212.

Shockley, W. (1939). On the surface states associated with a periodic potential. *Physical Review*, 56(4):317.

Simmler, W. (2000). Silicon compounds, inorganic. *Ullmann's Encyclopedia of Industrial Chemistry*.

Stern, A. and Lindner, N. H. (2013). Topological quantum computationfrom basic concepts to first experiments. *Science*, 339(6124):1179–1184.

Stone, M. (1992). *Quantum Hall Effect*. World Scientific.

Tamm, I. (1932). On the possible bound states of electrons on a crystal surface. *Phys. Z. Sowjetunion*, 1:733–735.

Tanikawa, T., Matsuda, I., Nagao, T., and Hasegawa, S. (2001). Growth mode and electrical conductance of Ag atomic layers on Si(001) surface. *Surface science*, 493(1):389–398.

Thouless, D., Kohmoto, M., Nightingale, M., and Den Nijs, M. (1982). Quantized Hall conductance in a two-dimensional periodic potential. *Physical Review Letters*, 49(6):405.

van der Pauw, L. (1958). A method of measuring specific resistivity and hall effect of discs of arbitrary shape. *Philips Res. Rep.*, 13:1–9.

Wasa, K. (2012). *Handbook of Sputter Deposition Technology: Fundamentals and Applications for Functional Thin Films, Nano-materials and MEMS*. William Andrew.

Wu, L., Brahlek, M., Aguilar, R. V., Stier, A., Morris, C., Lubashevsky, Y., Bilbro, L., Bansal, N., Oh, S., and Armitage, N. (2013). A sudden collapse in the transport lifetime across the topological phase transition in (Bi1-xInx)2Se3. *Nature Physics*, 9(7):410–414.

Wu, L., Salehi, M., Koirala, N., Moon, J., Oh, S., and Armitage, N. (2016). Quantized Faraday and Kerr rotation and axion electrodynamics of the surface states of three-dimensional topological insulators. *arXiv preprint arXiv:1603.04317*.

Wu, L., Tse, W.-K., Brahlek, M., Morris, C., Aguilar, R. V., Koirala, N., Oh, S., and Armitage, N. (2015). High-Resolution Faraday Rotation and Electron-Phonon Coupling

in Surface States of the Bulk-Insulating Topological Insulator Cu0.02Bi2Se3. *Physical Review Letters*, 115(21):217602.

Xia, Y., Qian, D., Hsieh, D., Wray, L., Pal, A., Lin, H., Bansil, A., Grauer, D., Hor, Y., Cava, R., et al. (2009). Observation of a large-gap topological-insulator class with a single Dirac cone on the surface. *Nature Physics*, 5(6):398–402.

Xu, Y., Miotkowski, I., Liu, C., Tian, J., Nam, H., Alidoust, N., Hu, J., Shih, C.-K., Hasan, M. Z., and Chen, Y. P. (2014). Observation of topological surface state quantum Hall effect in an intrinsic three-dimensional topological insulator. *Nature Physics*, 10(12):956–963.

Yan, B., Jansen, M., and Felser, C. (2013). A large-energy-gap oxide topological insulator based on the superconductor BaBiO3. *Nature Physics*, 9(11):709–711.

Yokoyama, T. and Murakami, S. (2014). Spintronics and spincaloritronics in topological insulators. *Physica E: Low-dimensional Systems and Nanostructures*, 55:1–8.

Yoshimi, R., Tsukazaki, A., Kozuka, Y., Falson, J., Takahashi, K., Checkelsky, J., Nagaosa, N., Kawasaki, M., and Tokura, Y. (2015). Quantum Hall effect on top and bottom surface states of topological insulator (Bi1-xSbx)2Te3 films. *Nature Communications*, 6.

Zangwill, A. (1988). *Physics at surfaces*. Cambridge university press.

Zhang, H., Liu, C.-X., Qi, X.-L., Dai, X., Fang, Z., and Zhang, S.-C. (2009). Topological insulators in Bi2Se3, Bi2Te3 and Sb2Te3 with a single Dirac cone on the surface. *Nature Physics*, 5(6):438–442.

Zhang, Y., He, K., Chang, C.-Z., Song, C.-L., Wang, L.-L., Chen, X., Jia, J.-F., Fang, Z., Dai, X., Shan, W.-Y., et al. (2010). Crossover of the three-dimensional topological insulator Bi2Se3 to the two-dimensional limit. *Nature Physics*, 6(8):584–588.